UNIVERSITÀ DEGLI STUDI DI PALERMO
Dottorato di Ricerca in Fisica
Dipartimento di Fisica e Chimica
Settore Scientifico Disciplinare FIS03

ATOMIC EMISSION AND PHOTON LOCALIZATION IN 1D MICROCAVITY ARRAY

IL DOTTORE
Federico Lombardo

IL COORDINATORE
Prof. Antonio Cupane

IL TUTOR
Prof. Gioacchino Massimo Palma

CICLO XXVI
ANNO CONSEGUIMENTO TITOLO 2016

Contents

Introduction

Research in cavity quantum electrodynamics (CQED) explores quantum dynamical processes for individual atoms strongly coupled to the quantized electromagnetic field of a resonator. For more applications in CQED, current interest lies in the coherent interaction among several cavities coupled each other.
Coupled-cavity arrays (CCAs) typically consist of an arrangement of low-loss single-mode cavities with nearest-neighbor coupling allowing photon hopping between neighboring cavities. In turn, each cavity may interact with one or more atoms (or atomlike systems). Progress in the fabrication techniques make such systems experimentally accessible in the immediate future [1, 9, 10, 140]. Such arrays have been proposed, for example, to control the coherent transport of a single photon by means of an artificial two-level atom which works as a quantum switch [17]. Other studies have focused on their potential to work as an effective platform to carry out quantum information processing tasks [5, 11, 12, 13]. Moreover, recent works have also shown that, when such an array of coupled cavities is doped with two- or multi-level atoms, the photon-blockade effect can emerge and it can be achieved a Mott-insulator state of polaritons that are many-body dressed states of atoms coupled to quantized modes of the optical field in the array [1, 3, 4].
This research in progress motivates us to further investigate some aspects of the interesting and extremely rich physics of a CCA interacting with a single two-level atom-like system.

The first part of this thesis is focused on the localization properties of a single excitation inside such an uniform CCA, which we theoretically examine by means of both analytic and numerical methods. In particular, in Sec 3.2 we discuss the emission of a two-level atom embedded in a cavity of the array which gives rise to *photon localization*, i.e. a fraction of the field is shared between the field-modes of the cavities around the atomic position at long times. If the atom is located at the central site of a very extended array, the boundary effects can be neglected. Owing to the presence of polaritonic atom-photon *bound states* [32], the atom is in general unable to eventually release the entire amount of its initial excitation to the field and thus exhibits fractional decay [27, 28, 30]. Such *population trapping* manifests itself as a residual oscillatory behavior of the excited state population at long times. Since the bound states show a spatially extended profile, photon localization takes place so that a fraction of the

initial excitation remains localized inside the cavities near the atom. The remaining part of the field propagates away from the atom and its dynamics is regulated by the *unbound* or *scattering states* of the system. The atom-field coupling strength g, or Vacuum Rabi frequency, is a key parameter which determines the particular dynamics of the excitation released. Specifically, it is the ratio between this coupling constant and the photon-hopping rate J, characterizing the coupling between the nearest-neighbour cavities, to determine the long-times balance between the localized fraction of the initial atomic excitation and the trapped one. In the strong-hopping regime, i.e. when g/J is small enough, the atom completely decays with exponential law (in the limit $g/J \to 0$) showing a Markovian behaviour and its excitation is transferred to the propagating field. In this case the CCA behaves as an almost flat spectral-density bath for the atom. In the regime characterized by a very large value of the coupling strength ($g/J \gg 1$), instead, the field remains confined within the cavity coupled to the atom and the resulting dynamics is reduced to the well-known Jaynes-Cummings model with a full atom-field energy swapping with standard vacuum Rabi oscillations at frequency $2g$. One might expect that photon localization and population trapping arise simultaneously as the ratio g/J grows from zero. We found that this is not the case. For atom-cavity resonant coupling, we highlight the existence of a regime of intermediate coupling strengths such that significant field localization can occur with no appreciable population trapping. Specifically, when g/J is conveniently chosen within a given interval, at long times, only a negligible fraction of the localized field-energy is periodically returned to the atom. In this case the localized field periodically undergoes a mere spatial redistribution in the vicinity of the atom. Such behavior arises from the peculiar properties of the two bound stionary states of the joint atom-field system. When the atom is detund from the cavity-mode, the localization profile and the population trapping change quantitatively but not qualitatively, the balance being strongly altered only for very large detuning. The main effect of the atom-cavity detuning is to produce an imbalance between the two bound states. The atomic trapped energy is always an increasing function of the detuning, while the localized energy shows a different behaviour depending on g/J. However, we show that their ratio, for a given value of g/J, is a monotonic increasing function of the detuning. As result, the effect of photon localization without population trapping, maximum at resonance, is still present for moderate atom-cavity detuning but the range of g/J within which such effect occurs is shrinked.
The localization and trapping properties discussed above arise from the presence of a pair of polaritonic bound states for the atom-CCA system and the spectrum of the bare uniform CCA, described by means of a tight-binding model, consists only of unbound states. If one or more defects are introduced into the bare CCA, i.e. cavities with different frequencies or hopping rates, the system will show a bound (photonic) state for each defect. Static disorder in such an 1D array, i.e. cavity-modes with random frequencies or random hopping rates, gives rise to a spectrum consisting only of localized eigenstates. This is a general multiple-scattering wave phenomenon (also valid for 2D and, under certain conditions, 3D systems), known as *Anderson localization* after Phillip Anderson who first predicted it in 1958 [60]. It has been observed in condensed matter [71], classical light [72, 73, 75, 76], acoustic waves [77] and Bose-Einstein condensates [78].

In the second part of the thesis we deal with the emission of a two-level atom coupled to such disordered array. Only uncorrelated disorder consisting of coupled cavities with random frequencies and uniform hopping is considered. In Sec 4.1.2 we implement the model by numerical diagonalization of the atom-CCA Hamiltonian with gaussian disorder for several realizations of the latter, characterized by different values of the associated standard deviation. The atom, coupled to the central cavity of the array in the strong-hopping regime ($g/J = 0.1$), can (almost) completely release its excitation only for small disorder. We choose to study the system only in this regime, in which the atom-photon bound states play no role, in order to investigate how the atomic Markovian dynamics is altered by the presence of static disordr. By means of an *open quantum systems* approach, we consider the atomic system interacting with a particular environment consisting of a restricted set of localized mods, depending on the disorder strength. When the latter one is large enough, each eigenstate of the bare CCA is localized on a single site. In this case the eigenstate localized on the central site dominates the atom-field dynamics, the other ones showing a negligible overlap with the atomic site. This results in a detuned (nearly closed) Jaynnes-Cummings dynamics between this central eigenmode and the atom. In general, when the disorder is not too strong, several eigenmodes will overlap on the central site. By means of numerical simulations, in Sec 4.2.4 we show that the bare-array environment behaves as a single open QED cavity from the atom perspective. The atom-cavity effective coupling constant, as well as the atomic external decay rate, will depend on the disorder strength. This equivalent dynamics describes the averaged evolution over several disorder realizations.

The two parts of the work on which I focused during the three years of my Ph.D. are presented, respectively, in the third and fourth chapter of this thesis. In Chapter 1 QED Cavities are introduced and some of the physics of these system is explained. Some of their possible experimental realizations are also discussed. Chapter 2 is devoted to the introduction of the mathematical tools needed to analyze the physics of Coupled QED Cavity arrays. Here the Green's function method is adopted to obtain the spectral properties of systems consisting of a two-level atom interacting with a generic bath of modes. Special attention is paid to the tigth-binding Hamiltonians, which we adopt as mathemathical models to analyze the physical systems of our interest.

Chapter 1

Cavity QED: Theory and pratical implementation

The most elementary form of interaction between light and matter, a single atom interacting with a single photon, has been the subject of theoretical and experimental research. Traditionally, one of the main difficulties in atomic physics is the very low probability of detecting photons and the weak light-matter interaction. In these conditions, experiments demanded that many photons scatter off a large number of atoms, making it impossible to shed light on the single quanta interactions. The direct observation of the fundamental quantum interaction has been for a long time elusive. Since the late '70 many experimental groups have carried out a lot of *thought experiments*, or some of their variants, on which the fathers of quantum physics have much debated [81, 91, 93, 94, 95, 96, 97, 100, 101, 102, 103, 104, 105, 109]. Manipulate individual objects with such a level of precision required the aid of particular resonators designed to make sufficiently strong and lasting these single-quanta interactions. Reaching this regime has been a major focus of research in atomic physics and quantum optics for several decades and has generated the field of cavity quantum electrodynamics (CQED).
In recent years the number of scientific publications, theoretical and experimental, on the interaction of a single mode of the quantized e.m. field within a cavity QED resonator with a single two level atom or atom-like system (TLS) has grown considerably, the argument being an essential chapter of all the latest quantum optics textbooks [81, 82, 83, 84, 85, 86, 87, 88].
This chapter examines the theoretical aspects and possible practical implementations of single-mode resonators that interact, in different regimes, with atom-like two-level systems. Moreover, given the current level of technology, we will see what are the best experimental candidates for implementing CQED applications.

1.1 Theory on Cavity QED

Traditional Cavity Quantum Electrodynamics is concerned with the very different situation of an atom trapped in a cavity of a size comparable to the wavelength of the emitted radiation. A major part of all Cavity QED experiments has been performed with Fabry-Perot cavities formed by rather massive mirrors. As we will see later, more recent settings make use of several new structures with small-volume micro-cavities.
Although most of the early experiments were made to investigate the changes in the rate of emission of an atom interacting with a confined environment, different from the free-vacuum, consisting of a cavity (for example to test the Purcell effect, in the so called *weak-coupling regime*), more recently the focus on Cavity QED has shifted to the possibility to make the atom-photon interaction as more intense and lasting as possible: the *strong coupling regime*.

1.1.1 CQED in the strong coupling regime: The Jaynes-Cummings model

Let us consider a series of features common to all realizations of such single-mode cavities interacting with a two-level system. Since, in the strong coupling regime, the aim of CQED is to enhance the interaction between atoms and photons, any experimental realization must ensure that a single photon can be sufficient to saturate the atomic transition. This condition is achieved by confining the photon to a small volume that can be several orders of magnitude smaller than in free space (in a Fabry-Perot setup this volume is defined by the mirrors and the optical modes they support). A small volume increases the atom-light coupling strenght known, for a single photon, as Vacuum Rabi frequency. It is also important to ensure that the duration of the interaction is sufficiently long, reducing losses from the cavity and the unwanted emission of the atom into the external continuum of modes. These essential physical features are described by the *Jaynes-Cummings model* [59], wich represents the theoretical framework for Cavity QED. The authors, in their work dating back to 1963, established the full quantum electrodynamic theory of a single emitter (e.g. an ammonia molecule in a maser) interacting with a single mode of the electromagnetic field. For a two-level atom with ground state $|g\rangle$, excited level $|e\rangle$ and transition energy $\hbar\omega_a = \hbar(\omega_e - \omega_g)$, coupled to a generic reservoir of modes, as in the case of the vacuum or other particular environments, the total atom-field Hamiltonian in the Schrödinger picture reads:

$$\hat{H} = \hat{H}^r + \hat{H}^a + \hat{H}^{coup} = \sum_k \hbar\omega_k \hat{a}_k^\dagger \hat{a}_k + \frac{\hbar}{2}\omega_a \hat{\sigma}_z + \hbar \sum_k g_k \left(\hat{a}_k^\dagger \hat{\sigma}_- + \hat{a}_k \hat{\sigma}_+\right) \tag{1.1}$$

where the g_k coupling constants are generally expressed in dipole approximation and the dispersion relation for the allowed frequencies depends on the specific environment ($\omega_k = ck$ for the vacuum). The k-mode creation and annihilation operators, respectively $\hat{a}_k^\dagger$ and $\hat{a}_k$, satisfy

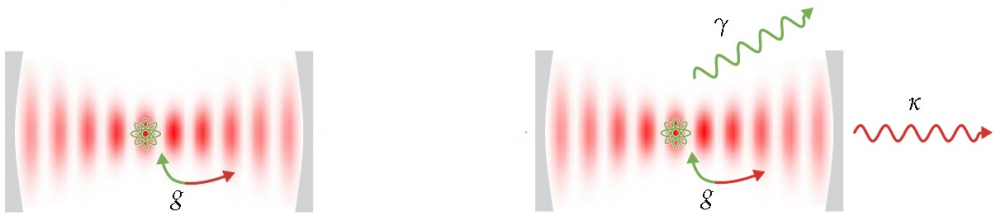

(a) (b)

Figure 1.1: An atom inside a single mode cavity. The atom-field coupling is given by the Vacuum Rabi frequency g. (a) Ideally lossless cavity. (b) System with leakages: the atom is also coupled to the continuum external modes at rate γ and the cavity loses photons at rate k.

the bosonic commutation relations $\left[\hat{a}_k, \hat{a}^\dagger_{k'}\right] = \delta_{k,k'}$ and the atomic Hamiltonian $\hat{H}^a = \frac{\hbar}{2}\omega_a\hat{\sigma}_z$ is chosen selecting the level $\hbar(\omega_e + \omega_g)/2$ as zero for the energies. Moreover, the coupling Hamiltonian $\hat{H}^{coup}$ in (1.1) is expressed in the *rotating wave approximation* (RWA), i.e. they have been neglected the *counter-rotating* terms $\hat{a}^\dagger_k\hat{\sigma}_+$ and $\hat{a}_k\hat{\sigma}_-$, these having a negligible effect on the evolution. The RWA is valid if the field strenght is not too large and assuming also that the state of the field does not vary rapidly on a time scale of ω_a^{-1}. An important property of the Hamiltonian (1.1) is that it conserves the total number of excitations, indeed the total number operator $\hat{N} = \hat{\sigma}_+\hat{\sigma}_- + \sum_k \hat{a}^\dagger_k\hat{a}_k$ commutates with $\hat{H}$.
In Fig (1.1(a)) is depicted a single two-level atom in a fixed position inside a single-mode cavity, whose resonant frequency is ω_c. Now the TLS is no longer coupled to a continuum of modes, as in the case of free space, but to a single quantum oscillator representing the only field mode the cavity ideally supports. As we shall see later, this is the ideal situation of a lossless cavity with an infinity Quality factor, since in practice any cavity presents losses and therefore the distribution of the allowed modes has a finite width. This more realistic situation is depicted in Fig (1.1(b)) in which the photon loss from the cavity mode (for example due to the leakage through the cavity mirrors) occurs at a rate k and, in addition, the atom can lose its excitation via spontaneous emission outside of the cavity mode, at a rate γ. The situation in wich the atom can exchange its excitation with the field inside the cavity for a sufficiently long time before decaying into the external modes and before the cavity loses its field is the above mentioned *strong coupling* regime. If we indicate with g the coupling between the atom and the cavity mode, it is intuitive to deduce that this regime is reached when $g \gg k, \gamma$. The theoretical background for the ideal case of Fig (1.1(a)) is the originally conceived Jaynes-Cummings model with $k = \gamma = 0$, i.e. the cavity QED strong coupling regime with infinite Quality factor. Now here we treat this ideal case, postponing the discussion on the losses to the next section.
From (1.1) we immediately obtain the Hamiltonian for a TLS with transition energy $\hbar\omega_a$ coupled to a field mode of frequency ω_c in dipole and rotating wave approximation:

$$\hat{H}^{JC} = \hat{H}^c + \hat{H}^a + \hat{H}^{ac} = \hbar\omega_c\left(\hat{a}^\dagger\hat{a} + \frac{1}{2}\right) + \frac{\hbar}{2}\omega_a\hat{\sigma}_z + \hbar g\left(\hat{a}\hat{\sigma}^+ + \hat{a}^\dagger\hat{\sigma}^-\right) \tag{1.2}$$

Here the coupling constant g, assumed real without loss of generality, is known as Vacuum Rabi frequency and the validity of the RWA is maintained for $g \ll \{\omega_a, \omega_c\}$. However it should be remembered that in this case the electric and magnetic field inside the cavity, as well as the vector potential, are stationary waves and their amplitudes are not constant and exhibit nodes and antinodes within the cavity volume. It can be shown that the electric field and the Vacuum Rabi frequency are described by the cavity mode function $f(\mathbf{r})$ [83] as :

$$\hat{E}(\mathbf{r}) = \sqrt{\frac{\hbar\omega_c}{2\epsilon_0 V}}\left(f(\mathbf{r})\hat{a} + f^*(\mathbf{r})\hat{a}^\dagger\right)\epsilon \qquad \textit{and} \qquad g(\mathbf{r}) = \mathbf{d}_a \cdot \epsilon\sqrt{\frac{\omega_c}{2\hbar\epsilon_0 V}}|f(\mathbf{r})| \tag{1.3}$$

where $V = \int |f(\mathbf{r})|d^3\mathbf{r}$ is the mode volume, ϵ the electric field polarization versor and $\mathbf{d}_a = \langle g|\mathbf{R}|e\rangle$ the atomic dipole matrix element. If the atom is located at an antinode of the electric field and, for a suitable choice of the electric polarization, we have $\epsilon \cdot \mathbf{d}_a = |\mathbf{d}_a| = d_a$, The Vacuum Rabi frequency is the maximum possible and reads [81]:

$$g = \sqrt{\frac{d_a^2\omega_c}{2\hbar\epsilon_0 V}} \tag{1.4}$$

In absence of the coupling term $\hat{H}^{ac}$, the Hamiltonian $\hat{H}^0 = \hat{H}^c + \hat{H}^a$ in (1.2) admits tensor-product eigenstates of the form $|e, n\rangle$ or $|g, n\rangle$, wich means that the field is in the generic Fock state $|n\rangle$ and the atom can be either in $|e\rangle$ or in $|g\rangle$. Its eigenvalues form an infinite ladder of two-level manifolds separated by the cavity frequency ω_c. Indicating with $\delta = \omega_a - \omega_c$ the atom-cavity detuning, each manifold consists of the two levels $|e, n\rangle$ and $|g, n+1\rangle$, both carrying $n + 1$ total excitations, separated by the energy $\hbar\delta$ (the state with the higer energy being $|e, n\rangle$ or $|g, n + 1\rangle$, respectively for $\delta > 0$ or $\delta < 0$). In this scheme the atom-field ground state $|g, 0\rangle$ is apart at the bottom of the ladder. Hence, the uncoupled Hamiltonian $\hat{H}^0$ is diagonal in the basis $\{|g, 0\rangle, |g, 1\rangle, |e, 0\rangle, |g, 2\rangle, |e, 1\rangle, \ldots |g, n + 1\rangle, |e, n\rangle, \ldots\}$. The diagonalization of the complete Jaynes-Cummings Hamiltonian in (1.2) leads to the following block-diagonal form :

$$\hat{H}^{JC} = \begin{bmatrix} \frac{1}{2}\hbar\omega_c & 0 & 0 & \ldots & \ldots & \\ 0 & \hat{h}_1 & 0 & \ldots & \ldots & \\ 0 & 0 & \hat{h}_2 & 0 & \ldots & \\ 0 & 0 & 0 & \ddots & \ldots & \\ \vdots & \vdots & \vdots & \vdots & \hat{h}_n & \\ 0 & \ldots & \ldots & \ldots & \ldots & \ddots \end{bmatrix}$$

in which the n-th 2×2 block $\hat{h}_n$ mixes the states $|g, n+1\rangle$ and $|e, n\rangle$ belonging to the n-th uncoupled manifold of $\hat{H}_0$ and, in this two-state basis, it is given by the matrix:

$$\hat{h}_n = \hbar \begin{bmatrix} \omega_c \left(n + \frac{1}{2}\right) + \frac{\delta}{2} & g\sqrt{n+1} \\ g\sqrt{n+1} & \omega_c \left(n + \frac{1}{2}\right) - \frac{\delta}{2} \end{bmatrix} \tag{1.5}$$

with eigenvalues and eigenvectors given by:

$$E_n^{\pm} = \hbar\omega_c \left(n + \frac{1}{2}\right) \pm \hbar \sqrt{\frac{\delta^2}{4} + g^2(n+1)} \tag{1.6}$$

$$|+, n\rangle = \sin\theta_n |e, n\rangle + \cos\theta_n |g, n+1\rangle \tag{1.7a}$$

$$|-, n\rangle = \cos\theta_n |e, n\rangle - \sin\theta_n |g, n+1\rangle \tag{1.7b}$$

with

$$\tan 2\theta_n = -\frac{2g\sqrt{n+1}}{\delta} = -\frac{2g_n}{\delta} \tag{1.8}$$

These states, which are generally entangled, are called the *dressed states* of the atom-field system and the mixing angle θ_n defined in (1.8) indicates, for each of them, the relative weight of the two uncoupled eigenstates $|g, n+1\rangle$ and $|e, n\rangle$. In (1.8) we have introduced the 'n-photons' Rabi frequency at resonance $g_n = g\sqrt{n+1}$. For very large detuning, but always within the range of validity of the RWA, i.e. $g \ll |\delta| \ll \omega_c$, the dressed states in (1.7) tend to the uncoupled ones: for positive detunings we have $|+, n\rangle \approx |e, n\rangle$ and $|-, n\rangle \approx -|g, n+1\rangle$, while for negative values they approximate as $|+, n\rangle \approx |g, n+1\rangle$ and $|-, n\rangle \approx |e, n\rangle$. In Fig (1.2b) is shown the behaviour of the two eigenenergies $E_n^{\pm}$, given in (1.6), as a function of the detuning for the generic n-th dressed level. The correspondig energies for the uncoupled levels are also shown as dotted lines and they cross at resonance. When the atom-field coupling is turned on, with a Rabi frequency g, the degeneracy at $\delta = 0$ of the two uncoupled levels $|g, n+1\rangle$ and $|e, n\rangle$ is lifted and the corresponding dressed states are separated by the minimum energy $2\hbar g_n$. The energies for the resonant case with and without coupling are shown in Fig (1.2a). If a nonvanishing detuning is introduced this energy separation increases and, for very large values, as it happens for the dressed states, the eigenenergies $E_n^{\pm}$ tend to the uncoupled ones $\hbar\omega_c \left(n + \frac{1}{2}\right) \pm \frac{\hbar\delta}{2}$.
The atom-field state evolution at the generic time t can be found by solving the time dependent Schrödinger equation for the Hamiltonian in (1.2). In general it may involve several blocks, but each 'n+1 excitations' component of the initial state evolves only with the corresponding Hamiltonian block $\hat{h}_n$ given in (1.5). In the interaction representation with respect to $\hat{H}^c = \hbar\omega_c \left(\hat{a}^\dagger \hat{a} + \frac{1}{2}\right)$, given in (1.2), the state at time t reads:

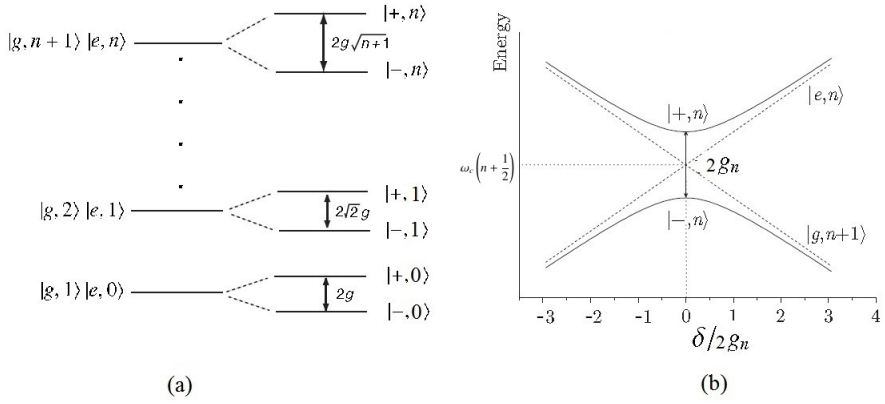

Figure 1.2: (a) Dressed states for the Jaynes-Cummings model in the resonant case. On the left, for each manifold, are shown the uncoupled degenerate states. On the right, when the atom and the field are coupled with a Vacuum Rabi frequency g, the dressed-states separation energy is shown. (b) Dressed state energies for the generic n-th manifold as a function of the atom-cavity detuning δ. At resonance the energy level separation is the minimum, equal to $2g_n = 2g\sqrt{n+1}$. The uncoupled state energies are represented as dotted lines and they cross at $\delta = 0$. For $\delta \gg g_n$ the uncoupled levels and the dressed energies converge. All energies are in $\hbar = 1$ units.

$$|\Psi(t)\rangle = \sum_n \left[C_{e,n}(t)|e,n\rangle + C_{g,n+1}(t)|g,n+1\rangle\right] e^{-i\left(n+\frac{1}{2}\right)\omega_c t} \tag{1.9}$$

By projecting the Schrödinger equation onto the $|e,n\rangle$ and $|g,n+1\rangle$ states, we find the equations of motion for the atom-field probability amplitudes in the n-th manifold:

$$\begin{aligned} \dot{C}_{e,n} &= -\frac{1}{2}i\delta C_{e,n} - ig\sqrt{n+1}C_{g,n+1} \\ \dot{C}_{g,n+1} &= \frac{1}{2}i\delta C_{g,n+1} - ig\sqrt{n+1}C_{e,n} \end{aligned} \tag{1.10}$$

For our purposes is sufficient to consider the solutions for $|\Psi(0)\rangle = |e,n\rangle$, i.e. at $t = 0$ we consider the atom in $|e\rangle$ and n photons in the cavity. Setting $C_{e,n}(0) = 1$ and $C_{g,n+1}(0) = 0$ in (1.10), we find the following time evolution for the probabilities:

$$\begin{aligned} P_{e,n}(t) &= |C_{e,n}(t)|^2 = \frac{\delta^2}{4g_n'^2} + \left(1 - \frac{\delta^2}{4g_n'^2}\right)\cos^2(g_n' t) \\ P_{g,n+1}(t) &= |C_{g,n+1}(t)|^2 = \frac{g_n^2}{g_n'^2}\sin^2(g_n' t) \end{aligned} \tag{1.11}$$

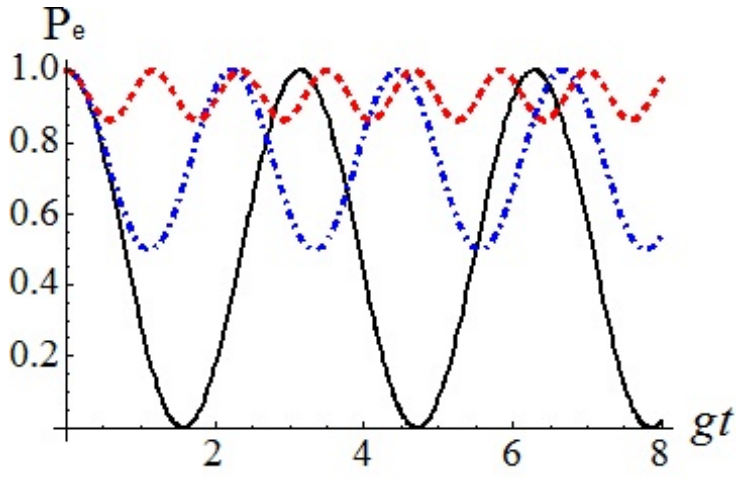

Figure 1.3: Atomic excitation probability $P_{e,0}$ for the $|e,0\rangle$ initial state as a function of the time, with generic Vacuum Rabi constant g. The three curves are relative to different values of the atom-field detuning: $\delta = 0$ (Black solid), $\delta/g = 2$ (Blue dot-dashed), $\delta/g = 5$ (Red dashed).

in which we have introduced the 'effective n-photons' Rabi frequency $g'_n = \sqrt{\delta^2/4 + g^2(n+1)}$. The above equations describe the two probabilities $P_{e,n}$ and $P_{g,n+1}$ oscillating at frequency $2g'_n$ around the average values given by:

$$< P_{e,n} >= \frac{1}{2}\left(1 + \frac{\delta^2}{\delta^2 + 4g^2(n+1)}\right) \qquad (1.12)$$
$$< P_{g,n+1} >= \frac{g_n^2}{\delta^2/2 + 2g^2(n+1)}$$

For $\delta = 0$ the two average probabilities are $1/2$ and the atom-field coupling results in a perfectly reversible energy exchange between the states $|e,n\rangle$ and $|g,n+1\rangle$ at frequency $2g_n$, indeed, from (1.11), the two probabilities evolve as $P_{e,n} = \cos^2(g_n t)$ and $P_{g,n+1} = \sin^2(g_n t)$. The case with the atom excited and zero photons at $t = 0$ is sketched in Fig (1.3), in which the black solid line represent the evolution of $P_{e,0}$ at resonance, and it can be viewed as reversible and oscillatory spontaneous emission which occurs at frequency $2g$. As well-known, an atom into the vacuum undergoes an irreversible sponaneous loss of its initial excitation since it is coupled to a continuum of nearly resonant modes. Here the initial atomic excitation is periodically transferred into a photon that remains inside the ideal lossless cavity and can be absorbed exciting again the atom and so on. The situation of an atom at resonance in a single-mode ideal cavity is very different from its spontaneous emission in free space: a coherent atom-field energy exchange in the first case, an irreversible damping in the second one. The red and blue lines in Fig (1.3) show the evolution of $P_{e,0}$ for the same initial state but with two different values

of the atom-cavity detuning. For increasing δ the time-averaged probabilities in (1.12) deviate from their $1/2$-value at resonance and for $\delta/g_n \gg 1$, in general, $P_{e,n}(t)$ and $P_{g,n+1}(t)$ oscillate respectively around a value very close to unity or to zero and with a very little amplitude. This is exactly what is to be expected, indeed an atom excited inside and far-off resonance with a perfect lossless resonator that 'protects' it from the external continuum of modes cannot decay and never loses or exchanges its excitation. In this way many experiments have been done in order to verify the enhancement or suppression of the spontaneous emission of atoms inside QED cavities in different regimes [81].
Another interesting feature of the Jaynes-Cummings model is its anharmonicity, since $g_n \propto \sqrt{n}$. In the strong coupling regime this gives rise to the so-called *photon blockade* effect, thanks to which it is possible to observe non-classical states of light. The effect of the atom-light interaction is to create an anharmonic energy ladder dependent upon the photon occupation, as illustrated in Fig (1.2a). If we consider the atom-cavity system at resonance and pumped by an external probe laser at frequency ω_c, the interaction causes the cavity to be shifted off resonance with the laser after the first photon is absorbed, preventing another photon from entering the cavity until the first photon leaves. This system allows a coherent state to be filtered into a train of single photons resulting in an *anti-bunched* output and it has been observed experimentally for different CQED setups [106].

1.1.2 Intermediate and weak coupling regime: damped CQED

As already briefly mentioned, in addition to the coherent atom-field interaction, the CQED dynamics is affected by two main loss processes: spontaneous emission from level $|e\rangle$ to level $|g\rangle$ at rate γ and cavity photon losses at rate k. Such two rates are independent each other. The Quality factor of a cavity is connected to the rate k by $Q = \omega_c/k$. The spontaneous emission rate is different from the free space decay rate, indeed the atom interacts only with a subset of the free-space modes determined by the solid angle over which the atom 'sees' that background. We refer to a system with $\gamma \neq 0$ as *open cavity*. Although other processes, such as thermal motion of the atom or dephasing due to background electromagnetic fields, also contribute to the losses of the system, their effects are usually much smaller and can be disregarded in many applications. In introducing the Jaynes-Cummings model, we have considered the ideal case of strong coupling regime and neglected any kind of loss. This obviously requires an infinite Q-factor and the $\gamma = 0$ condition must be separately specified. To indicate with a single parameter the condition for which the strong coupling regime is reached, we define the *cooperativity factor* as follows:

$$\xi = \frac{g^2}{2k\gamma} \tag{1.13}$$

When $\xi \gg 1$ the system works in strong coupling and the coherent part of the atom-field evolution dominates over the decoherence processes.
Let us consider the atom-cavity system in the $|e,0\rangle$ state at $t = 0$. In this case the most general approach to obtain the state-amplitude evolution is the master equation. We consider the system at zero temperature and restrict our analysis to the 'no-jump' regime in which the quantum jumps are unimportant, thus we will consider a wavefunction which incorporates only those states coupled by the Hamiltonian evolution. As the system evolves, the possible transitions are:

(i) Free space emission $|e,0\rangle \rightarrow |g,0\rangle$ at rate γ;

(ii) Coherent evolution $|e,0\rangle \rightarrow |g,1\rangle$ with Vacuum Rabi frequency g;

(iii) Cavity decay $|g,1\rangle \rightarrow |g,0\rangle$ at rate k.

The Linblad master equation [1] for the atom-cavity density operator reads:

$$\frac{\partial\hat{\rho}}{\partial t} = -\frac{i}{\hbar}\left[\hat{H^{eff}},\hat{\rho}\right] + \gamma\hat{\sigma}_{-}\hat{\rho}\hat{\sigma}_{+} + k\hat{a}\hat{\rho}\hat{a}^{\dagger} \tag{1.14}$$

with the effective non-Hermitian Hamiltonian $\hat{H}^{eff}$ given by:

$$\hat{H}^{eff} = \hat{H}^{JC} - i\hbar\frac{\gamma}{2}\hat{\sigma}_{+}\hat{\sigma}_{-} - i\hbar\frac{k}{2}\hat{a}^{\dagger}\hat{a} \tag{1.15}$$

We can obtain the 'no-jump' evolution by solving the Schrödinger equation $i\hbar\partial_t|\Psi(t)\rangle = \hat{H}^{eff}|\Psi(t)\rangle$ for the unnormalized state:

$$|\Psi(t)\rangle = C_{e,0}(t)e^{-i\delta t/2}|e,0\rangle + C_{g,1}(t)e^{i\delta t/2}|g,1\rangle \tag{1.16}$$

In this way the equations of motion for the probability amplitude in (1.10), in presence of losses and restricted to the $\{|e,0\rangle, |g,1\rangle\}$ subspace, are modified as follows:

$$\begin{aligned} \dot{C}_{e,0} &= -\frac{\gamma}{2}C_{e,0} - igC_{g,1} \\ \dot{C}_{g,1} &= \left(i\delta - \frac{k}{2}\right)C_{g,1} - igC_{e,n} \end{aligned} \tag{1.17}$$

[1] Master equation in Linblad form provides the prototype of a Markovian dynamics for an open quantum system. Its derivation requires the validity of several approximations, the most important one being the so-called Markov approximation, i.e. that the environmental correlation time is small compared to the open system's relaxation or decoherence time. In Chap 4 we describe a form of time local master equation, characterized by a time-depentent generator, which takes into account for a much larger class of quantum processes.

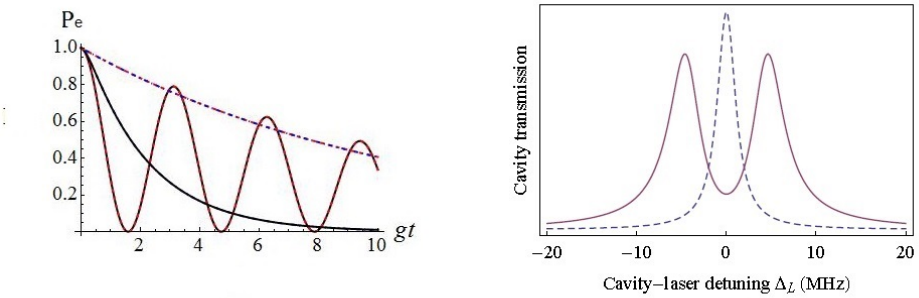

(a) (b)

Figure 1.4: (a) Atomic probability evolution at resonance for three different values of the cavity damping rate k. All the curves are calculated with the same spontaneous emission rate $\gamma = 0.05g$, by analytically solving (1.17). Weak coupling with enhanced emission rate ($k/g = 10$, black solid line); weak coupling and very fast cavity with 'vacuum' decay at rate γ ($k/g = 100$, blue dashed line); Strong coupling with damped oscillations ($k/g = 0.1$, red line). (b) Simulation for the cavity transmission in a laser-driven cavity experiment, showing the normal mode splitting (from [138]). The transmission is plotted as a function of the cavity-laser detuning $\Delta_L = \omega_c - \omega_L$ and the atom is assumed to be resonant with the cavity. The average photon number is $\langle n \rangle = 1$ and the parameters are $g, \gamma, k = 2\pi \times (4.5, 3, 1.25)MHz$. The dashed line represents the empty cavity spectrum.

which admit general solutions for $C_{e,0}(t)$ and arbitrary g, γ, k of the form:

$$C_{e,0}(t) = C_+ e^{\alpha_+ t} + C_- e^{\alpha_- t} \tag{1.18}$$

where the coefficients C_+, C_- can be derived from the initial conditions $|C_{e,0}| = 1$, $C_{g,1} = 0$ and the exponents are:

$$\alpha_\pm = \frac{1}{4}(\gamma + k - 2i\delta) \pm \frac{1}{2}\left[\frac{1}{4}(\gamma + k - 2i\delta)^2 - 4g^2\right]^{1/2} \tag{1.19}$$

1.1.2.1 Intermediate and strong coupling regime

The exponents in (1.19) are in general complex. For $\delta = 0$ it can be seen that they have nonvanishing imaginary parts if $\gamma + k > 4g$ and the evolution of $|C_{e,0}(t)|^2$ will show damped oscillations. We refer to this regime as *intermediate coupling*. As already seen, the strong coupling regime is reached when $\xi \gg 1$ or $g^2 \gg k\gamma$. In this case we can approximate the solutions (1.19) as:

$$\alpha_{\pm} \approx \frac{1}{4}(\gamma + k - 2i\delta) \pm ig \tag{1.20}$$

This leads to a damped oscillation of $|C_{e,0}(t)|^2$ at frequency $2g$ for $\delta = 0$ and with damping constant $(\gamma + k)/4$, as illustrated in Fig (1.4a). Physically this means that the coupling constant between the atom and the cavity mode is so strong that a photon emitted into the cavity is likely to be reabsorbed before leaving out of the cavity.
The damped atom-cavity system gives a finite width to the JC doublet resonances. This can be seen by calculating the eigenvalues of $\hat{H}^{eff}$ in (1.15). In the presence of damping and at resonance, the two JC eigenvalues in (1.6) are modified as follows [99]:

$$E_n^{\pm} = \hbar\omega_c\left(n + \frac{1}{2}\right) - i\frac{\hbar}{4}\left[k(2n-1) + \gamma\right] \pm \frac{\hbar}{4}\sqrt{16ng^2 - (\gamma - k)^2} \tag{1.21}$$

These eigenvalues have a Rabi splitting $E_n^+ - E_n^-$ which differs from the loseless case. The normal mode splitting at resonance is shown in Fig (1.4b) for a simulation of a driven-cavity experiment. This Rabi splitting can only be resolved if the square root in (1.21) is real and if it is larger than the imaginary part, i.e. $g^2 \gg k\gamma$. This justifies the definition of strong coupling regime given above, which can be also seen as the regime in which the spectrum consists of a doublet of well-separated Lorentzian lines of equal widths $(k+\gamma)/4$ and energy splitting almost equal to $2g\sqrt{n}$.
It is possible to test experimentally the Vacuum Rabi splitting, i.e. the normal mode splitting for $n = 0$, by probing the cavity with a laser while monitoring the transmission. For coherent and sufficiently weak pumping, the atom-cavity spectrum for $\delta = 0$ can be obtained as the cavity transmission as a function of the laser-cavity detuning Δ_L. The transmission can be analytically calculated by adding a driving term in the Hamiltonian (1.15), proportional to $i(\hat{a} - \hat{a}^{\dagger})$, and calculating $\langle n \rangle$ in the steady-state regime. The evolution must be restricted to the subspace spanned by $\{|e,0\rangle, |g,1\rangle, |g,0\rangle\}$ and the cavity transmission, plotted in Fig (1.4b), is found to be proportional to $|C_{g,0}(\Delta_L)|^2$.

1.1.2.2 Weak coupling regime

In the weak coupling regime, caracterized by $g \ll k, \gamma$, the dynamics of the emitter is basically incoherent and dominated by the damping rates. Formally integrating (1.17) yields:

$$C_{g,1}(t) = -ig\int_0^t dt' C_{e,0}(t') e^{(i\delta - k/2)(t-t')} \tag{1.22}$$

In many experimental cases of weak coupling regime the system can be either a *closed cavity* with $\gamma = 0$ and $g \ll k$, or an open cavity which works in the so called *fast cavity* regime in which $\gamma < g \ll k$. In both cases the photon leaks out of the cavity (at rate k) immediately after

being emitted so that the population of $|g,1\rangle$ can be neglected [83] and we can assume $\dot{C}_{g,1} \approx 0$ in (1.17) [2], thus:

$$C_{g,1}(t) = \frac{ig}{i\delta - k/2} C_{e,0}(t) \tag{1.23}$$

This corresponds to evaluate $C_{e,0}$ at $t' = t$ and remove it from the integral in (1.22). The strongly damped cavity field affects the evolution of the atomic state which can be obtained by substituting the above value into (1.17):

$$\dot{C}_{e,1}(t) = -\left[\frac{\gamma}{2} + \frac{g^2(k/2 + i\delta)}{\delta^2 + k^2/4}\right] C_{e,0}(t) \tag{1.24}$$

and the evolution of the atomic excitation probability is:

$$P_{e,0}(t) = |C_{e,0}(t)|^2 = e^{-\gamma_c t} \qquad with \qquad \gamma_c = \gamma + \frac{2g^2}{k} \frac{1}{1 + 2(2\delta/k)^2} \tag{1.25}$$

We retrive an exponential decay for the atomic upper state with rate modified by its coupling to the overdamped cavity mode. Moreover, for $\delta \neq 0$, the Lamb-shift term proportional to $i\delta$ in (1.24) describes an energy shift of the atomic transition due to the detuned interaction with the cavity mode. The fundamental result represented by (1.25) is that the QED cavities can be used to enhance or reduce the spontaneous emission rate. At resonance we always obtain an increase in the decay rate, the well-known *Purcell effect*. The enhanced rate in (1.25) can be put into the form:

$$\gamma_c = \gamma\,(1 + 4\xi) \tag{1.26}$$

where ξ is the Cooperativity factor introduced in (1.13) to describe the open atom-cavity system. For a closed cavity ($\gamma = 0$) at resonance, we define the *Purcell factor* to compare γ_c in (1.25) with the vacuum emission rate[3] $\Gamma_0 = \frac{d_a^2 \omega_a^3}{3\pi\epsilon_0 c^3}$, using the Quality factor $Q = \omega_c/k$. This reads:

$$\frac{\gamma_c}{\Gamma_0} = \frac{3Q\lambda^3}{4\pi^2 V} \tag{1.27}$$

with $\lambda = 2\pi c/\omega_c$. In order to obtain a large Purcell factor we should work with high-Q cavity with small mode volume and the spectral width of the emitter should be smaller than the cavity width.

For a closed cavity far-detuned from the atomic resonance, $\delta \gg k$, the atomic decay rate is

[2] This is a good approximation if γ and g are small compared to $|\delta| + |k|/2$

[3] We will calculate this rate by means of the Green's function approach in the next chapter.

strongly suppressed. This effect has been seen in microwave experiments where the cavity size is of the order of the wavelength $L \approx \lambda$. The decay-rate ratio in this regime is:

$$\frac{\gamma_c}{\Gamma_0} = \frac{3\lambda^3}{16\pi^2 QV} \tag{1.28}$$

so the decay rate is suppressed by the cavity quality factor.

1.2 CQED practical implementations

Modern CQED setups result from more than fifty years of incremental improvements in cavity design and atom manipulations, which have largely benefited from the technological development of lasers, quantum optics and solid state devices. The first discussion of a CQED concept is found in the short note by Purcell [92], in which he predicted that the spontaneous emission rate of a spin in a magnetic resonance setup, exceedingly low in free space, should be considerably enhanced in a resonant structure, such as a resonant R-L-C circuit used to filter the free-induction decay NMR signals. This argument was applied to a spin in an NMR context, but the same effect is expected for an atom in an optical cavity and it applies only as long as the damped cavity mode can be considered as a continuum. This is the case of CQED in the weak-coupling regime in which, as described above, spontaneous emission can be enhanced by imposing boundary conditions to the field radiated by the atom, indeed the Q-factor reaches high values in small-volume, high-quality cavities.
The first CQED experiments, strictly speaking, date back to the early-mid 1980s, thanks to progress in laser and microwave technology. These experiments were carried out with Rydberg atoms in the microwave regime, chiefly because it is much easier to achieve a small mode volume, comparable to the wavelength, when the latter is measured in centimetres rather than micrometres. In early microwave experiments atoms were detected and used to reveal the evolution of the field in the cavity. Thus Haroche [93] was the first to observe Purcell enhancement in 1983, using a beam of low-lying Na Rydberg atoms ($23S \rightarrow 22P$ transition at 340 GHz) and a niobium superconducting cavity. The atoms were prepared in the $23S$ state prior to entering the cavity; if the latter is off-resonant, only $23S$ atoms were detected after the transit. When the cavity was tuned in resonance, $22P$ atoms were detected, showing that the radiative decay $23S \rightarrow 22P$ has been enhanced by the cavity. Shortly after, several other experiments using beams of atoms in microwave CQED setups were conducted by other researchers to demonstrate both enhancement and inhibition of spontaneous emission [95]. In 1987 G. Rempe, H. Walther, and N. Klein demonstrated experimentally for the first time the quantum collapse and revival predicted by the Jaynes-Cummings model by using a one-atom maser with Rb Rydberg atoms [97]. At that time optical CQED started to progress in parallel with microwave experiments and, here too, the challenge was the realization of a small-volume high-Q cavity. The breakthrough came with the development of extremely high-finesse multi-dielectric mirrors,

mounted in a Fabry-Perot configuration with typical cavity length of $\approx 100\mu m$ and mirror diameter in the millimetre range [81]. The photon storage time reached the microsecond range. In these experiments it is the field leaking from the cavity which provides information about the atomic behaviour. Suppression of spontaneous emission in the near-infrared was demonstrated by Haroche in 1987 [100] on the caesium $5D_{5/2} \rightarrow 6P_{3/2}$ line at $3.49\mu m$ in a planar geometry. The first manifestation of the strong coupling regime dates back to 1992 when Thompson, Kimble et al. [101] observed the 'vacuum Rabi splitting' using the caesium $D2$ line at 852 nm and an high-finesse optical resonator. Experiments with atoms trapped and cooled inside small optical cavities by way of a far-off resonance dipole-force trap (FORT) were carried out for the first time in the early 2000's. In [105] trapped caesium atoms were observed continuously via transmission of a strongly coupled probe beam, with individual events lasting $\approx 1s$. At the same time, improvements in trapping techniques made it possible to load atoms deterministically into the cavity, for example with a standing-wave conveyor belt [109]. The latest development of CQED experiments is that of coherent control. Strong coupling can be used to manipulate entanglement, and this has given rise to a number of applications in quantum information. In a recent experiment Rempe employed a scheme that entangles a stationary atom inside a high-finesse optical cavity with a flying photon. This then carries the entanglement to a remote location where the photonic state can be mapped onto another atomic system, thus entangling the atomic emitter with the atomic receiver [98]. The Haroche's group carried out other experiments in the same direction. For example they have implemented a nondestructive counting of photons, the recording of field quantum jumps, the preparation and reconstruction of 'Schrödinger cat' states of radiation and the study of their decoherence, which provides a striking illustration of the transition from the quantum to the classical world [91]. These experiments have also led to the demonstration of basic steps in quantum information processing, including the deterministic entanglement of atoms and the realization of quantum gates using atoms and photons as quantum bits.

Here we present a brief, non-exhaustive, review of what are the best experimental CQED candidates to implement, given the current level of technology, atom-field coupling applications, focusing in particular on systems with 'fixed' atom-like TLS able to work in the strong-coupling regime.

As mentioned above, the early CQED experiments has been performed with Fabry-Perot cavities formed by rather massive mirrors. Several new structures with small-volume micro-cavities have emerged in recent years. These are routinely produced in large arrays and by construction can allow for efficient photon tunnelling between neighbouring cavities. In addition, the strong-coupling regime with cooperativity factors much larger than unity has been achieved in several of these devices.

1.2.1 Fabry-Perot and fiber based cavities

The optical Fabry-Perot cavity consisting of two separated parallel mirrors is the most conventional cavity system. In such a cavity, a standing-wave electromagnetic field can exist for a long time and interact with an atom (or spin) trapped inside the resonator. With an appropriate design, a Fabry-Perot cavity can achieve high quality factors $Q \sim 3 \times 10^8$ [107]. However, traditional bulk-optics based cavities were limited by a relatively large mode volume and very limited prospect for scalability. Since the mid-2000 arrays of spherical micromirrors etched on a silicon substrate and coated with a high-reflectivity multilayer dielectric mirror have been developed [110]. A cavity is formed between this mirror and another planar mirror glued on the tip of an optical fibre. The spherical mirrors have a typical radius of curvature in the range $\sim 100-300\mu m$, which allows the cavity mode to be perfectly matched to the fibre. Such a cavity has a mode volume at least an order of magnitude smaller than bulk optics designs. Working with cold Rb atoms from a magneto-optical trap (MOT) dropped in free fall, these cavities are been used as a fast, efficient single-atom detector [111] and as a single photon source [112]. Here an pump laser passing transversely through the cavity is used to trigger photon emission into the cavity mode and hence into the single-mode fiber.
Large regular arrays of spherical mirrors can be created with controllable sizes and spacings and they may contain several hundred mirrors. Their extremely small mode volume leads to a large single-photon Rabi frequency, and light is conveniently coupled into and out of the cavities via the fibres themselves. With these cavities Purcell factor or cooperativity of ~ 40 has been achieved.
Fibres can also be integrated in large, commercially available arrays, or into a waveguide chip; thus it should be possible to operate a large number of cavities simultaneously.

1.2.2 Microsphere and microtoroidal cavities

Another class of micro-cavities that are routinely produced in large arrays and which have very high Q-factors are silicon structures of either a spherical [113], or a toroidal shape [114]. These cavities, with very small mode-volume, are closed silicon sphere or toroids fabricated by melting the tip of an optical fibre and typically they are carried by a thin pillar in their centre. Light can be trapped in the so called whispering gallery modes (WGMs)[4] if the refractive index of the material of the sphere is larger than the one surrounding it. Successive total internal reflections off the concave inner surface confine the light into a thin ring close to the equator. These high-Q ring modes have been observed and studied extensively in droplets [115]. It

[4]WGMs had first been observed in the gallery of the cupola of St. Paul's Cathedral in London. A whisper spoken close to the wall can be heard all the way along the gallery, some 42 m to the other side. Lord Rayleigh was the first to identify the refocusing effect of the curved surface as the sound travels along the gallery. He also conjectured the existence of the thus called whispering gallery modes. He suggested that such modes of the electromagnetic field could find some applications due to the extreme confinement of the field.

was soon recognised that the field enhancement caused by the strong confinement of the light in these modes combined with their high quality factors could lead to strong CQED effects. Their Q-factor can be as high as 10^8 with photon storage times of the order of one microsecond [116]. Clearly such a system is ideally suited for the observation of nonlinear optical effects and CQED experiments. Very efficient and highly tunable coupling of photons into and from those cavities is possible via tapered optical fibres that are placed close to their surface [117]. Here, the evanescent field of both cavity and fibre overlap and photons can hop between them. The photon hopping rate can thereby be controlled very accurately via the separation between cavity and fibre. Quantum dots can be deposited on the surface and coupled to the evanescent field, or a cold atomic ensemble can be brought in close proximity; the relatively large distance between cavities allows individual addressing of the emitters. These cavities can interact with atoms or quantum dots in a strong-coupling regime with cooperativity factors ~ 50 [108] if the atoms are placed close to the cavity surface and interact with the evanescent field.

1.2.3 Photonic band-gap cavities and quantum dots

Photonic crystals (PC) are materials patterned with a periodicity in dielectric constant, which can create a range of 'forbidden' frequencies called photonic band-gap. Photons with energies lying in the band-gap cannot propagate through the medium. PCs can be fabricated for one, two, or three dimensions. One-dimensional PCs can be made of layers deposited or stuck together. Two-dimensional ones can be made by photolithography, or by drilling holes in a suitable substrate.

Similarly to the wavefunction of an electron inside a periodic potential imposed by the crystal lattice, it can be shown that electromagnetic field inside such a periodic dielectric medium can be expressed in terms of the electromagnetic eigenmodes which satisfy the Bloch theorem, and are therefore referred to as Bloch modes. The allowed electromagnetic modes in such a medium can be obtained as the solutions of the Maxwell's equation (or wave equation) for the electric field with a periodic dielectric constant. Therefore, given the frequency ω, we can solve the wave equation in such a periodic medium to find the wavevector $\mathbf{k}$ and the allowed Bloch modes of the system at that frequency[5]. The dispersion relation $\omega(\mathbf{k})$ is also called *photonic band diagram*. If there is a whole band of frequencies in which the wave equation inside such a periodic crystal has no solutions for any real $\mathbf{k}$, such a band of frequencies is called *photonic band-gap*. Bloch modes in this range of frequencies do not exist, implying that the electromagnetic waves with frequencies within the photonic band gap cannot propagate through the PC. In other words, the PC behaves as a mirror for electromagnetic waves with frequencies inside the photonic band gap. Such reflection could also be viewed as the distributed Bragg reflection of the electromagnetic wave from the interfaces between regions with different dielectric constants. In 1D and 2D structures photonic band gap occurs only for waves propagating in a

[5]We carry out a similar calculation in Sec. 3.1 to obtain the dispersion relation and the photon-hopping rate for a system of coupled cavities which can be realized within a PC structure.

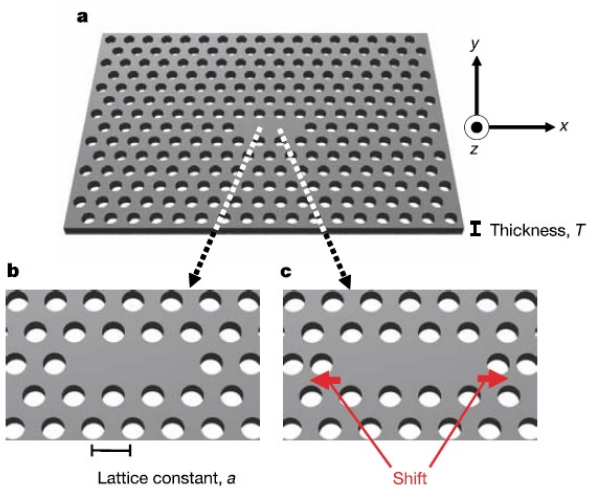

Figure 1.5: Photonic high-Q nanocavities using a 2D photonic-crystal slab. (a) Schematic of the basic cavity structure having a triangular lattice of air rods with lattice constant a ($\sim 0.42\mu m$). The thickness T of the slab and the radius R of the air rods are $0.6a$ and $0.29a$, respectively. (b) Starting cavity structure with three missing air rods in a line. (c) Designed cavity structure created by displacing the air rods at both edges to obtain an ultrahigh Q/V value. From [120].

certain direction or set of directions in which the periodicity of the dielectric constant occurs. 3D PCs, however, can lead to a complete photonic band-gap, meaning that in a certain frequency region the wave propagation is prohibited through the crystal in any direction in space and for any polarization. In 2D structures, holes may be drilled in a substrate that is transparent to the wavelength of radiation that the ban-dgap is designed to block [118]. Triangular and square lattices of holes have been successfully employed. The first 3D structure dates back to 1991 when Yablonvitch [119] was able to produce a microwave PC by drilling an array of holes in a transparent material, where the holes of each layer form an inverse diamond structure.
In their most common form, PCs are thin slabs ($\sim 100nm$) of high-index dielectric patterned with a regular array of holes. A missing row of holes defines a waveguide and a few missing holes a cavity. A nanocavity can be created in a photonic band gap material by producing a localized defect in the structure of the crystal, in such a way that light of a particular frequency cannot propagate outside the defect area. For example, a defect-microcavity in an hexagonal 2D PC lattice of air holes is formed by changing the radius or the position of a single hole, or by changing its refractive index. In Fig (1.5) is sketched the scheme for a nanocavity realized using a 2D silicon based PC slab with $Q = 4.5 \times 10^4$ and volume $V = 7 \times 10^{-14} cm^3$ [120]. Here the photonic band-gap effect is used for light confinement in the in $x - y$ plane direction and total internal reflection (TIR), at the interface between the slab and the air clad, in the vertical z direction. The basic structure is composed of Si with a triangular lattice of air 'rods' with lattice constant $a = 0.42\mu m$. The initial structure of the cavity is made with three missing air rods in

a line and, with this structure, light can be confined by Bragg reflection for the in-plane directions. If the air rods at both edges of the cavity are shifted, the Q/V ratio is significant increased [Fig (1.5c)]. In this way, localized modes with frequencies within the photonic band-gap are producted and these have to be evanescent inside the photonic crystal, i.e. they have to decay exponentially away from the defect [see Fig (1.6b)]. In other words, the defect behaves as an optical cavity, and the surrounding PC represents mirrors surrounding the cavity. Large arrays of such nanocavities have been produced [122] and photon hopping between neighbouring cavities has been observed in the microwave and optical domains [121].

Quantum dots (QD) are small nanostructures where electrons are trapped in a potential-well and have discrete energy levels. These structures are made usually by sandwiching a tiny chunk of one type of semiconductor with a smaller band gap inside another semiconductor with a larger band gap, thereby producing potential barrier for electrons and holes in three dimensions. For example, InAs QD embedded inside GaAs are formed by self-assembly during a growth process called molecular beam epitaxy (MBE), as a result of lattice mismatch between InAs and GaAs [123]. This process of self-assembly of QD is known as Stransky-Krastanov growth. Since QD islands are formed by self-assembly, their locations are random, and there is a distribution of sizes and shapes, leading to fluctuations in the energies of transitions of different QD on the same wafer (inhomogeneous broadening). QDs exhibit discrete atomic like spectra and for this reason they are often referred to as artificial atoms. The discrete lines in their spectrum are produced by recombination of carriers (electrons and holes) occupying discrete energy levels in the conduction and valence bands.

QDs can be created inside PC nanocavities [124] and made to interact with the cavity mode to form a standard cavity QED system. The strong-coupling regime with cooperativity factors up to 70 has already been achieved in such systems. Due to the extremely small volume of the nanocavity, the Vacuum Rabi frequency can be extremely large, while spontaneous emission rates are very low. Fig (1.6a) shows a QD in a photonic band gap cavity [125] realized by means of MBE. Here the semiconductor heterostructure used for subsequent PC fabrication was grown on a semi-insulating GaAs substrate. The epitaxial structure consists of a $126nm$ GaAs slab incorporating a QD of InAs located precisely at the cavity electric field maximum. When tuned into resonance, the exciton and photon enter the strong-coupling regime of CQED (with cooperativty $\sim$ 10) and the photon stream from the cavity becomes antibunched. Other examples of CQED strong coupling regime in a similar structure can be found in [126, 127].

For all coupled cavity applications we will discuss later, current decay rates of PCs cavities remain a limiting factor. This is mainly due to the fact that most structures employ two-dimensional PC, as placing a QD into a three-dimensional structure is difficult. The difficulties to control the properties of individual quantum dots and to place them at desired locations could even pose a more significant problem.

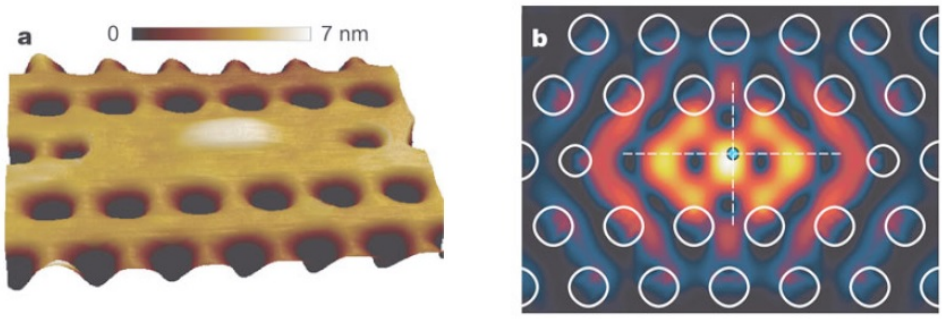

Figure 1.6: A quantum dot in a photonic band gap cavity. (a) AFM topography of a GaAs photonic crystal nanocavity aligned to a hill of material on the surface arising from a quantum dot buried 63 nm below. (b) Electric field intensity of the photonic crystal cavity mode showing that the location of the buried QD, indicated by the teal dot, overlaps the field maximum. From [125]

1.2.4 Superconducting stripline resonators and Superconducting qubits

Superconducting qubits are solid-state artificial atoms which are based on lithographically defined Josephson tunnel junctions. When sufficiently cooled, these superconducting devices exhibit quantized states of charge, flux or junction phase depending on their design parameters. This allows to observe coherent evolutions of their states. Experimentally, these circuits are fabricated on a micrometer scale and operated at mK temperatures. Thanks to their relatively large size they are easy to manipulate and control experimentally. Compared to normal harmonic oscillators formed by LC circuits, in SC qubits the energy-level separation becomes nonuniform by introducing a nonlinearity via Josephson junctions. This property allows one to encode a qubit in the lowest two levels of a SC circuit [128], so they offer the possibility to realize an effective two-level system.
The Cooper pair box (CPB) was among the first superconducting devices to demonstrate properties of quantum coherence, including evidence for quantum superposition of charge states and it was the first used to demonstrate coherent control of the quantum states of a qubit in a solid-state electronic device [129]. This device is composed of a tiny superconducting island coupled by a Josephson junction to a superconducting reservoir. The state of the qubit is determined by the number of Cooper pairs which occupy the box.
SC circuits have two important parameters: the Josephson coupling energy E_J and the electrostatic Coulomb energy E_C. According to their topology and physical parameters, SC qubits can be divided into three kinds: charge qubits (using a CPB based scheme, with $E_J/E_C < 1$), flux qubits (using the circulating supercurrent states in a loop and $E_J/E_C > 1$) and phase qubits (using the oscillatory states of the circuit and $E_J/E_C > 1$). These solid-state qubits can be controlled by the applied bias current, gate voltage, and microwave fields. Other two kinds of charge qubits are the Quantronium and the Transmon. These two circuits are modications of the

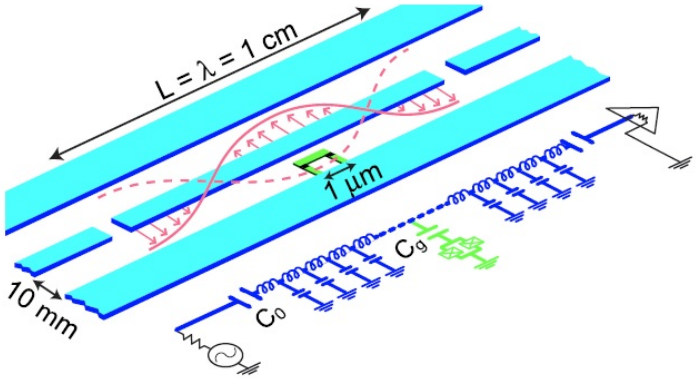

Figure 1.7: Schematic illustration of a typical coplanar waveguide (CPW) resonator used in circuit QED together with its discretized lumped-element equivalent circuit. The qubit lies between the center pin and the adjacent ground plane and is located at an antinode of the electric field, shown in this case for the full-wave resonance of the CPW. From [132]

CPB which improve dramatically the dephasing times of the original circuit [128]. The reason is that Quantronium and Transmon are more robust with respect to the charge noise, which is the biggest problem with this kind of circuits.
The energy eigenstates of a charge qubit based on a dc-SQUID setup can be defined by $|e\rangle = \cos(\theta/2)|0\rangle - \sin(\theta/2)|1\rangle$ and $|g\rangle = \sin(\theta/2)|0\rangle + \cos(\theta/2)|1\rangle$, with the transition frequency $\Omega = \sqrt{B_z^2 + B_x^2}$ for $\theta = \arctan(B_x/B_z)$. The eigenstates $|0\rangle$ and $|1\rangle$ represent the excess Cooper pairs on the superconducting island. The parameter $B_z = 4E_C(2n_g - 1)$, with the charging energy $E_C = e^2/2(C_g + 2C_J)$ and $n_g = C_g V_g/(2e)$, can be controlled by the voltage V_g applied to the gate capacitance C_g for a given capacitance C_J of the Josephson junction. The parameter $B_x = 2E_J \cos(\pi\Phi_x/\Phi_0)$, with the Josephson energy E_J, can be changed by an external magnetic flux through the SQUID loop [17, 130].
A superconducting stripline resonator, on the other hand, is a quasi-one-dimensional coplanar waveguide resonator (CPW), formed on a chip with a resonance frequency in the microwave range. CPW consists of a superconducting wire evaporated on an insulating substrate and has superconducting ground planes adjacent to it on the same surface [131], as shown in Fig (1.7). Such a system exhibits many standing wave resonances and each resonance is an independent harmonic oscillator equivalent to a simple LC oscillator. The discretized equivalent circuit for the CPW resonator is also shown in Fig (1.7), where two gap capacitors C_0 at each end play the role of the mirrors in a conventional optical cavity and the distance between these capacitors defines the characteristic frequencies of the normal modes. These capacitors couples the resonator to external transmission lines and if one assume open-circuit boundary conditions, the current (but not the voltage) vanishes at the ends of the resonator.
A high-quality microwave resonator can be coupled to SC qubits, which can be used to realize cavity-QED where the SC qubit is regarded as an artificial atom [133, 134]. Fig (1.7) shows

also an SC qubit lying between the center pin and the adjacent ground plane and is located at an antinode of the electric field. In general, the entire setup should be on the millimeter scale in order to fit the microwave frequency of the SC qubit, and it can be built by etching techniques. Recent experiments have shown that gigahertz photons can make up to a million bounces before being lost in a high-quality CPW resonator at low temperatures. An SC qubit can have a large effective transition dipole moment, e.g. the effective electric dipole moment of a charge qubit is 10^4 times larger than that of an alkali atom. Moreover, in a CPW resonator, the microwave field is confined to a much smaller volume than in a conventional 3D optical or microwave cavity. This can make the field strength in the quasi-1D cavity much larger (about 100 times or more) than in a 3D cavity and it may be obtained very high Q-factor ($> 10^8$) and cooperativity ($> 10^4$). However, SC qubits are sensitive to environmental noise from extrinsic and intrinsic decohering elements, which leads to short coherence times. For charge qubits, the dominant source of noise is due to charge fluctuations, such as trapped charges in the substrate and oxide layers of Josephson junctions. For flux and phase qubits, the noise from flux fluctuations dominates the decoherence.

A SC circuit involving a CPW resonator and a charge qubit was experimentally demonstrated by Wallraff et al. [135], where a strong electric coupling between a single photon and a charge qubit was achieved. In this setup, a charge qubit with two identical Josephson junctions is integrated into the ground planes of the transmission line at or near the antinode of the standing wave of the voltage on the SC wire for maximum coupling. They experimentally observed the coherent interaction of a superconducting two-level system with a single microwave photon in the strong coupling regime.

Flux qubits can also couple to CPW resonators via the induced magnetic field. A flux qubit placed at or near an antinode of the standing wave of the current on the SC wire can strongly couple to the SC resonator via the mutual inductance. In such a SC circuit, the vacuum Rabi splitting in the transmission spectrum was observed, which means that strong coupling was achieved. In [136] and [137], the inductive coupling between the flux qubit and the resonator was be enhanced and the system was bring to the ultrastrong-coupling regime.

Chapter 2

The Green's function approach

A Cavity represents a particular environment for the atom confined in it. Different methods can be applied to the study of the time evolution of a TLS initially prepared in the upper state and coupled with a radiation reservoir of arbitrary mode structure. The most general approach, already seen in the previous chapter, is the master equation. In the particular case of an atom decaying in free space the other most well-known methods are the Wigner-Weisskopf theory and Fermi's Golden Rule approach.
Here we summarize the resolvent operator or Green's function [30, 89, 90], a method that has proven to play a large role in many body theory, perturbation theory, and even in the development of modern quantum mechanics. This is a very convenient tool for the study of the dynamics for problems with a well defined initial state and a total time-independent Hamiltonian. The method is nonperturbative and lends itself to a systematic development of perturbation theory. Its description and some simple application discussed below will be a starting point to analyze, in the next chapter, the problem of a TLS decaying in a finite-band reservoir of modes, in particular the specific case of an environment consisting of an array of coupled cavities described by a tight binding Hamiltonian. The Green's function provides a full description of the system's spectrum and, at the same time, allows to obtain the time evolution of all probability amplitudes. Moreover, it allows to easily solve many problems, such as in Scattering Theory, for which the Hamiltonian consists of an unperturbed term, whose properties are assumed known, which adds a second term that represents a perturbation or, as we will see below, a defect.
The first section begin with deriving and stating some useful properties of time-independent Green's functions. In the second section, after introducing the main features of the corresponding time-dependent operator, we present the power of the method analyzing the dynamics for a TLS placed in a generic reservoir of modes. The Green's function approach is well suited to the study of the single excitation decay and allows also a direct analysis of the Markovianity of the process. Moreover, we apply the resolvent operator method to the particular cases of an atom decaying into the free space and into a QED cavity environment, analyzing, in the latter case, the different cavity regimes already seen. In the last section the method is applied to the study

of specific tight-binding Hamiltonians, a good starting point to introduce the problem of a TLS interacting with a coupled cavity array. We provide at the end the mathematical tools needed to analyze, in the next chapter, the photon localization and the scattering problem for this system.

2.1 Fundamental properties of the time-independent Green's function

A Green's function is the solution of an inhomogeneous differential equation of the form:

$$[z - \hat{H}(r)]G(r, r'; z) = \delta(r - r') \tag{2.1}$$

in which z is a complex parameter. In our paricular case, we now consider the time-independent Schrödinger equation with Hamiltonian $\hat{H}(r)$ expressed in the r-representation. The two-value Green's function $G(r, r'; E)$ satisfies the same boundary conditions[1] as the wavefunction $\psi(r)$, solution of the Schrödinger equation $[E - \hat{H}(r)]\psi(r) = 0$. Indicating with $\phi_n(r)$ the eigenstates of $\hat{H}$ in the r-representation and with E_n the corresponding eigenvalues, the Green's function can be expressed as:

$$G(r, r'; z) = \sum_n \frac{\phi_n(r)\phi_n(r')}{z - E_n} \tag{2.2}$$

We can define a general Green operator $\hat{G}(z)$ such that the above Green's function reads $G(r, r'; z) = \langle r|\hat{G}(z)|r'\rangle$, thus the Green's operator associated with the Hamiltonian $\hat{H}$ is:

$$\hat{G}(z) = \sum_n \frac{|\phi_n\rangle\langle\phi_n|}{z - E_n} = \frac{1}{z - \hat{H}} \tag{2.3}$$

In general the spectrum of $\hat{H}$ contains both discrete and a continous eigenvalues. For the systems which we will discuss in this chapter and in the next, the continous spectrum is always associated with unbound eigenstates. Since all eigenvalues of the Hermitian operator $\hat{H}$ are real, the associated Green's operator defined above is an analytic function on the complex z-plane except at those points or portions of the real z-axis that correspond to the spectrum. Separating the Green's function in a discrete and continous-spectrum component, we can rewrite the definition (2.3) as:

$$\hat{G}(z) = \sum_n \frac{|\phi_n\rangle\langle\phi_n|}{z - E_n} + \int dc \frac{|\phi_c\rangle\langle\phi_c|}{z - E_c} \tag{2.4}$$

[1] i.e. continuity of ψ and $\nabla\psi$ and finite or zero value at infinity.

in which we indicate with $|\phi_n\rangle$ the eigenstates associated with the discrete eigenvalues E_n and with $|\phi_c\rangle$ the ones associated with the continuous band of the spectrum, labeled by the index c. From the last equation it can be seen that $\hat{G}(z)$ exhibits simple poles at the position of the discrete eigenvalues (the inverse is also true) and, for z belonging to the continuous spectrum, it usually exists but it is not uniquely defined because one can add to any particular $\hat{G}$ the general solution of the homogeneous equation corresponding to (2.1). In this case it is convenient to define two Green's functions as the two side limits of $G(r, r'; z = E_c)$, i.e.:

$$G^{\pm}(r, r'; z) = \lim_{s \to 0^+} G(r, r'; z \pm is) \tag{2.5}$$

These limits exist but are different from each other, thus the continuous spectrum produces a *branch cut* in $\hat{G}(z)$ along parts of the real z-axis. The operator $\hat{G}^+(E)$ is also known as *resolvent operator*. Using the identity:

$$\lim_{\eta \to 0^+} \frac{1}{x \pm i\eta} = \mathcal{P}\left(\frac{1}{x}\right) \mp i\pi\delta(x) \tag{2.6}$$

with $\mathcal{P}$ denoting the principal value of the integral and (2.4), we can express the discontinuity $\tilde{G}(r, r'; z) = G^+(r, r'; z) - G^-(r, r'; z)$ as:

$$\tilde{G}(r, r'; E) = -2\pi i \left[\sum_n \delta(E - E_n)\phi_n(r)\phi_n^*(r') + \int dc\, \delta(E - E_c)\phi_c(r)\phi_c^*(r') \right] \tag{2.7}$$

The knowledge of the Green's function $G(r, r'; z)$ allows us to obtain immediately the solution of the general inhomogeneous equation:

$$[z - \hat{H}(r)]u(r) = f(r) \tag{2.8}$$

where $f(r)$ is a given function and the unknown function $u(r)$ satisfies the same boundary conditions as $G(r, r'; z)$. By taking into account (2.1), we obtain the following solution[2] of (2.8):

$$u(r) = \begin{cases} \int G(r, r'; z) f(r') dr', & z \neq \{E_n\}, \\ \int G^{\pm}(r, r'; z) f(r') dr' + \phi(r), & z = E_c. \end{cases} \tag{2.9}$$

where $\{E_n\}$ represents the set of all discrete eigenvalues, E_c belongs to the continuous spectrum of $\hat{H}$ and $\phi(r)$ is the general solution of the corresponding homogeneous equation. If z coincides with a discrete eigenvalue of $\hat{H}$ there is no solution of (2.8), unless f(r) is orthogonal to all

[2] If $u(r)$ describes physically the response of a system to a source $f(r)$, then $G(r, r'; z)$ describes the response of the same system to a unit point source located at r'. The physical meaning of the first equation in (2.9) is that the response to the general source $f(r)$ can be expressed as the sum of the responses to point sources distributed according to $f(r)$.

eigenfunctions associated with that eigenvalue.
Below we will use the following fundamental properties of the Green's function:

(i) The poles of $\hat{G}(z)$ coincide with the discrete eigenenergies corresponding to $\hat{H}$ and vice versa;

(ii) The residue at each pole E_n of G(r,r';z) is equal to $\sum_{i=1}^{\theta_n} \phi_i(r)\phi_i(r')$, where the summation runs over the θ_n degenerate eigenstates corresponding to the discrete eigenenergy E_n;

(iii) The branch cut of $\hat{G}(z)$ along the real z-axis coincide with the continuous spectrum of $\hat{H}$ and vice versa.

In particular the property (ii) can be used to get the generic expression for the projector over the eigenstate $|\phi_n\rangle$. If the associated eigenenergy E_n is non-degenerate, the projector is:

$$|\phi_n\rangle\langle\phi_n| = \lim_{z\to E_n}(z - E_n)\hat{G}(z) \tag{2.10}$$

In many cases, as well as in all systems of our interest, the Hamiltonian $\hat{H}$ can be separated into an unperturbed part $\hat{H}_0$ and a perturbation term, i.e. $\hat{H} = \hat{H}_0 + \hat{H}_1$. All eigenenergies and eigenfunctions of $\hat{H}_0$ are assumed to be known. The Green's function associated with $\hat{H}$ can be solved by calculating the Green's operator $\hat{G}_0(z)$ corresponding to $\hat{H}_0$ and expressing $\hat{G}(z)$ in terms of $\hat{G}_0(z)$ and $\hat{H}_1$. From the Green's operator $\hat{G}(z)$, associated with the total Hamiltonian, we can extract the informations about the eigenvalues and eigenfunctions of $\hat{H}$. Using the definitions $\hat{G}_0(z) = (z - \hat{H}_0)^{-1}$ and $\hat{G}(z) = (z - \hat{H}_0 - \hat{H}_1)^{-1}$, it is straightforward to rewrite $\hat{G}(z)$ in the following form:

$$\hat{G}(z) = \frac{\hat{G}_0(z)}{1 - \hat{G}_0(z)\hat{H}_1} \tag{2.11}$$

Expanding the operator $(1 - \hat{G}_0\hat{H}_1)^{-1}$ in power series it is possible to relate $\hat{G}(z)$ to $\hat{G}_0(z)$ and $\hat{H}_1$ as follows:

$$\begin{aligned} \hat{G}(z) &= \hat{G}_0(z) + \hat{G}_0(z)\hat{H}_1\hat{G}_0(z) + \hat{G}_0(z)\hat{H}_1\hat{G}_0(z)\hat{H}_1\hat{G}_0(z) + \dots , & (2.12)\\ &= \hat{G}_0(z) + \hat{G}_0(z)\hat{H}_1\hat{G}(z) , & (2.13) \end{aligned}$$

The above equation is an inhomogeneous integral equation for $\hat{G}(z)$. This expansion allows to obtain the eigenstates associated with the continuous spectrum of $\hat{H}$ in a very simple way. The time-independent Schrödinger equation for a system with Hamiltonian $\hat{H} = \hat{H}_0 + \hat{H}_1$ can be written as:

$$(E - \hat{H}_0)|\psi\rangle = \hat{H}_1|\psi\rangle \tag{2.14}$$

in which we suppose that the energy E belongs to the continuous spectrum of both[3] $\hat{H}$ and $\hat{H}_0$. According to (2.9), it is possible to consider (2.14) as an inhomogeneous equation whose general solution is:

$$|\psi^{\pm}\rangle = |\phi\rangle + \hat{G}_0^{\pm}\hat{H}_1|\psi^{\pm}\rangle \tag{2.15}$$

where $|\phi\rangle$ is the general solution of the associated homogeneous of (2.14), i.e. the eigenstate of the unperturbed Hamiltonian $\hat{H}_0$ with energy E. In most physical applications the solution $|\psi^{-}\rangle$ is discarded on physical ground since it does not correspond to any physically meaningful situation. In the r-representation (2.15) is an integral equation[4] for the unknown $|\psi^{\pm}\rangle$. By iterating (2.15) we have:

$$|\psi^{\pm}\rangle = |\phi\rangle + \hat{G}_0^{\pm}\hat{H}_1|\phi\rangle + \hat{G}_0^{\pm}\hat{H}_1\hat{G}_0^{\pm}\hat{H}_1|\phi\rangle + \dots \tag{2.16}$$

Finally, using (2.12), from (2.16) with some algebra it is possible to get the following useful expression:

$$|\psi^{\pm}\rangle = |\phi\rangle + \hat{G}^{\pm}\hat{H}_1|\phi\rangle \tag{2.17}$$

2.2 Time-dependent Green's function: the dynamic of a TLS in a structured reservoir

In the previous chapter we introduced the problem of a TLS in a generic reservoir of modes in order to analyze the dynamic of such a system into the environment of a cavity QED. Here we apply the time-dependent Green's function approach or *resolvent operator* method to study the generic dynamic of a 'TLS + bath' system, described by the Hamiltonian (1.1). In particular we treat the specific case of a TLS in free space and also review its evolution inside a cavity. From now on we will use $\hbar = 1$ units. For problems with a well defined initial state and total time-independent Hamiltonian, the resolvent operator proves to be a powerful tool for investigating the dynamics of the system. We can use the Green's function to calculate the evolution operator restricted to the TLS dynamic with a given initial condition. If we look at the spontaneous emission, we consider $|\Psi(0)\rangle = |e\rangle|0\rangle$, i.e. at $t = 0$ the atom is in its upper state and there are no photons in the bath. So we start at $t = 0$ with one excitation and, since the RWA

[3] In many cases, in all those of our interest, it is possible to choose $\hat{H}_0$ and $\hat{H}_1$ in such a way that the continuous spectrum of $\hat{H}$ coincides with that of $\hat{H}_0$.

[4] the well-known *Lippman−Schwinger* equation.

Hamiltonian (1.1) conserves the total number of quanta, the only other possible states entering in the dynamic are the $|g\rangle|k\rangle$s, with the atom in its ground state and a photon in the field mode k. For brevity we indicate the initial state simply with $|e\rangle$ and the field states with $|k\rangle$. Of course $|g\rangle$, $|e\rangle$ and $\{|k\rangle\}$ are eigenstates of the unperturbed Hamiltonian $\hat{H}^r + \hat{H}^a$ in (1.1) and from the same equation we have $\langle k|\hat{H}^{coup}|e\rangle = g_k$, i.e. $\hat{H}^{coup}$ couples only $|e\rangle$ with the generic field state $|k\rangle$, the corresponding matrix element being the coupling constant g_k (considered real without loss of generality). The state of the 'atom + bath' system at the generic time t is:

$$|\Psi(t)\rangle = \hat{U}(t)|\Psi(0)\rangle = \hat{U}(t)|e\rangle \tag{2.18}$$

which defines the time evolution operator $\hat{U}(t)$ associated with the Hamiltonian (1.1):

$$\hat{U}(t) = e^{-i\hat{H}t} \tag{2.19}$$

The time evolution operator $\hat{U}(t)$ can be obtained from the time-independent Green's operator $\hat{G}(z)$. As in the case of the time-independent Schrödinger equation, the time-dependent problem can be associated with a corresponding Green's function differential equation. In this case the Green's function associated with a first-order (in time) partial differential equation of the form $i\partial\phi/\partial t - \hat{H}(r)\phi = 0$ is defined as solution of the following equation:

$$\left[i\frac{\partial}{\partial t} - \hat{H}(r)\right] G(r, r', t, t') = \delta(r - r')\delta(t - t') \tag{2.20}$$

Here the time-dependent Green's function $G(r, r', t, t')$ is a function of the difference $t - t'$ that, for the sake of simplicity and without loss of generality, we indicate simply as t. Expressing $G(r, r', t)$ in terms of its Fourier transform:

$$G(r, r', t) = \frac{1}{2\pi}\int_{-\infty}^{+\infty} d\omega' \Gamma(r, r'; \omega') e^{-i\omega' t} \tag{2.21}$$

and substituting in (2.20) we obtain:

$$[z - \hat{H}(r)]\Gamma(r, r'; \omega) = \delta(r - r') \tag{2.22}$$

that is the same of (2.1). Hence we deduce that $\Gamma(r, r'; \omega) = G(r, r'; \omega)$, i.e. the Fourier transform of the time-dependent Green's function corresponds to the Green's function of the associated time-independent problem. But we have seen that $G(r, r', \omega)$ may present singularities for real ω (poles and/or branch cuts), thus definition (2.21) must be modified by using a limiting procedure of the type:

$$G^C(r, r', t) = \lim_{C \to \omega_R} \frac{1}{2\pi}\int_{-\infty}^{+\infty} d\omega' G(r, r'; \omega') e^{-i\omega' t} \tag{2.23}$$

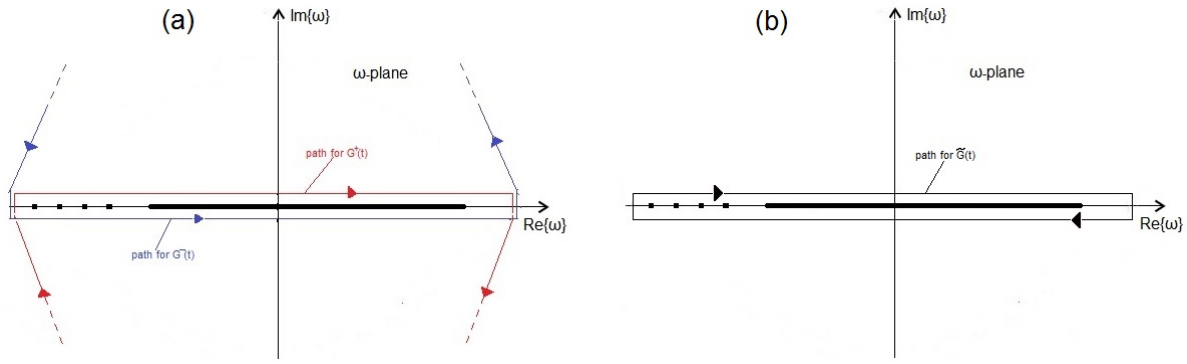

Figure 2.1: Integration paths in the $\omega-$plane to get (a) $G^+(r,r',t)$ (red path) and $G^-(r,r',t)$ (blue path), (b) $\tilde{G}(r,r',t) = G^+(r,r',t) - G^-(r,r',t)$. The paths encircle all singularities of the integrand, all lying on the real $\omega-$axis.

obtaining infinitely many $G^C(r,r',t)$s depending on how the contour C approaches the real $\omega-$axis ω_R. Using (2.5) we can define $G^\pm(r,r',t)$ following the two paths sketched in Fig (2.1a):

$$G^\pm(r,r',t) = \frac{1}{2\pi}\int_{-\infty}^{+\infty} d\omega' G^\pm(r,r';\omega')e^{-i\omega' t} \tag{2.24}$$

with $G^\pm(r,r';\omega)$ defined in (2.5). These are the only two choices of physical interest. The red (blue) path for $G^+(r,r',t)$ (for $G^-(r,r',t)$) approaches ω_R from the upper half-plane (from the lower one). For $t > 0$ ($t < 0$) we can close the integration path with an infinite semicircle in the lower (upper) half-plane. Thus it results that $G^+(r,r',t<0) = 0$ and $G^-(r,r',t>0) = 0$. We can use the difference $\tilde{G}(t) = G^+(t) - G^-(t)$ to calculate the evolution operator defined in (2.19). This difference is the time-dependent Green's function corresponding to the integration path sketched in Fig (2.1b). Obviously, substituting with t the difference $t - t'$ in (2.20), we automatically count the time from the $t = 0$ instant corrensponding to the initial condition, compatibly with (2.19). Using (2.7) and (2.24), the time-dependent Green's function difference is calculated as follows:

$$\begin{aligned}\tilde{G}(r,r',t) &= \frac{1}{2\pi}\int_{-\infty}^{+\infty} d\omega' \tilde{G}(r,r';\omega')e^{-i\omega' t} = \\ &= -i\int_{-\infty}^{+\infty} d\omega' \sum_n \delta(\omega' - E_n)\phi_n(r)\phi_n^*(r') = -i\sum_n e^{-iE_n t}\phi_n(r)\phi_n^*(r')\end{aligned} \tag{2.25}$$

As in the time-independent case, the time-dependent Green's function defined above can be seen as the $\langle r|\ldots|r'\rangle$ matrix element of a given Green's operator. This turns out to be:

$$\hat{\tilde{G}}(t) = -i \sum_n e^{-iE_n t} |\phi_n\rangle\langle|\phi_n| = -ie^{-i\hat{H}t} \tag{2.26}$$

i.e. the time-dependent Green's operator is proportional to the time-evolution operator $\hat{U}(t) = e^{-i\hat{H}t}$, hence:

$$\hat{U}(t) = i\hat{G}^+(t), \qquad t > 0 \tag{2.27}$$

Using $|\phi(t)\rangle = \hat{U}(t)|\phi(0)\rangle$, valid only for $t > 0$, from (2.27) transforming to the r-representation we obtain the solution of the time-dependent Schrödinger equation in the following form:

$$\phi(r,t) = i \int dr' G^+(r,r',t)\phi(r',0) \tag{2.28}$$

that is, the time-dependent Green's function is a kernel that allows to propagate the state from $t = 0$ to the generic time t, hence the name of *propagator*. In (2.27) we found a very important result and it will allow us to obtain the evolution of a part of the entire system by Fourier-transforming a corresponding matrix element of the time-independent Green's operator. In (2.25) we took into account only the summation over discrete spectrum present in (2.7), but it can been shown that (2.27) is a general result, valid for Hamiltonians with continuous and/or discrete spectrum.

Let us apply the resolvent operator to the dynamics of a TLS interacting with a single-mode radiation field in the RWA, with total Hamiltonian given in (1.1). As already mentioned, the 'atom+reservoir' state at time t is $|\Psi(t)\rangle = \hat{U}(t)|e\rangle$ with the initial condition $|\Psi(0)\rangle = |e\rangle$. We work in the single-excitation sector of the Hilbert space with basis $\{|e\rangle, \{|k\rangle\}\}$ and for the moment don't specify the dispersion ω_k for the field modes and the constants g_k. From now on, we set the zero of the energies on the ground level of the TLS, hence (1.1) is recasted as:

$$\hat{H} = \hat{H}^r + \hat{H}^a + \hat{H}^{coup} = \sum_k \omega_k \hat{a}_k^\dagger \hat{a}_k + \omega_a |e\rangle\langle e| + \sum_k g_k \left(\hat{a}_k^\dagger \hat{\sigma}_- + \hat{a}_k \hat{\sigma}_+\right) \tag{2.29}$$

The time-independent Green's operator associated to the unperturbed part $\hat{H}_0 = \hat{H}^r + \hat{H}^a$ of (2.29) reads:

$$\hat{G}_0(z) = \frac{|e\rangle\langle e|}{z - \omega_a} + \sum_k \frac{|k\rangle\langle k|}{z - \omega_k} \tag{2.30}$$

For the moment we consider discrete the set $\{|k\rangle\}$. Using the expansion in (2.12), it is possible to calculate all matrix elements of the complete Green's operator $\hat{G}(z)$ on the $\{|e\rangle, \{|k\rangle\}\}$ basis. What it has been said so far for the r-representation can be applied to any basis. For example, $\langle k|\hat{G}^+(t)|e\rangle$ describes the propagation of the initial excitation from $|e\rangle$ at $t = 0$ to $|k\rangle$ at time t or viceversa. In other words this matrix element represents the probability amplitude of finding at

time t the excitation as $k-$mode photon when at $t = 0$ the state is $|e\rangle$ or viceversa. The atomic probability amplitude with the same initial condition is calculated as:

$$u_e(t) = i\langle e|\hat{G}^+(t)|e\rangle = \lim_{s\to 0} \frac{i}{2\pi} \int_{-\infty}^{+\infty} dz G_{ee}(z + is)e^{-izt} \tag{2.31}$$

in which we used (2.5), (2.27), (2.24). The time-independent matrix element $G_{ee}(z) = \langle e|\hat{G}(z)|e\rangle$ in (2.31) reads [30]:

$$G_{ee}(z) = \frac{1}{z - \omega_a - \sum_k \frac{|g_k|^2}{z-\omega_k}} \tag{2.32}$$

To derive the atomic probability amplitude from (2.31) we need to know the exact expressions for g_k and ω_k, but from (2.32) we can deduce some general considerations. The function $W(z) = \sum_k \frac{|g_k|^2}{z-\omega_k}$ in the denominator of (2.32) is known as *shift-width* or *self-energy* and if the spectrum of $\hat{H}$ is continuous, characterized by the continuous variable k, we have to replace the summation with an integral. If $W(z)$ is approximately constant for z varying into the range for which $G_{ee}(z)$ is substantially non-zero, we can replace the shift-width function in (2.32) with a complex constant W_0 and so the resulting expression for $G_{ee}(z)$ has a simple pole at $z = \omega_a + W_0$. We refer to this as *pole approximation* and, when it is valid, the real part of W_0 represents the vacuum shift of the state $|e\rangle$, while the imaginary part is the spontaneous decay width, i.e. the emission rate of the transition $|e\rangle \to |g\rangle$. By inspecting (2.32), we can see that the pole approximation holds essentially if two conditions are verified: i) $W(z)$ must be a slowly varying function of z and ii) $|W(z)| \ll \omega_a$ for all z. In this case it is reasonable to approximate the shift-width function with $W_0 = W(\omega_a) = \sum_k \frac{|g_k|^2}{\omega_a-\omega_k}$, since the inversion integrand $G_{ee}(z)$ is very peaked at $z = \omega_a$.

2.2.1 Sponaneous emission of a TLS

As already seen in the previous chapter, the most general method to obtain the time evolution of a small system, as an atom or a two-level system, coupled to many modes of the radiation field (e.g. a thermal bath of harmonic oscillators) in the dipole and RW approximation is the master equation. If we indicate with $\hat{\rho}_a$ the reduced density matrix of the atom, the master equation (in Linblad form) reads:

$$\frac{\partial\hat{\rho}_a}{\partial t} = -\frac{i}{\hbar}\left[\hat{H}, \hat{\rho}_a\right] - \frac{\Gamma}{2}\left[\hat{\sigma}_+\hat{\sigma}_-\hat{\rho}_a + \hat{\rho}_a\hat{\sigma}_+\hat{\sigma}_- - 2\hat{\sigma}_-\hat{\rho}_a\hat{\sigma}_+\right] \tag{2.33}$$

The second term on the right-hand side describes the spontaneous emission process, in which the atom loses a photon into the continuum of field modes with rate Γ. We have neglected the

stimulated emission and absorption processes, assuming zero thermal occupation of the bath at the atomic resonance frequency ω_a (this condition, always verified at $T = 0$, is realistic at optical frequencies). The general system evolution is characterized by:

$$P_e(t) = \langle e|\hat{\rho}_a(t)|e\rangle = e^{-\Gamma t} \qquad \langle \hat{\sigma}_-(t)\rangle = \langle e|\hat{\rho}_a(t)|g\rangle = e^{-(\frac{\Gamma}{2}+i\omega_a)t} \tag{2.34}$$

The equations above show the well-know exponential decay of the excited state probability $P_e(t)$ with rate Γ and the atomic coherence oscillating at frequency ω_a and decaying at rate $\Gamma/2$ (the atom radiates as it decays). This statistical approach cannot provide informations about Γ, as it does not take into account how the atomic transition is coupled to each field mode.
The Green's function approach, as well as a microscopic derivation of the master equation [89], provides a more accurate description of the dynamics and allows to obtain the exact decay rate. An atom in free space can be seen as a small system coupled to a reservoir of infinitely many degrees of freedom which belong to a continuum. In this case, assuming the dispersion relation $\omega_k = ck$, we need to introduce the density of field modes, i.e. the summation in (2.32) must be replaced by an integral. For a given density $D(\omega)$, there are a total number of $D(\omega)d\omega$ modes at frequency ω. Thus the shift-width function reads:

$$W(z) = \int_0^\infty \frac{D_0(\omega)|g(\omega)|^2}{z-\omega} d\omega \tag{2.35}$$

In our case the particular environment is the vacuum with a density of modes, accounting for the two orthogonal polarizations, given by [83]:

$$D_0(\omega) = \frac{2V_q\omega^2}{3\pi^2c^3} \tag{2.36}$$

where V_q is the quantization volume and the well-known coupling constant dependence on the frequency is:

$$g(\omega) = \sqrt{\frac{\omega}{2\epsilon_0 V_q}} d_a \tag{2.37}$$

in which d_a is the atomic dipole matrix element. Of course the product $D_0(\omega)|g(\omega)|^2$ in the numerator of (2.35) no longer contains the quantization volume V_q. So we have all the elements to calculate the shift-width function in the pole approximation and then, from (2.32) and (2.31), to obtain the exact probability evolution. The former reads:

$$W_0 = \frac{|d_a|^2}{3\pi^2\epsilon_0 c^3} \lim_{\eta\to 0} \int_0^\infty \frac{\omega^3}{\omega_a + i\eta - \omega} d\omega \tag{2.38}$$

In the above equation $W_0 = \lim_{\eta\to 0} W(\omega_a + i\eta)$. In this way, using (2.6), we obtain:

$$W_0 = S_0 - i\Gamma_0 = \frac{d_a^2\omega_a^2}{3\pi c^3}\int_0^\infty \frac{\omega}{\omega-\omega_a}d\omega - i\frac{d_a^2\omega_a^3}{3\pi\epsilon_0 c^3} \tag{2.39}$$

Thus we can rewrite (2.31) as:

$$u_e(t) = \lim_{\eta\to 0}\frac{i}{2\pi}\int_{-\infty}^{+\infty} dx \frac{e^{-ixt}}{x+i\eta-\omega_a-W_0} \tag{2.40}$$

The smooth dependence of the vacuum density of states on ω, $D_0(\omega) \propto \omega^2$ in (2.36), ensures the applicability of condition i) in the above discussion, i.e. the shift-width function for an atom decaying into the vacuum is a slowly varying function and, if also condition ii) ($W(\omega_a) \ll \omega_a$) is verified, it can be replaced by the constant $W_0 = S_0 - i\Gamma_0$ given in (2.39). The real part S_0, as already discussed, represents the non-relativistic contribution to the vacuum shift of level $|e\rangle$ (for a realistic atomic transition this is not a complete result, since it needs to consider all contributions for all states with non-vanishing dipole matrix element with the state $|e\rangle$). By inserting Γ_0 in (2.40), regardless of S_0, we obtain the decaying exponential result, already found above with the master equation approach, but now we know the exact value of the rate:

$$P_e(t) = |u_e(t)|^2 = e^{-\Gamma_0 t} \qquad with \qquad \Gamma_0 = \frac{d_a^2\omega_a^3}{3\pi\epsilon_0 c^3} \tag{2.41}$$

We now mention briefly the physical meaning of the mathematical restrictions i) and ii) on the shift-width function. The $W(z) \ll \omega_a$ condition concernes with the equivalence of the resolvent method, in this specific case, with a lowest nonvanishing order perturbation theory, i.e. the first-order Born approximation for the restricted density matrix of the atom wich is valid if the coupling potential $\hat{H}^{coup}$ in (2.29) is treated perturbatively. More importantly, the requirement that $W(z)$ must be a slowly varying function of z implies that the emission of a photon into the continuum of the vacuum modes, due to the atomic de-excitation, is an event of which the environment loses memory instantly: this is the so-called *Markov approximation* and it is important to stress that from this it derives the exact exponential shape of the atomic decaying law. In the next chapters we will analyze in detail this implication for the case of a TLS decaying into the enviroment of a coupled QED-cavity array.

2.2.2 TLS in a cavity

Now we want to review the atom-cavity dynamics already seen in the previous chapter by means of the formalism we have outlined above. Here we consider only a closed, i.e. $\gamma = 0$, and high-Q cavity, characterized by a mode-width much lower than the mode-separation. We consider again the atom excited at $t = 0$ and, since the Hamiltonian is always of general form (2.29), we follow the same steps as above up to the point where we need to calculate the shift-width

function $W(z)$. Let ω_c be the central frequency of the cavity mode and Q its quality factor. We introduce the following Lorentzian spectral density of states inside a cavity of volume V:

$$D_c(\omega) = \frac{V}{\pi} \frac{k/2}{(\omega - \omega_c)^2 + k^2/4} \tag{2.42}$$

where the photon loss rate $k = \omega_c/Q$ has been introduced in the previous chapter. This spectral density describes well the finite-width cavity mode coupled to the external dissipative reservoir [30, 88]. Since $D_c(\omega)$ is a peaked function around $\omega = \omega_c$, we can assign the value $g = g(\omega_c)$ to the slowly varing $g(\omega)$ given in (2.37) [5]. Substituting $D_c(\omega)|g(\omega_c)|^2$ into (2.35) we have:

$$W_c(z) = \frac{g^2 k}{2\pi} \int_0^\infty \frac{1}{(\omega - \omega_c)^2 + \frac{k^2}{4}} \frac{d\omega}{(z - \omega)} \tag{2.43}$$

In this case, due to the peaked shape of $D_c(\omega)$, $W_c(z)$ is not a slowly varying function of z, thus it would be wrong to replace it with a constant in (2.32). With the spectral density (2.42) the pole approximation is no longer valid. We can calculate the integral in (2.43) on the complex $\omega-$plane with the aid of the residue theorem. Extending the integration to $-\infty$, after some algebraic manipulation, we obtain the following result:

$$W_c(z) = \frac{g^2}{z - \omega_c + ik/2} \tag{2.44}$$

Substituting this into (2.32), the G_{ee} matrix element is calculated as:

$$G_{ee}(z) = \frac{z - \omega_c + ik/2}{(z - \omega_a)(z - \omega_c + ik/2) - g^2} \tag{2.45}$$

which, through the change of variable $z \to z + \omega_c$ and recalling the definition of atom-cavity detuning $\delta = \omega_a - \omega_c$ given in the previous chapter, it is rewritten as:

$$G_{ee}(z) = \frac{z + ik/2}{(z - \delta)(z + ik/2) - g^2} \tag{2.46}$$

Unlike the open space case, $G_{ee}(z)$ now has two poles whose position at resonance is:

$$z_\pm = -\frac{k}{4}\left(i \pm \sqrt{\frac{16g^2}{k^2} - 1}\right) \tag{2.47}$$

The properties of the time-independent Green's function are quite general and a non-Hermitian Hamiltonian is characterized in general by a complex spectrum. The poles of $G_{ee}(z)$ in (2.47) are

[5] For a more rigorous calculation the vacuum Rabi frequency must be correct by a geometrical factor of order unity accounting for three-dimensional angular average of $|g(\omega_c)|^2$.

in agreement with the complex eigenvalues (with $n = 1$ and $\gamma = 0$) of the damped atom-cavity system given in (1.21). From the analysis of the different CQED regimes, we have seen that, by comparing g with a finite value of the damping rate k (and $\gamma \neq 0$ for open cavities), it is possible to determine the behaviour of $P_e(t) = |u_e(t)|^2$ with the certainty that, for sufficiently long times, the atomic population is lost. This property follows from the analysis of the Green's function for general (Hermitian or non-Hermitian) Hamiltonians. The poles with a positive imaginary part fall outside the contour of integration and thus do not contribute to the inversion integral (we recall that, for $t > 0$, $G^-(t) = 0$ and the inversion integral (2.31) is calculated from (2.24) choosing G^+). The complex poles with negative imaginary part lead to a transient dissipative behaviour and do not contribute in the long-time limit. The purely real poles, on the other hand, represent a stable nondecaying state of the system and thus determine the behaviour in the long-time limit. In our case we have neither real poles nor poles with $Im\{z\} > 0$ and the two complex poles in (2.47) have both negative imaginary part, in agreement with the damped behavior we expected. The behaviour of $u_e(t)$ will then depend on the ratio g/k and, by substituting (2.46) into (2.31) we obtain, for $\delta = 0$, the following atomic probability evolution:

$$P_e(t) = |u_e(t)|^2 = \frac{1}{2} e^{-\frac{kt}{2}} \left(1 + \cos(2g't)\right) \quad with \quad g' = \sqrt{g^2 - k^2/16} \tag{2.48}$$

If $k \gg g$, we have an exponential decay as in open space. In this case, the cavity energy damping is so fast, compared with the rate with which it is deposited by the atom, that it is as if the atom were radiating directly into the open space: this is the weak-coupling regime for cavity QED we have discussed in the previous chapter. On the contrary, if $g \gg k$, the atom exchanges its excitation with the cavity in the strong coupling regime at frequency $\approx 2g$ and the loss into the outside environment is comparatively slow. In this limit, in which the emitted photon survives sufficiently long to be reabsorbed and to cause oscillations between the populations of the excited and the ground states, the atom-photon dynamics is described with very good approximation by the Jaynes-Cummings model with $n = 0$. But whenever the damping rate k has a finite value, as it is clear from (2.48), the atom will end up in the ground state in the limit $t \to \infty$ and the cavity will be empty of energy. The Green's function approach reveals this as a rigorous consequence of the structure of the density of states. We have chosen a Lorentzian form in (2.42), but, for sufficiently large time, the atom will end up in its ground state assuming any form of density of states with wings extending to infinity, regardless g/k and δ. Moreover, if the atom is detuned from the cavity mode ($\delta \neq 0$), the situation differs quantitatively but not qualitatively. Also in this case the atom, although it is protected somewhat against decay, will eventually lose its inital excitation.

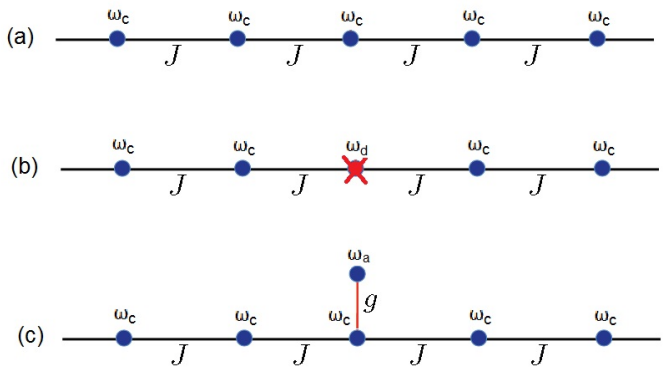

Figure 2.2: Equivalent network for: (a) An uniform infinite array of single-mode coupled cavities (CCA) with frequency ω_c and hopping rate J; (b) A CCA with a 'defect-mode' of different frequency $\omega_d = \omega_c + \omega_1$; (c) An uniform CCA with a cavity coupled at rate g to a TLS with transition frequency ω_a.

2.3 The Green's function for tight-binding Hamiltonians

Now we introduce the so-called tight-binding Hamiltonians (TBH), which have the general form:

$$\hat{H} = \sum_{x=-\infty}^{+\infty} \omega_x \hat{a}_x^\dagger \hat{a}_x + \sum_{x=-\infty}^{+\infty} \left(J_{x,x+1} \hat{a}_x^\dagger \hat{a}_{x+1} + h.c. \right) \tag{2.49}$$

We will use the bosonic tight-binding model to treat the photon hopping through an infinite array of single-mode coupled cavities (CCA). In (2.49) x is a discrete-position index, indicating the position of the cavity at point x through the array. The operator $\hat{a}_x^\dagger$ ($\hat{a}_x$) creates (annihilates) a photon of frequency ω_x at the xth cavity. By engineering the CCA in such a way that the field modes exhibit spatial overlap, photon hopping can occur between nearest-neighbor cavities. For the moment we consider only ideal lossless cavities, all with the same mode-frequency ω_c or at most with only one cavity with frequency different from the other. The second term on the right-side of (2.49) describes the photon hopping with rate generally dependent on the position $x, x+1$ of the pair of adjacent cavities. We will consider below only uniform hopping through the CCA at rate J. Since we are interested in the single-excitation transport, it is convenient to express the Hamiltonian in the single-excitation subspace, spanned by the orthonormal basis vectrors $|x\rangle$. These are the discrete version of the $|r\rangle$ vectors used in r-representation, hence $\langle x|x'\rangle = \delta_{x,x'}$.

At the end of the chapter we will apply the Green's function theory to the coupled TLS + CCA system, i.e. a TLS coupled to a single cavity of the uniform array, which we will cover in the rest of the thesis.

2.3.1 The uniform CCA

In the absence of defects, the uniform CCA in the single-excitation subspace, whose equivalent network is sketched in Fig (2.2a), is described by a tight-binding Hamiltonian of the form:

$$\hat{H}_0 = \omega_c \sum_{x=-\infty}^{+\infty} |x\rangle\langle x| + J \sum_{x=-\infty}^{+\infty} (|x\rangle\langle x+1| + |x+1\rangle\langle x|) \tag{2.50}$$

Hamiltonians in this form are well-known and widely used in solid-state physics to describe the electronic properties of crystalline solids. Of course, the infinite array and its Hamiltonian have traslational invariance and this property gives rise to a continuous spectrum with a lower bound, as in the case of the atom in open space, as well as with an upper bound. The Hamiltonian (2.50) can be diagonalized as:

$$\hat{H}_0 = \lim_{N\to\infty} \sum_{x=-N/2}^{N/2-1} \omega_k^N |\phi_k^N\rangle\langle\phi_k^N| \tag{2.51}$$

that is the thermodynamic limit ($N \to \infty$) of a finite closed array of N coupled cavities with the cyclic boudary conditions $|N/2\rangle = |-N/2\rangle$. For the finite case we have N extended eigenfunctions and eigenvalues of the form:

$$|\phi_k^N\rangle = \frac{1}{\sqrt{N}} \sum_{x=-N/2}^{N/2-1} e^{ikx}|x\rangle\,, \tag{2.52}$$

$$\omega_k^N = \omega_c + 2J\cos k\,, \tag{2.53}$$

$$k = \frac{2\pi n}{N} \quad (n = -N/2, -N/2+1, \ldots, N/2-1) \tag{2.54}$$

(2.53) and (2.52) represent, respectively, the free photon dispersion law and the associated field normal modes. The N possible photon energies fall in the frequency range $[\omega_c - 2J, \omega_c + 2J]$ and, in the thermodynamic limit, it becomes a continuous band (we omit the $N-$index) with the $k-$mode index in (2.54) varying continuously in the range $[-\pi, \pi]$

Knowing the expressions for $|\phi_k\rangle$ and ω_k, we can use the infinite CCA's Hamiltonian in its diagonal form (2.51) to express the associated Green's operator. From the definition (2.3) it reads:

$$\hat{G}_0(z) = \lim_{N\to\infty} \sum_k \frac{|\phi_k^N\rangle\langle\phi_k^N|}{z - \omega_k^N} \tag{2.55}$$

Thus the Green's function has only a branch cut corresponding to the continous spectrum of frequencies ω_k. Its generic matrix element in the $\{|x\rangle\}$ basis are:

$$G_0(x,x';z) = \langle x|\hat{G}_0(z)|x'\rangle = \lim_{N\to\infty}\frac{1}{N}\sum_k \frac{e^{ik(x-x')}}{z-\omega_k^N} = \frac{1}{2\pi}\int_{-\pi}^{\pi} dk \frac{e^{ik(x-x')}}{z-\omega_c-2J\cos k} \tag{2.56}$$

Here and in (2.55) we use the discrete eigenfunctions given in (2.52), for which $\langle x|\phi_k^N\rangle = e^{ikx}\sqrt{N}$, and in the thermodynamic limit we substitute $\frac{1}{N}\sum_k \to \frac{1}{2\pi}\int_{-\pi}^{\pi} dk$. To evaluate this integral, we observe first that it depends on the absolute value $|x-x'|$. It is possible to calculate it by transforming it into an integral over the complex variable $w = e^{ik}$ along the unit circle and using the method of residues, then the result is [90]:

$$G_0(x,x';z) = \frac{(-\tilde{z}+\sqrt{\tilde{z}^2-1})^{|x-x'|}}{\sqrt{(z-\omega_c)^2-4J^2}} \qquad for \quad |z-\omega_c|>2J\,, \tag{2.57}$$

$$G_0^{\pm}(x,x';z) = \frac{\mp i\left(-\tilde{z}\pm i\sqrt{1-\tilde{z}^2}\right)^{|x-x'|}}{\sqrt{4J^2-(z-\omega_c)^2}} \quad for \quad |z-\omega_c|\le 2J \tag{2.58}$$

with

$$\tilde{z} = \frac{z-\omega_c}{2J} \tag{2.59}$$

For $-1 \le \tilde{z} \le 1$, i.e for z belonging to the continuous band, the integral (2.56) is not well defined and $\hat{G}_0(z)$ has a branch cut, hence this condition gives the continuous spectrum of $\hat{H}$ which lies in the real $z-$axis between $\omega_c - 2J$ and $\omega_c + 2J$. In this case we have calculated in (2.58) the analytic continuations $G_0^{\pm}$ as defined in (2.5). As mentioned above, this side limits are useful to obtain the evolution operator for a given initial condition. In particular, one can see that the diagonal Green's matrix elements do not depend on the x-position (we denote the diagonal elements $G_0(x,x;z)$ simply by $G_0(z)$) and have square root singularities at both band edges, i.e. Van Hove singularities characteristic of one-dimensional systems. From (2.53) we can calculate the density of states obtaining:

$$\rho(\omega) = -\frac{dk}{d\omega} = \frac{1}{\sqrt{4J^2-(\omega-\omega_c)^2}} = |G_0^{\pm}(\omega)| \tag{2.60}$$

for ω belonging to the spectrum. Since $|-\tilde{z}+\sqrt{\tilde{z}^2-1}|<1$ for $|\tilde{z}|>1$, from (2.57) we can see that the off-diagonal matrix elements $G_0(x,x';z)$ decay exponentially with the distance $|x-x'|$ when z does not coincide with the spectrum. This is no longer true when $-1 \le \tilde{z} \le 1$.
Now we can use the time-dependent Green's function to get the time-evolution amplitude for the generic site x_0 that we suppose to be excited at $t = 0$. From (2.31), substituting in this atomless array $|e\rangle$ with $|x_0\rangle$, irrespective of the position of the initially excited site, we have for $t > 0$:

$$u_0(t) = iG_0(t) = \frac{i}{2\pi}\int_{-\infty}^{+\infty} dz G_0^+(z)e^{-izt} = J_0(2Jt) = \left(\frac{2}{2\pi Jt}\right)^{1/2}\cos(2Jt - \pi/4) + O(t^{-3/2}) \quad (2.61)$$

where J_0 is the Bessel function of the first kind and zero order. The asymptotic form of $u(t)$ depends on the singularities of $G_0(z)$ on the real $z-$axis, i.e. on the branch cut and particularly its end points. For the one-dimensional infinite array, indeed, near these points we have $|G_0^{\pm}(z)| = \rho(z) \propto z^{-1/2}$ and, since $\int_0^{+\infty} z^{1/2}e^{-izt}dz \propto t^{-1/2}$, one obtains this asymptotic decay.

2.3.2 The CCA with a single defect

We consider here the case of the same infinite CCA whose perfect periodicity has been broken at just one site, i.e. the cavity at site $|x_d\rangle$ has a single-mode of frequency $\omega_d = \omega_c + \omega_1$, different from all the other (Fig (2.2b)). This is the analogue of the problem of a substitutional impurity in a perfect periodic lattice, well-known in solid state physics. The corresponding tight-binding Hamiltonian reads:

$$\hat{H} = \hat{H}_0 + \hat{H}_1 \qquad with \qquad \hat{H}_1 = \omega_1|x_d\rangle\langle x_d| \quad (2.62)$$

in which $\hat{H}_0$ is the Hamiltonian of the perfect CCA given in (2.50) and $\hat{H}_1$ is the defect term and the system is thus described by an Hamiltonian consisting of an unperturbed part and a perturbation term, as discussed at the beginning of the chapter. The Green's function corresponding to $\hat{H}$ can be evaluated exactly in terms of $\hat{G}_0(z)$ and ω_1. Using the expansion (2.12), after some manipulation, we obtain:

$$\hat{G}(z) = \hat{G}_0(z) + \frac{\omega_1}{1 - \omega_1 G_0(z)}\hat{G}_0(z)|x_d\rangle\langle x_d|\hat{G}_0(z) \quad (2.63)$$

in which $G_0(z)$ at the denominator is the diagonal matrix element of $\hat{G}_0(z)$ that does not depend on the position. As already seen, the poles of $\hat{G}(z)$ correspond to the discrete eigenvalues of $\hat{H}$ and, in the present case, the Green's function has only a pole given by $G_0(\omega_p) = 1/\omega_1$, i.e. at the frequency:

$$\omega_p = \omega_c \pm \sqrt{4J^2 + \omega_1^2} \qquad for \quad \omega_1 \gtrless 0 \quad (2.64)$$

Thus the Hamiltonian in (2.62) has one and only one discrete level of frequency ω_p for any nonvanishing value of ω_1. Note that the pole must lie outside the band of $\hat{H}_0$, because inside the band $G_0(z)$ has a nonzero imaginary part (cf. (2.58) with $x = x'$) and consequently $G_0(\omega_p) = 1/\omega_1$ cannot be satisfied. From (2.10) we can obtain the expression for the associated bound state [6] $|\psi_b\rangle$ by calculating the residue of $G(x, x'; z)$ at the pole $z = \omega_p$:

[6] It can be shown that ω_p is always non-degenerate [90].

$$Res\{G(x,x';\omega_p)\} = \lim_{z\to\omega_p}(z-\omega_p)G(x,x';z) = \langle x|\psi_b\rangle\langle\psi_b|x'\rangle \tag{2.65}$$

From (2.63) we calculate the residue, finally obtaining the following expression for $|\psi_b\rangle$:

$$|\psi_b\rangle = \sum_x b_x|x\rangle, \qquad with \quad b_x = \frac{G_0(x,x_d;\omega_p)}{\sqrt{-G_0'(\omega_p)}} \tag{2.66}$$

where, from (2.57), $G_0'(z) = \frac{dG_0(z)}{dz} < 0$ for z not belonging to the spectrum. Moreover, since for z outside the band the off-diagonal matrix elements $G_0(x,x';z)$ decay exponentially with the distance $|x-x'|$, it can be seen that $|\psi_b\rangle$ is a localized state in the vicinity of the impurity site $|x_d\rangle$. The amplitudes b_x in (2.66) can be put into the form:

$$b_x = Be^{-\frac{|x-x_d|}{\lambda}} \qquad with \quad \frac{1}{\lambda} = -\log\left[\sqrt{1+\frac{\omega_1^2}{4J^2}} - \frac{|\omega_1|}{2J}\right] \tag{2.67}$$

with normalization constant B and localization length λ, which is a measure of the linear extent of the bound eigenfunction. The state is the more localized the larger is $|\omega_1|$.
The Green's function in (2.63) has the same branch cut of $\hat{G}_0$, hence the spectrum of $\hat{H}$ coincides with that of $\hat{H}_0$. Using (2.17) it is possible to obtain the corresponding eigenstates in the *scattering* form:

$$|\psi_k^{\pm}\rangle = |\phi_k\rangle + \hat{G}^{\pm}\hat{H}_1|\phi_k\rangle \tag{2.68}$$

with the $\hat{H}_0$'s eigenstates $|\phi_k\rangle$ given in (2.52) for an $N-$sites cyclic array. We choose only the '+' solution that corresponds to the physical case where the incident photon is scattered from the defect, either reflected back or transmitted forward. Substituting the corresponding side limit of (2.63) into (2.68) we obtain the $x-$site amplitude for the unbound state $|\psi_k^+\rangle$:

$$\langle x|\psi_k^+\rangle = \langle x|\phi_k\rangle + \omega_1\langle x_d|\phi_k\rangle\frac{G_0^+(x,x_d;\omega_k)}{1-\omega_1 G_0^+(\omega_k)} \tag{2.69}$$

in which ω_k is the common spectrum of $\hat{H}$ and $\hat{H}_0$, given by the $N\to\infty$ limit of (2.53), and the generic matrix elements of $\hat{G}_0^+$ in the thermodynamic limit are given in (2.58). In particular, the amplitude of $|\psi_k^+\rangle$ at the defect site x_d reads:

$$\langle x_d|\psi_k^+\rangle = \frac{\langle x_d|\phi_k\rangle}{1-\omega_1 G_0^+(\omega_k)} \tag{2.70}$$

Moreover, from (2.69), the transmission coefficient for a plane wave propagating from the left and incident on the defect is found to be:

$$T_k = \frac{1}{|1 - \omega_1 G_0(\omega_k)|^2} = \left(1 + \frac{\omega_1^2}{4J^2 - \omega_k^2}\right)^{-1} \tag{2.71}$$

and does not exhibit any resonant structure.
If we now consider the defect site $|x_d\rangle$ initially excited ($t = 0$), the excitation decay amplitude is again obtained by calculating $iG(t)$ as for the uniform CCA. Now the contour integral has two contributions:

$$u(t) = iG(t) = \frac{i}{2\pi}\int_{cut} dz G^+(z)e^{-izt} + \frac{i}{2\pi}\int_{pole} dz G^+(z)e^{-izt} = u_c(t) + u_p(t) \tag{2.72}$$

This is a general expression valid for Hamiltonians with both discrete and continous eigenvalues. Here u_c is the probability amplitude contribution due to the branch cut of $G(z)$, which is calculated in the same way that in (2.61), while u_p is the contribution due to the pole. The former describes the fraction of the initial excitation propagating away from the defect towards the extremes of the CCA. It can be calculated as series of Bessel's functions [62]. The pole contribution is obtained by calculating the contour integral on a path that surrounds only the pole, hence from the theorem of residues we have:

$$u_p(t) = -2\pi i \frac{1}{2\pi} Res\{G^+(\omega_p)\}e^{-i\omega_p t} = |b_{x_d}|^2 e^{-i\omega_p t} \tag{2.73}$$

where (2.63) and (2.66) were taken into account. From (2.73) it can be seen that, in presence of a single pole, even as $t \to \infty$ there will be a finite probability $|b_{x_d}|^4$ of finding the excitation at site x_d that was initially excited. This is known as *fractional decay*. Moreover, we can see how a single bound state of the form (2.67) ensures the presence at long times of a finite probability amplitude in each site of the array. Indeed the pole-contribution $u_p(x, t)$ to the probability amplitude for the generic site x at time t, for the same initial condition, can be obtained by expressing the evolution operator as in (2.26) i.e. :

$$u_p(x, t) = \langle x|\psi_b\rangle\langle\psi_b|x_d\rangle e^{-i\omega_p t} = |B|^2 e^{-|x-x_d|/\lambda} e^{-i\omega_p t} \tag{2.74}$$

Hence the probability profile for $t \to \infty$ is due only to the pole contribution and reads:

$$P(x, t \to \infty) = |B|^4 e^{-2|x-x_d|/\lambda} \tag{2.75}$$

It is distributed with an exponential profile, centred on the defect site, through the entire array and the width of the profile is characterized by half the localization length of the bound state. The bound state profile is very peaked around the defect for large $|\omega_1|/J$ (cf. (2.67)), and so the probability profile at $t \to \infty$ (the constant B depends also on ω_1/J to normalize the bound state). The presence of a single defect, which mathematically corresponds to the presence of a

pole of $\hat{G}(z)$ outside the band, gives rise to a localized bound state of exponential $x-$profile that allows a fraction of the initial excitation to remain localized around the defect site: we refer to this as *photon localization*. The strenght of the defect $|\omega_1|/J$ determines the part of excitation which remains near x_d and the one which propagates away, as well as the localization profile.

2.3.3 A TLS coupled to the uniform CCA

In Fig (2.2c) is sketched the equivalent network of a TLS, whose transition frequency is ω_a, coupled to a cavity of the infinite uniform CCA. We consider the TLS inside the cavity at site x_0, coupled at rate g in dipole and RW approximation. For the moment we neglect any kind of loss. The general formalism for a TLS interacting with a structured reservoir presented in Sec. 2.2 can be applied also in this case. The general form for the x-representation Hamiltonian, with the same notation of (2.49), is:

$$\hat{H} = \omega_a \hat{\sigma}_+ \hat{\sigma}_- + \omega_c \sum_{x=-\infty}^{+\infty} \hat{a}_x^\dagger \hat{a}_x + J \sum_{x=-\infty}^{+\infty} \left(\hat{a}_x^\dagger \hat{a}_{x+1} + h.c. \right) + g \left(\hat{\sigma}_+ \hat{a}_{x_0} + h.c. \right) \tag{2.76}$$

Here the last term on the right side represents the coupling of the atom with the x_0th cavity, as described for the Jaynes-Cummings model in (1.2). In the single-excitation subspace with basis given by the orthonormal vectors $\{\{|x\rangle\}, |e\rangle\}$, where $|e\rangle$ represents the atomic excited state, the tight-binding Hamiltonian for this system reads:

$$\hat{H} = \omega_a |e\rangle\langle e| + \hat{H}_0 + \hat{H}_{ac} \qquad with \qquad \hat{H}_{ac} = g \left(|x_0\rangle\langle e| + |e\rangle\langle x_0| \right) \tag{2.77}$$

By using the diagonal form (2.51) of $\hat{H}_0$ in the thermodynamic limit, (2.77) can be put in the k-representation as follows:

$$\hat{H} = \omega_a |e\rangle\langle e| + \lim_{N\to\infty} \sum_k \omega_k^N |\phi_k^N\rangle\langle\phi_k^N| + \lim_{N\to\infty} \frac{g}{\sqrt{N}} \left(|\phi_k^N\rangle\langle e| + |e\rangle\langle\phi_k^N| \right) \tag{2.78}$$

The eigenstates $|\phi_k^N\rangle$ of $\hat{H}_0$ and the corresponding eigenvalues ω_k^N are given, respectively, in (2.52) and (2.53) for a finite $N-$sites array. The limiting procedure leads to a continuous eigenvalues band, as above mentioned. The form (2.78) is a particular case of the Fano-Anderson Hamiltonian. In the present problem the atom is coupled to a finite band of modes with a $k-$independent coupling strength. Also in this case, by separating the Hamiltonian (2.76) in the unperturbed term $\hat{H}_0' = \hat{H}_0 + \omega_a |e\rangle\langle e|$ and the coupling term $\hat{H}_{ac}$, it is possible to express the total Green's function in terms of $\hat{G}_0'$ and $\hat{H}_{ac}$. Here $\hat{G}_0'$, with the above notation, reads:

$$\hat{G}_0'(z) = \frac{|e\rangle\langle e|}{z - \omega_a} + \lim_{N\to\infty} \sum_k \frac{|\phi_k^N\rangle\langle\phi_k^N|}{z - \omega_k^N} \tag{2.79}$$

that is the uniform-CCA Green's function $\hat{G}_0$ with in addition the bare-atom term $|e\rangle\langle e|/(z-\omega_a)$. Again, using the expansion (2.12), we obtain the following expression:

$$\hat{G}(z) = \hat{G}'_0(z) + \hat{G}'_0(z)\left[f\,|e\rangle\langle x_0| + \text{h.c.} + f_1\,|e\rangle\langle e| + f_2\,|x_0\rangle\langle x_0|\,\right]\hat{G}'_0(z) \tag{2.80}$$

The detailed calculation to expand $\hat{G}$ and express it in this form is reported in Appendix A. The complex functions f, f_1, f_2 are given by:

$$f(z) = \frac{g}{1 - g^2 G_{0e}(z) G_{00}(z)}, \qquad f_1(z) = g G_{00}(z) f(z), \qquad f_2(z) = g G_{0e}(z) f(z). \tag{2.81}$$

with the following $\hat{G}'_0$'s matrix elements in the $N \to \infty$ limit:

$$G_{00} = \langle x_0|\hat{G}'_0(z)|x_0\rangle = \langle x_0|\hat{G}_0(z)|x_0\rangle = \frac{1}{2\pi}\int_{-\pi}^{\pi} dk \frac{1}{z - \omega_c - 2J\cos k}\,, \tag{2.82}$$

$$G_{0e} = \langle e|\hat{G}'_0(z)|e\rangle = \frac{1}{z - \omega_a} \tag{2.83}$$

$G_{00}(z)$ is the diagonal matrix element $G_0(x, x; z)$ for the uniform CCA given in (2.56), calculated in (2.57) and (2.58), here renamed for clarity. From the discussion on the uniform CCA and from (2.82), we know that $G_{00}(z)$ has a branch cut on the real $z-$axis for z which coincides with the spectrum of $\hat{H}_0$. The Green's function of the TLS + CCA in (2.80) thus present the same cut. As for the CCA with a single defect, the perturbation term of the total Hamiltonian leaves the spectrum unchanged compared to that of the uniform CCA and involves only the addition of discrete poles on the Green's function matrix elements. These poles are the discrete eigenenergies of $\hat{H}$. In order to find them, from (2.81), we need to find the roots of equation $1 - g^2 G_{0e}(z) G_{00}(z) = 0$ for the external domain $|z - \omega_c| > 2J$ in which $G_{00}(z)$ reads (cf. (2.57)):

$$G_{00}(z) = \frac{1}{\sqrt{(z - \omega_c)^2 - 4J^2}} \qquad for \quad |z - \omega_c| > 2J \tag{2.84}$$

Using (2.83), the above equation takes the form $(z-\omega_a)\sqrt{(z - \omega_c)^2 - 4J^2} = \pm g^2$. By introducing $z' = z - \omega_a$, we choose to calculate the poles with the $\omega_a = 0$ energy scale. In this case the equation to solve is $z'\sqrt{(z' + \delta_{ac})^2 - 4J^2} = \pm g^2$, i.e. the quartic equation:

$$z'^2\left[(z' + \delta_{ac})^2 - 4J^2\right] = g^4 \tag{2.85}$$

Here we have defined the atom-cavity detuning $\delta_{ac} = \omega_a - \omega_c$ as in Chap1. When $\delta_{ac} \neq 0$, solutions of (2.85) are algebraically extended and we report them in Appendix C. The quartic equation admits two real solutions $\omega_\pm$ and, for $\delta_{ac} = 0$, they read:

$$\omega_{0\pm} = \pm\sqrt{2J^2 + \sqrt{g^4 + 4J^4}} \qquad for \quad \delta_{ac} = 0 \tag{2.86}$$

We indicate the resonant solutions using the subscript '0'. As expected, for any finite g, $|\omega_{0\pm}| > 2J$, i.e. these fall out of the band (branch cut). In the strong-hopping limit $g \ll J$, $\omega_{0\pm} \simeq \pm 2J$ and the poles collapse into the band. In the strong-coupling[7] limit $g \gg J$, instead, they reduce to $\omega_{0\pm} \simeq \pm g$ since we retrieve a standard Jaynes-Cummings model where the atom significantly interacts only with the x_0th cavity.
Furthermore, with the help of (2.10), we obtain the matrix elements of the corresponding projectors by calculating the residues of $\hat{G}(z)$ at the poles. This calculation presents a relatively simple algebra only for the resonant case and we carry out it in Appendix B. For $\delta_{ac} = 0$ we find:

$$\langle x|\psi_0^{\pm}\rangle\langle\psi_0^{\pm}|x\rangle = \lim_{z\to\omega_{0\pm}} (z - \omega_{0\pm})G(x, x; z) \propto \varrho^{2|x-x_0|}, \quad |\varrho| < 1 \qquad for \quad \delta_{ac} = 0 \tag{2.87}$$

thus the residues of $\hat{G}(z)$ at the poles $\omega_{0\pm}$ decay exponentially with $|x - x_0|$ and, by imposing an ansatz compatible with this condition, we obtain:

$$|\psi_0^{\pm}\rangle = \mathcal{N}\sum_x (\pm\varrho)^{|x-x_0|}|x\rangle \pm c_{e0}\,|e\rangle \tag{2.88}$$

with

$$\mathcal{N} = \frac{\sqrt{(1 - c_{e0}^2)(1 - \varrho^2)}}{\varrho}, \tag{2.89}$$

$$\varrho = \frac{\omega_{0+} - \sqrt{{\omega_{0+}}^2 - 4J^2}}{2J}, \tag{2.90}$$

$$c_{e0}^2 = \frac{g^4}{2{\omega_{0+}}^2\left({\omega_{0+}}^2 - 2J^2\right)} = \frac{\eta^4}{2\left(\eta^4 + 2\sqrt{\eta^4 + 4} + 4\right)} \qquad for \quad \delta_{ac} = 0 \tag{2.91}$$

where the excitonic components of the states are $\pm c_{e0}$, with c_{e0} real positive and we have introduced the rescaled coupling constant:

$$\eta = \frac{g}{J} \tag{2.92}$$

As in the case of the CCA with a single defect, we have bound states [29, 32, 33] with an exponential probability profile. The probability to find the atom in $|e\rangle$ when the system is in

[7] This should not be confused with the *strong-coupling regime* of the atom-cavity Jaynes-Cummings model described in Chap1. Here we neglect any cavity leakage, thus we are implicitly assuming that the atom interacts with the x_0th cavity in strong-coupling regime.

either of the two bound states is c_{e0}^2 and is given in (2.91). In this resonant case we obtain a couple of states $|\psi_0^{\pm}\rangle$ with symmetrical eigenenergies with respect to the center of the band.
With an exponential ansatz as in (2.88) we obtain the bound states with a generic detuning and their generic expression as a function of $\omega_{\pm}$ reads:

$$|\psi^{\pm}\rangle = A_{\pm} \sum_x e^{-\frac{|x-x_0|}{\lambda_{\pm}}} |x\rangle + c_{e\pm}|e\rangle \tag{2.93}$$

with

$$\lambda_{\pm} = \log\left[\frac{g^2}{2J\omega_{\pm}}\left[1+\sqrt{\frac{4J^2\omega_{\pm}^2}{g^4}}\right]\right]^{-1}, \quad |A_{\pm}|^2 = \left(\frac{e^{2/\lambda_{\pm}}+1}{e^{2/\lambda_{\pm}}-1}+\frac{g^2}{\omega_{\pm}^2}\right)^{-1}, \quad c_{e\pm} = \frac{gA_{\pm}}{\omega_{\pm}} \tag{2.94}$$

The normalization constants $A_{\pm}$ are defined up to a phase factor. Again, the localization lengths $\lambda_{\pm}$ measure the linear extension of the two bound eigenfunctions. Here their two values are different for $\delta_{ac} \neq 0$ and converge, when $\delta_{ac} \to 0$, to the common localization length λ_0 associated with both states $|\psi_0^{\pm}\rangle$ of the resonant case. By substituting (2.86) into (2.94) we can cast $|\psi_0^{\pm}\rangle$ into the following form:

$$|\psi_0^{\pm}\rangle = |A_0| \sum_x (\pm 1)^{|x-x_0|} e^{-\frac{|x-x_0|}{\lambda_0}} |x\rangle \pm c_{e0}|e\rangle \quad with \quad \lambda_0 = \log\left[\frac{1}{2}\left(\sqrt{\sqrt{\eta^2+4}-2}+\sqrt{\sqrt{\eta^2+4}+2}\right)\right]^{-1} \tag{2.95}$$

in which the constant $|A_0|$ is the resonant limit of $|A_{\pm}|$. Here, again, the presence of bound states leads to photon localization. In this case the field remains localized around the atomic position. For the resonant case, the localization length of the probability profile is $\lambda_0/2$ and, from (2.95), it decreases with $\eta = g/J$. In the strong-coupling limit $\lambda_0 \to 0$, hence the field remain entirely localized on the x_0-site. Moreover, from (2.91), $c_{e0}^2 \to \frac{1}{2}$ as well as $\sum_x |\psi_0^{\pm}(x)|^2$. This means that, in the limit $\eta \gg 1$, both bound states describe a total excitation consisting of a field component, nonvanishing only on the x_0-site, and an excitonic component, both with probability $1/2$. This is in agreement with the asymptotic behaviour $\omega_0^{\pm} \to \pm g$, when the Jaynes-Cummings limit is reached. By introducing a nonvanishing detuning, the bound states show a localization profile with different lengths. For $\delta_{ac} > 0$, λ_- (λ_+) is larger than (smaller than) λ_0 calulated at the same η (and viceversa for $\delta_{ac} < 0$): the atom-cavity detuning introduce an imbalance between the two localization profiles. For $|\delta_{ac}| > g$ the most extended bound state (namely $|\psi^-\rangle$) tends to a quasi-photonic state, i.e $\sum_x |\psi^-(x)|^2 \to 1$, while the other one tends to a quasi-excitonic state, i.e. $|c_{e+}|^2 \to 1$. This is in agreement with the fact that an atom very far-detuned from the cavity-mode frequency does not exchange energy with the field.
Now we apply again (2.17) to calculate the unbound or *scattering* states. The scattering problem is similar to that of the CCA with a defect-mode and it will be discussed in Chap 3. In this case

the TLS acts as a scattering center for an incident photon and the reflection amplitude depends on both η and δ_{ac}/J. As in (2.68), the generic $k-$state is obtained by means of the Green's function and its analytic continuation (side limit):

$$|\psi_k^+\rangle = |\phi_k\rangle + \hat{G}^+(\omega_k)\hat{H}_{ac}|\phi_k\rangle \tag{2.96}$$

Here also we neglect the solution deriving from $\hat{G}^-$ since it has no physical meaning. The unperturbed $|\phi_k\rangle$s are eigenstates of $\hat{H}_0$ in the thermodynamic limit. Using (2.52), (2.77) and (2.80) the perturbation term reads:

$$\hat{G}^+(\omega_k)\hat{H}_{ac}|\phi_k\rangle = \frac{g}{\sqrt{N}}\left[\left(1+\frac{f_1(\omega_k^+)}{\omega_k^+}\right)\frac{|e\rangle}{\omega_k^+} + \frac{f(\omega_k^+)}{\sqrt{N}\omega_k^+}\sum_{k'}\frac{|\phi_{k'}\rangle}{\omega_k^+ - \omega_{k'}}\right] \tag{2.97}$$

where we set $\omega_k^+ = \omega_k + is$. Upon projection on $|x\rangle$ and on $|e\rangle$, for $N \gg 1$, we can express (2.96) as:

$$|\psi_k\rangle = \sum_k c_{kx}|x\rangle + c_{ke}|e\rangle, \qquad -\pi \leq k \leq \pi \tag{2.98}$$

with the x-components c_{kx} given by:

$$c_{kx} = \begin{cases} \frac{1}{\sqrt{N}}\left(e^{ik(x-x_0)} + r_k e^{-ik(x-x_0)}\right) & x - x_0 < 0, \\ \frac{1}{\sqrt{N}} s_k e^{ik(x-x_0)} & x - x_0 > 0. \end{cases} \tag{2.99}$$

and with transmission and reflection amplitudes s_k, r_k. The most simple way to obtain r_k, with the ansatz (2.99), is by imposing the boundary condition $c_{kx_0^+} = c_{kx_0^-}$ and by projecting the Schrödinger equation onto $\langle x_0|$. The reflection amplitude thus reads [17]:

$$r_k = \frac{\eta^2}{4i\sin k(\frac{\delta_{ac}}{2J} - \cos k) - \eta^2} \tag{2.100}$$

and the transmission amplitude is obtained by the constraints $s_k = r_k + 1$ and $|s_k|^2 + |r_k|^2 = 1$. By projecting (2.97) onto $|e\rangle$, we finally find the excitonic amplitude of $|\psi_k\rangle$, i.e. :

$$c_{ke} = \frac{\eta}{\sqrt{N}}\frac{1 + r_k}{\left(2\cos k - \frac{\delta_{ac}}{J}\right)} \tag{2.101}$$

In the next chapter we will use these results to analyze the atomic emission into the CCA-reservoir and the photon scattering problem. Here we consider only the emission in the strong-hopping limit ($\eta \to 0$) highlighting the role of the shift-width function or *self energy*. We don't need to take into account the discrete poles since, in this limit, they collapse into the band (this

is true for generic δ_{ac}). The general expression for the atomic probability amplitude is given by (2.72), where we have to consider only the branch-cut contribution, i.e:

$$u_c(t) = \frac{i}{2\pi}\int_{cut} dz G^+_{ee}(z)e^{-izt} = \lim_{s\to 0^+}\frac{i}{2\pi}\int_{cut} dz G_{ee}(z+is)e^{-izt} \tag{2.102}$$

In this way the contour integral is expressed in the same form of the general decay amplitude (2.31), valid for an atom interacting with a generic reservoir. Using (2.80) and (2.81), we obtain:

$$G_{ee}(z+is) = \langle e|\hat{G}(z+is)|e\rangle = \frac{1}{z+is-g^2G_{00}(z)} \tag{2.103}$$

By comparing this with the general case (2.32), recalling that now the energy scale is defined by $\omega_a = 0$, we find the self-energy function for a TLS interacting with an infinite CCA-reservoir:

$$W(z) = \sum_k \frac{|g_k|^2}{z-\omega_k} = g^2G^+_{00}(z) = -\frac{ig^2}{\sqrt{4J^2-(z+\delta_{ac})^2}} \tag{2.104}$$

Here the $k-$mode dispersion is given by the constant g^2/N, as result from (2.78), and the last term is the $N >> 1$ limit of the sum, obtained by using the result for $G_{00}(z) = \langle x_0|\hat{G}_0|x_0\rangle$ given in (2.58) and changing the scale. Now we can see why it is possible to apply the pole approximation for $W(z)$, as in the case of the free-space TLS. First we note that $W(z)$ is purely imaginary for $|z+\delta_{ac}| < 2J$. In the strong-hopping limit $|W(0)| \ll \delta_{ac}$ and the main contribution to the contour integral comes from the region $z \approx 0$, so we can approximate
$W(z) \approx W(0)$ in (2.102) for not too strong detuning ($\delta_{ac} < 2J$). The explicit form of the contour integral (2.102) in the pole approximation thus reads:

$$u_c(t) = \lim_{s\to 0^+}\frac{i}{2\pi}\int_{cut}\frac{e^{-iz}}{z+is+i|W(0)|}dz \tag{2.105}$$

This is the same that (2.40), i.e. the probability amplitude for the free-atom decay, but with a different rate, given by the imaginary part of the pole. In this case $W(0)$ is purely imaginary and, from (2.105), we obtain:

$$p_e(t) = |u_c(t)|^2 = e^{-\Gamma t}, \qquad with \quad \Gamma = 2|W(0)| = \frac{2g^2}{\sqrt{4J^2-\delta^2_{ac}}} \tag{2.106}$$

In the limit $g/J \to 0$, a TLS decaying into the CCA-reservoir shows a Markovian probability amplitude, as in the free space. The decay-rate is g^2/J for the resonant case. For small detuning, $W(z)$ is a slowly varying function of z and its small absolute value makes it possible the perturbative substitution $W(z) \approx W(0)$ into the contour integral. Here we have neglected the bound-states contribution to the atomic evolution. We will see in the next chapter that when the

discrete eigenvalues collapse into the band, i.e. in the strong-hopping limit, contributions like (2.74) become negligible with respect to the contour integral (2.102).

Chapter 3

Photon localization and population trapping in Coupled Cavity Arrays

Cavity quantum electrodynamics (CQED) studies the properties of atoms coupled to discrete photon modes in high-Q cavities. Such systems, which we reviewed in the first chapter, are of great interest in the study of the fundamental quantum mechanics of open systems, the engineering of quantum states, measurement-induced decoherence and have also been proposed as possible candidates for use in quantum information processing and transmission [81, 103].
More recently, several authors have considered the possibility of coupling each other many of such cavities, part or all of them contain a TLS (or a multiple-level atom-like system). Such Coupled Cavity Arrays (CCA), known also as Coupled Resonator Optical Waveguides (CROW), and several variants turned out to be a promising tool of investigation in many branches of modern physics. With the currently available photonic-crystal technology, it is possible to realize such an atomless arrays with a large number of components [140], the main experimental problem being the atom-CCA coupling. Very large arrays including one or more atoms have been so far only theoretically proposed. The first proposal of such an systems, dating back to 2006, is due to M. J. Hartmann, F. G. S. L. Brandão, and M. B. Plenio and concerns the study of strongly correlated many-body phenomena [1]. Shortly after, the use of atom-light interaction in coupled microcavity arrays has taken several directions: spin models [2], phase diagrams and phase transitions [4], dynamical effects [6, 12] and quantum information applications [5]. An interesting and rich dynamics characterises the propagation of initially localized excitations along the array [7, 8, 16]. In this respect, the simplest - yet very interesting - scenario is the propagation of excitation in single-atom arrays, where only one cavity of the CCA is coupled to a single two-level atom. Most of the attention in such setup has been focused on single- or multi-photon scattering [17, 18, 19, 23, 24, 25], where one or more photons impinge on the initially unexcited atom. Here we want to focus on the interplay between photon localizzation and atomic population trapping resulting from the emission of an initially excited TLS. We have

introduced in the previous chapter the mathematical tools necessary to analyze this physics, i.e. the essential ingredients to solve problems of scattering, atomic emission, population trapping and localization applied to the TLS-CCA interaction.
In Sec 3.1 we present the theoretical description for the coupling of several cavities in an array. In Sec. 3.2 we analyze our results about the emission of a TLS coupled with the central cavity of the array and we focus in particular on the interplay between the atomic trapped excitation and the corresponding fraction converted in cavity field that, at long times, localizes into the cavities near the atomic site. The dynamics is investigated in different regimes of the atom-cavity coupling strength, both at resonance and detuned coupling. Finally, in Sec. 3.3, we present a brief review of the scattering problem for a single photon propagating in the same system.

3.1 How to couple two or more cavities

The physical process underlying the coupling of two adjacent QED cavities is the evanescent-field coupling between the respective high-Q modes. Photon hopping can occur between neighbouring cavities due to the overlap of the spatial profile of cavity modes, as sketched in Fig (3.1a). The best candidates for such a realization are the 2D photonic crystals, which we reviewed in Sec 1.2. With these realizations, in which the single resonators consist of defect cavities embedded in a two-dimensional periodic structure whose resonant frequency falls within the forbidden gap of the surrounding 2D structure, it is relatively simple to obtain an uniform string of high-Q cavities whose adjacent field-modes can be coupled (Fig (3.1b)) [140]. In order to obtain a tight-binding Hamiltonian of the form (2.49) or (2.50), the mode-profile of the single resonator should not be significantly altered when it approaches another one, thus we assume sufficiently large separation between the individual resonators which are weakly coupled. This coupling is exactly the optical analog of the tight-binding limit in condensed-matter physics, in which the overlap of atomic wave functions is large enough that corrections to the picture of isolated atoms are required yet at the same time is not large enough to render the atomic description completely irrelevant.
In order to model such a process, we describe the array of cavities, arranged along the $x-$direction, by a periodic dielectric constant $\epsilon(\mathbf{r}) = \epsilon(\mathbf{r} + na\mathbf{u}_x)$, where $\mathbf{r}$ is the position inside a generic cavity of the one-dimensional array, a the distance between the centers of two adjacent cavities and n an integer [14]. In the Coulomb gauge we have $\nabla \cdot (\epsilon(\mathbf{r})\mathbf{A}) = 0$ and the vector potential can be expanded as linear combination of single-cavity contributions whose frequency is ω_c:

$$\mathbf{A}_k(\mathbf{r}, t) = e^{i\omega_k t} \sum_n e^{-inka} \mathbf{A}_0(\mathbf{r} - na\mathbf{u}_x) \tag{3.1}$$

The localized modes described by the vector potential $\mathbf{A}_0(\mathbf{r})$ are the analogue of the Wannier functions, by means of which the field operator is expanded in the well-known Bose-Hubbard model of condensed matter physics. Since the vector potential in (3.1) satisfies the Bloch the-

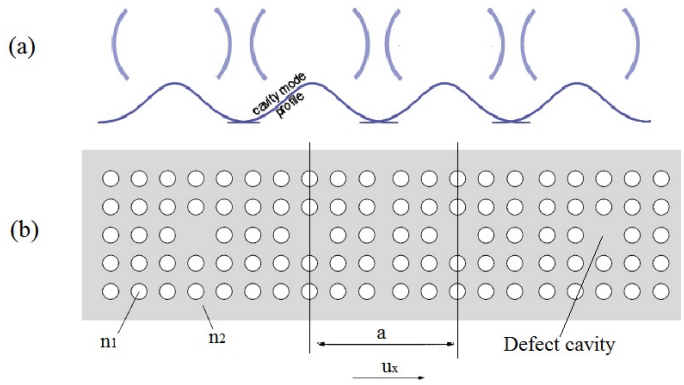

Figure 3.1: (a) An array of single-mode cavities. Photon hopping can occur between two nearest-neighbour cavities owing to the spatial overlap of the corresponding modes profile. (b) Corresponding photonic-crystal realization, obtained by coupling the 2D individual defect cavities (from [14]). The distance between the centers of the cavities is a and $\mathbf{u}_x$ indicates the direction versor of the array. The medium is described by two different refraction indexes, n_1 and n_2.

orem, we can limit ourselves only to the eigenfrequencies belonging to the first Brillouin zone: $-\frac{\pi}{a} \leq \omega_k \leq \frac{\pi}{a}$. Applying the Maxwell's equations to $A_0(\mathbf{r})$, localized around a generic $n-$site, we find:

$$\nabla \times (\nabla \times \mathbf{A}_0(\mathbf{r})) = \epsilon_0(\mathbf{r}) \frac{\omega_c^2}{c^2} \mathbf{A}_0(\mathbf{r}) \tag{3.2}$$

In which $\epsilon_0(\mathbf{r})$ denotes the single-cavity dielectric constant. From (3.1) it can be seen that the above equation can be applied to the generic $k-$mode of the expanded vector potential, i.e.:

$$\nabla \times (\nabla \times \mathbf{A}_k(\mathbf{r})) = \epsilon(\mathbf{r}) \frac{\omega_k^2}{c^2} \mathbf{A}_k(\mathbf{r}) \tag{3.3}$$

Here we have replaced $\epsilon_0(\mathbf{r})$ with the periodic dielectric constant $\epsilon(\mathbf{r})$ and ω_c with the eigenvalue ω_k. We consider the single-cavity vector potential $\mathbf{A}_0$ normalized in such a way that $\int_V d\mathbf{r}|\mathbf{A}_0(\mathbf{r})|^2=1$, where the integration is over the cavity volume V. In order to find the dispersion relation, we substitute (3.1) into (3.3) and multiply both sides from the left by $\mathbf{A}_0^*(\mathbf{r})$. After integrating over the position, we find:

$$\omega_k^2 = \omega_c^2 \frac{1 + \sum_{n\neq 0} e^{-inka} \beta_n}{1 + \Delta + \sum_{n\neq 0} e^{-inka} \alpha_n} \tag{3.4}$$

where α_n,β_n and Δ are defined as:

$$\alpha_n = \int d\mathbf{r}\, \epsilon(\mathbf{r})\, \mathbf{A}_0^*(\mathbf{r}) \cdot \mathbf{A}_0(\mathbf{r} - na\, \mathbf{u}_x) \tag{3.5a}$$

$$\beta_n = \int d\mathbf{r}\, \epsilon_0(\mathbf{r} - na\, \mathbf{u}_x)\, \mathbf{A}_0^*(\mathbf{r}) \cdot \mathbf{A}_0(\mathbf{r} - na\, \mathbf{u}_x) \tag{3.5b}$$

$$\Delta = \int d\mathbf{r}\, \left[\epsilon(\mathbf{r}) - \epsilon_0(\mathbf{r})\right]\, |\mathbf{A}_0(\mathbf{r})|^2 \tag{3.5c}$$

When the separation a between the cavities is sufficiently large or the coupling is sufficiently weak, the only modes with overlapping profiles are the nearest-neighbor. In this case we have to keep only the $\alpha_{\pm 1}, \beta_{\pm 1}$ and Δ integrals in (3.5). Of course, from symmetry considerations, we also require that $\alpha_1 = \alpha_{-1}$ and $\beta_1 = \beta_{-1}$ and assume all integrals to be sufficiently small. In this way, substituting these integrals in (3.4), the dispersion relation is simplified as follows:

$$\omega_k = \omega_c \left[1 - \frac{\Delta}{2} + (\beta_1 - \alpha_1)\cos(ka)\right] \tag{3.6}$$

The band of frequencies is centered around $\omega_c' = \omega_c\,(1 - \Delta/2)$. If the periodic dielectric constant ϵ coincides with ϵ_0 at each site, from (3.5c) it results $\Delta = 0$ and $\omega_c' = \omega_c$. This is strictly true only for isolated cavities, but we will assume below a weak enough cavity-coupling to approximate $\Delta \approx 0$. Thus the hopping rate J we introduced in Sec 2.3 is found to be:

$$\frac{J}{\omega_c} = \frac{1}{2}\,(\beta_1 - \alpha_1) = \frac{1}{2}\int d\mathbf{r}\, \left[\epsilon_0(\mathbf{r} - a\, \mathbf{u}_x) - \epsilon(\mathbf{r} - a\, \mathbf{u}_x)\right]\, \mathbf{A}_0^*(\mathbf{r})\mathbf{A}_0(\mathbf{r} - a\, \mathbf{u}_x) \tag{3.7}$$

and the dispersion relation takes the form $\omega_k = \omega_c + 2J\cos k$ discussed in Sec 2.3. The group velocity of the CCA is:

$$v_g(k) = \frac{d\omega_k}{dk} = -Ja\sin(ka) \tag{3.8}$$

and it is maximum for $k = \pm\frac{\pi}{2a}$, i.e. at $\omega = \omega_c$.
The Hamiltonian in second quantization form (2.49) is obtained by introducing the creation and annihilation operators of the localized field-modes or Wannier functions, $\hat{a}_n^\dagger$ and $\hat{a}_n$ with $x = na$. Hence, considering only nearest-neighbor coupling with the uniform hopping rate in (3.7), the CCA Hamiltonian assuming identical cavities reads:

$$\hat{H} = \omega_c \sum_n \hat{a}_n^\dagger \hat{a}_n + J \sum_n \left(\hat{a}_n^\dagger \hat{a}_{n+1} + \hat{a}_{n+1}^\dagger \hat{a}_n\right) \tag{3.9}$$

where $\hat{a}_n^\dagger$ ($\hat{a}_n$) creates (annihilates) a single-photon of frequency ω_c inside the $n-$th cavity. In deriving (3.9) we have neglected the counterrotating terms which contain products of two creation

or two annihilation operators. This is resonable because the overlap integrals (3.5) are generally small, i.e. $J/\omega_c \ll 1$. Since the total excitation-number operator $\hat{N} = \sum_n \hat{a}_n^\dagger \hat{a}_n$ commutates with $\hat{H}$, the total photon-number is conserved.
The tight-binding Hamiltonian (3.9) is a particular case of the Bose-Hubbard model, which was first discussed by Fisher et al in [69] as the bosonic counterpart of the Hubbard model. The B-H Hamiltonian, indeed, contains also an interaction term of the form $U \sum_n \hat{a}_n^\dagger \hat{a}_n \left(\hat{a}_n^\dagger \hat{a}_n - 1\right)$ that describes the interactions between bosons at each site, with strengh U. For non-vanishing U, there are two different phases at zero temperature that are separated by a quantum phase transition when the ratio U/J crosses a critical value. The uniform tight-binding Hamiltonian (3.9) is the $J >> U$ limit of the B-H model, in which the tunnelling term dominates and the lowest-energy state of the system is a condensate of delocalised bosons, i.e. the system is in a superfluid phase. Above a specific value of U/J, the system ceases to be a superfluid and becomes a Mott insulator, with a well-defined number of localised particles in each site. In this case it will thus be energetically favourable for the bosons to evenly distribute across all lattice sites and avoid moving around in order to minimise the repulsion. The superfluid to Mott insulator phase transition is of a quantum character and is driven by quantum fluctuations, as it occurs even at zero temperature. Photons are noninteracting bosons, and there is no possibility to have any quantum phase transitions in purely photonic systems. For a pure Bose system as that described by (3.9), the conducting phase at zero temperature is always superfluid. However, engineered arrays of optical cavities, few-level atoms, and laser light can form a strongly interacting many-body system which can simulate condensed matter physics models [1, 2, 3, 4]. For such a simulation of a Bose-Hubbard model a self-interaction term is needed. Indeed, the Bose-Hubbard self-interaction term has the form of a Kerr self-nonlinearity $(\hat{a}_n^\dagger)^2(\hat{a}_n)^2$ and its effect is generally negligible at the level of individual quanta. By placing several TLS or multi-level atoms inside each cavity and using external lasers, it is possible to generate strong nonlinear interaction among the photons of the cavity mode. Indeed, strong interactions of the light mode with atoms inside the cavity, under particular circumstances, mediate strong nonlinear interaction among the photons. The strength of the nonlinearity can be increased even further if instead of considering photons as the bosonic particles of the model, one considers polaritons, joint photonic-atomic excitations.

3.2 The TLS emission: photon localization vs population trapping

We now describe the emission of a TLS into an environment consisting of a CCA initially in the vacuum state [15]. We consider the atom embedded into a cavity of the uniform array. A sketch of the entire setting and its equivalent network is shown in Fig (3.2). The mathematical description of the joint atom-CCA system is reviewed in Sec 2.3.3. In the following we will label with '0' the position of the cavity containing the atom. The CCA can be realized by

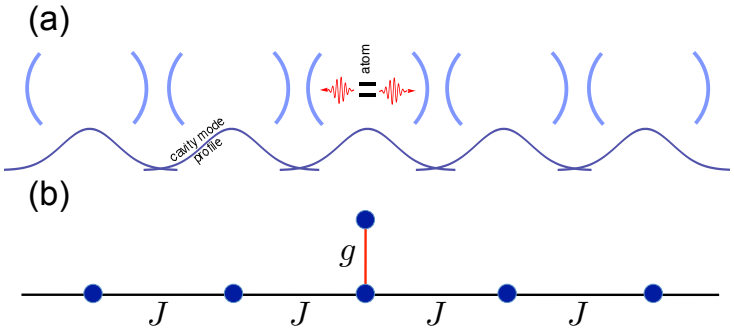

Figure 3.2: (a) Sketch of the setup. A large array of single-mode cavities, where one cavity is coupled to an initially excited two-level atom. Photon hopping can occur between two nearest-neighbour cavities. (b) Equivalent network.

using either coupled superconducting transmission line resonators [139] or defect resonators in photonic crystals [140], whose main features have been described in Sec. 1.2. Such systems are of importance in the study of the fundamental properties of open quantum systems, as well as for quantum information processing applications.

We will focus on the strong-coupling regime and on the polariton formation when a single qubit is coupled to a mesoscopic photonic system. From the perspective of the qubit, the CCA is a mesoscopic system representing a dissipative electromagnetic environment featuring a spectral density that is highly structured. In the absence of additional qubit decay channels, polaritonic bound-states typically are formed in such a system. In the previous chapter we have discussed their mathematical expressions by using the Green's function method.

The single-atom CCA - under rotating-wave approximation and in the thermodynamic limit of an infinite number of cavities - is described by the Hamiltonian (2.76) and it is a known instance of the general Fano-Anderson [20, 21] (or Friedrichs-Lee) model, where a two-level system is coupled to a finite band of bath modes with a constant coupling strength. When the TLS frequency lies at the middle of the band, the resulting dressed system features a continuous band (which coincides with the bare bath band) and two symmetrical out-of-band discrete levels. The polaritonic bound states are associated to the latter ones and they are given in (2.95), while (2.98) is the expression for the unbound stationary states associated with the band. We have seen that each bound state is localized around the atom's position on the lattice, the localization length being a decreasing function of the coupling strength. Owing to the presence of the atom-photon bound states, the atom is in general unable to eventually release the entire amount of its initial excitation to the field and thus exhibits fractional decay. By discussing the expressions for the discrete eigenvalues at resonance given in (2.86), we mentioned the Jaynes-Cummings limit $g \gg J$, in which their asymptotic values $\approx \pm g$ witness a dynamics involving energy-exchange only between the atom and the cavity containing it. This is the extreme-case of population trapping for this system, in which the time-averaged atomic population at long times is $1/2$ and the atom periodically exchanges the entire content of its initial energy with the 0th cavity field so as to exhibit standard vacuum Rabi oscillations. In this case only bound states

take place to the atom-field dynamics. On the other hand, the unbound or scattering states are responsible for the fractional-propagation of the field, i.e. part of the initial atomic excitation is converted in light departing away from the emitter. In the strong-hopping limit $g \ll J$, for which the discrete eigenvalues collapse into the band, the atom-field dynamics is almost entirely governed by the unbound states. In this case standard exponential decay of atomic population takes place, the atom showing an (almost) Markovian[1] behaviour as in the free-space decaying or in weak-coupling regime of a single cavity QED, while the photon wave function spreads in either direction of the array in such a way that, for long enough times, it vanishes within any finite region around the central cavity. At intermediate values of the coupling rate, in general, the dynamics features partial field localization and atomic fractional decay, the latter being due to population trapping that manifests as a residual oscillation of the atom's excitation at large times. Whenever partial population trapping takes place then, clearly, photon localization must occur, with part of the field propagating away and the remaining is confined (symmetrically) around the cavities next to the atom. In this case the (trapped) atomic population oscillates with a time-averaged value less than $1/2$ and the energy swapping involves several cavities (the whole array, in principle) symmetrically arranged around the atom, the field in each cavity oscillating with amplitude exponentially decreasing with the distance from the atom. As we will see below, this exponential localized field-profile has the same localization length as that of the bound states, being closely linked to these. We want to examine in details the balance, at long times, between the atomic trapped excitation and the corresponding field-localized part for differtent coupling regimes. Initially we consider the resonant-atom case, introducing the detuned case later. In presence of atom-cavity detuning the localized profile and population trapping change quantitatively but not qualitatively, the balance resulting strongly altered only for very large detuning. In general, we will see how field localization and atomic population trapping do not arise simultaneously as the coupling rate grows from zero and we will highlight the existence of a regime of intermediate coupling strengths such that significant field localization can occur with no appreciable population trapping. In such cases, thereby, field localization is not accompanied by appreciable fractional atomic decay. At long enough times, in this regime the localized fraction of the photon wave function undergoes time modulation in intensity. Unlike in the strong-coupling limit, such modulation is not connected with atomic excitation/emission processes (the atom having fully decayed to the ground state). Rather, it reflects a mere time-continuous redistribution of light among the cavities next to the atom.

3.2.1 Resonant atom-cavity coupling

From the previous chapter we have all the ingredients to investigate the atomic emission into the field vacuum by an initially excited atom i.e., to study the time evolution of the state $|\Phi(0)\rangle = |e\rangle$. Since the atomic and cavity frequencies coincide, in this case the dynamics is independent of

[1] In Sec 4.2, by introducing an exact definition of open quantum Markovian processes, we will see that, strictly speaking, a Markovian dynamic for the TLS-CCA interaction can't occur for any finite g/J.

their common value ω_c, which here we set to zero. A straightforward decomposition of $|\Phi\rangle$ in terms of all bound and unbound stationary states as given by Eqs. (2.88) and (2.98), respectively, leads to the following joint-state at time $t \geq 0$:

$$|\Phi(t)\rangle = \sum_k c^*_{ke} e^{-i\omega_k t}|\psi_k\rangle + \sum_{\mu=\pm} c_{e0}\, e^{-i\omega_{0\mu} t}|\psi^\mu_0\rangle\,. \tag{3.10}$$

with continuous-spectrum frequencies $\omega_k = 2J\cos k$ associated to the branch cut of the Green's function (2.80) and discrete eigenvalues, corresponding to the poles, given in (2.86). It is convenient to express the atom's excitation probability amplitude $\alpha(t)$ as the sum of two contributions:

$$\alpha(t) = \langle e|\Phi(t)\rangle = \alpha_u(t) + \alpha_b(t)\,, \tag{3.11}$$

where $\alpha_u(t)$ and $\alpha_b(t)$ are the contribution due to the unbound and bound states respectively, i.e:

$$\alpha_u(t) = \langle e|\sum_k c^*_{ke}\, e^{-i\omega_k t}|\psi_k\rangle = \sum_k |c_{ke}|^2 e^{-i\omega_k t}\,, \tag{3.12}$$

$$\alpha_b(t) = \langle e|\sum_{\mu=\pm} c_{e0}\, e^{-i\omega_{0\mu} t}|\psi^\mu_0\rangle = 2c^2_{e0}\cos(\omega_{0+}t)\,, \tag{3.13}$$

where we used $\omega_{0-} = -\omega_{0+}$ [cf. (2.86)] and c_{ke}, c_{e0} given respectively in ((2.101) with $\delta_{ac} = 0$) and (2.91).

For the corresponding field-evolution we use the notation of the previous chapter, i.e. the discrete array-position index is x (the nearest-neighbor cavities distance a is set to unity), with $x_0 = 0$. The photon excitation amplitude at the xth cavity is obtained by projecting (3.10) onto $|x\rangle$:

$$\psi(x,t) = \langle x|\Phi(t)\rangle = \psi_u(x,t) + \psi_b(x,t) \tag{3.14}$$

with

$$\psi_u(x,t) = \sum_k c_{kx} c^*_{ke} e^{-i\omega_k t}\,, \tag{3.15}$$

$$\psi_b(x,t) = c_{e0}\mathcal{N}\sum_{\mu=\pm}\mu(\mu\,\varrho)^{|x|}e^{-i\omega_{0\mu}t} = 2c_{e0}\mathcal{N}\varrho^{|x|}\begin{cases} -i\sin\omega_{0+}t & \text{for } |x| \text{ even} \\ \cos\omega_{0+}t & \text{for } |x| \text{ odd} \end{cases} \tag{3.16}$$

In analogy with the atomic amplitude, here $\psi_u(x,t)$ [$\psi_b(x,t)$] stands for the contribution from the unbound (bound) stationary states to the photon probability amplitude $\psi(x,t)$ and c_{kx}, $\mathcal{N}$, ϱ are given respectively in (2.99), (2.89), (2.90). Below we evaluate separately the atomic and field's contributions to the state evolution.

3.2.1.1 Atom's excitation amplitude

When the coupling strength is very small [cf. Fig. (3.3a)] standard spontaneous emission takes place and the atomic excitation exhibits a purely exponential decay. In such conditions, indeed, the emitter does not sense the finiteness of the field band (correspondingly, the effective spectral density is flat). We have already analyzed this strong-hopping case at the end of Sec. 2.3.3, by evaluating the unbound contribution to the amplitude with a contour-integral of the Green's function matrix element $G_{ee}(z)$ in pole approximation, i.e. by replacing the self-energy function with a constant. In this limit we have neglected the bound-states contributions to the amplitude, justifying this with the collapse of the discrete external poles into the band. Now we want to prove this more rigorously. Using (2.91), we can see that $\alpha_b \to \frac{\eta^4}{4}\cos(\omega_{0+}t)$ for η small enough, while $\alpha_u(t)$ does not vanish in the limit $\eta \to 0$ at any finite t. Indeed, for $\eta = 0$, it results $\alpha_b = 0$ and therefore $\alpha_u = 1$ since the decoupled atom never decays. Thus, when $\eta \ll 1$, the only relevant contribution to the atomic excitation amplitude is the unbound one, i.e. $\alpha(t) \approx \alpha_u(t)$. With the help of (2.101), substituting $\frac{1}{N}\sum_k \to \frac{1}{2\pi}\int dk$ for $N \gg 1$, $\alpha_u(t)$ can be expressed in the integral form as:

$$\alpha_u(t) = \frac{\eta^2}{2\pi}\int_{-\pi}^{\pi} dk\, \frac{\sin^2 k}{\sin^2(2k) + \frac{\eta^4}{4}}\, e^{-i\omega_k t} \tag{3.17}$$

which is a (real) time function that vanishes in the limit $t \to \infty$. This can be seen by noting first that in (3.17) we can replace $e^{-i\omega_k t} \to \cos(\omega_k t)$ since the contribution from the imaginary part vanishes (this yields an odd integrand function). This and the Jacobi-Anger expansion [34]:

$$\cos(z\cos k) = J_0(z) + 2\sum_{n=1}^{\infty}(-1)^n J_{2n}(z)\cos(2nk) \tag{3.18}$$

allow us to express $\alpha_u(t)$ as a series of Bessel functions:

$$\alpha_u(t) = a_0\, J_0(2Jt) + \sum_{n=1}^{\infty} a_n\, J_{2n}(2Jt) \tag{3.19}$$

with $a_0 = I_0$, $a_{n\geq 1} = 2(-1)^n I_n$ and where I_n is obtained from integral (3.17) by replacing the complex exponential with $\cos(2nk)$. In Figs. (3.3) and (3.5), we study the behavior of the atomic excitation $p_e(t) = |\alpha(t)|^2$ and the photon probability distribution $p_x(t) = |\psi(x,t)|^2$, respectively, for different values of the rescaled coupling strength $\eta = \frac{g}{J}$. The plots were drawn through numerical evaluation of (3.12) and (3.15). Due to the appearance of the Bessel functions, the amplitude $\alpha_u(t)$ eventually decays to zero after exhibiting secondary oscillations [cf. Fig. (3.3b)], these becoming less and less significant as $\eta \to 0$. This can be proved by expressing (3.17) as:

$$\alpha_u(t) = \frac{\eta^2}{\pi}\int_0^{\pi} dk\, F(k)\, e^{-2iJt\cos k} \qquad with \quad F(k) = \frac{\sin^2 k}{\sin^2(2k) + \frac{\eta^4}{4}} \tag{3.20}$$

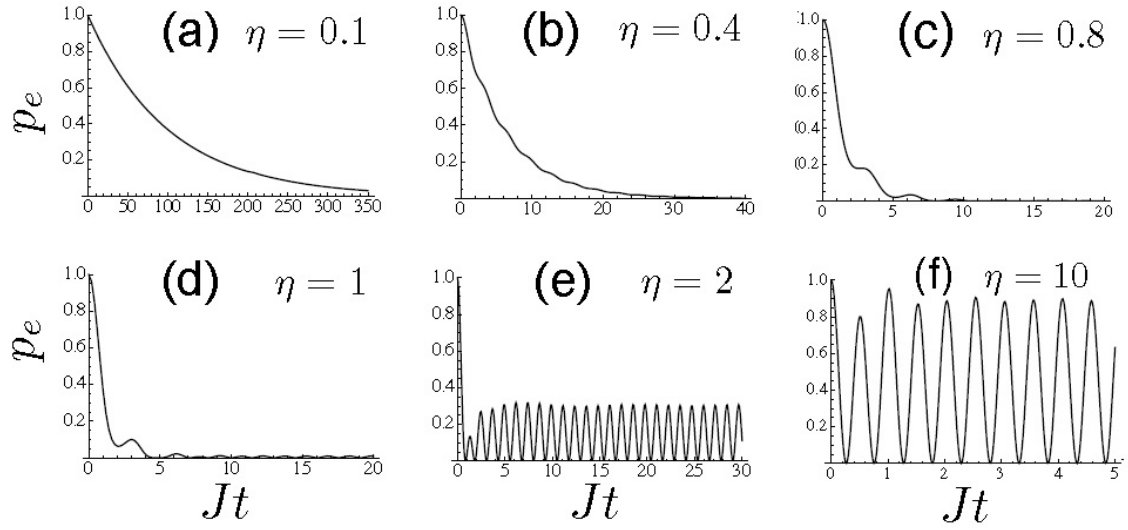

Figure 3.3: Atom's excitation probability $p_e = |\alpha|^2$ against time (in units J^{-1}) for increasing values of the rescaled coupling strength $\eta = g/J$.

where we have used that both $F(k)$ and the complex exponential are even functions of k. Function $F(k)$ is peaked around $k = \pm\pi/2$, the height of the peaks becoming infinite in the limit $\eta \to 0$. Hence, in the strong-hopping limit, the dominant contribution to the integral (3.20) comes from values of k close to $k = \pi/2$, the only unbound states with appreciable excitonic component being the quasi-resonant ones. One can therefore make the approximations $\sin k \simeq 1$, $\cos k \simeq \pi/2 - k$, which yields $F(k) \simeq 1/[4(k-\pi/2)^2 + \eta^4/4]$, and, moreover, extend the integration range to $[-\infty, \infty]$. This entails:

$$\alpha_u(t) \simeq \frac{\eta^2}{\pi}\int_{-\infty}^{\infty} dk\, \frac{e^{2iJ(k-\pi/2)t}}{4(k-\pi/2)^2+\eta^4/4} \equiv \frac{\eta^2}{\pi}\int_{-\infty}^{\infty} dk\, \frac{e^{2iJtk}}{4k^2+\eta^4/4} = e^{-\frac{\eta^2}{2}Jt} \tag{3.21}$$

where we made use of the Fourier-transform of a Lorentzian, which results in an exponential function. The decay rate of $p_e(t) = |\alpha_u(t)|^2$ is g^2/J, in agreement with (2.106), obtained by the Green's function in pole-approximation. In the first chapter we have also found an exponential decay for an atom in free-space and in the weak-coupling regime of a damped cavity QED. The Markovian behaviour of $p_e(t)$ is a general feature of the dynamics of a two-level atom which is coupled to a 'memoryless' reservoir of field modes initially in the vacuum state. For a generic structured bath of modes and for a generic initial condition, the atomic excitation probability can be expressed as $p_e(t) = p_e(0)|\Gamma(t)|^2$ where the function $\Gamma(t)$ is defined as the solution of the integrodifferential equation [42]:

$$\frac{d}{dt}\Gamma(t) = -\int_0^t dt'\zeta(t-t')\Gamma(t') \tag{3.22}$$

corresponding to the initial condition $\Gamma(0) = 1$, where ζ denotes the two-point reservoir correlation function, obtained by Fourier-transforming the spectral density $\rho(\omega)|g(\omega)|^2$. If the spectral density varies very slowly with ω, the corresponding correlation function $\zeta(\tau)$ turns out to be narrow enough and $\Gamma(t)$ is expected not to present pronounced secondary oscillations. On the other hand, if the spectral density is a very peaked function, as in the case of an high-Q cavity QED with Lorentzian density of states given in (2.42), the bath is caracterized by a $\zeta-$function slowly decaying in time (esponential decreasing for the CQED with Lorentzian d.o.s.). Indicating with t^* this characteristic (long) decay-time, it is as if the bath had memory of the atomic state at t up to time $t + t^*$. This results in pronounced revivals in the atomic probability evolution, as a back-flow of information[2] from the environment in which the atom decays (cf. Fig (1.4) for the CQED example). In our case $p_e(0) = 1$ and $\Gamma(t) = \alpha_u(t)$ for $\eta \ll 1$. The spectral density is $g^2\left(4J^2 - \omega^2\right)^{-1/2}$ and, in this particular case, it is proportional to the self-energy function [cf. (2.104) with $\delta_{ac} = 0$]. The pole approximation for the $G_{ee}(z)$ Green's function matrix element, by means of which the contour integral can be approximated as (2.105) resulting in the exponential law (2.106), is equivalent to consider completely flat the spectral density. By Fourier-transforming it we obtain $\zeta(\tau) \propto \delta(\tau)$ and by substituting in (3.22), the solution for $|\Gamma(t)|^2$ is found to be the same exponential decay law, with the same rate. This is analogous to the free-space atomic emission analyzed in Sec 2.2.1. Here we have generalized our discussion on the shift-width function. A smooth enough spectral density is a sufficient condition to obtain a Markovian evolution of $p_e(t)$ and the atom gradually releases its energy to a $\delta-$correlated in time (memoryless) environment. In our case this occurs for very weak atom-cavity coupling and can also be seen as result of the very-peaked Lorentzian-shape function $F(k)$ in (3.20), representing the excitonic component distribution of the unbound states: in the $\eta \ll 1$ limit, only states with energy very close to the atomic one are involved in the atomic emission process.
As the g/J ratio is increased, secondary oscillations are introduced as shown in Figs (3.3b) and (c). As already discussed, the amplitude α_b in (3.13) is an oscillatory term that never exactly vanishes for any finite η and gives rise to population trapping. In general, this occurs whenever a pole (external or in-continuum[3]) of the Green's function is associated to a bound state with non-vanishing component on the 'starting' state (as already seen also for the single-defect CCA in Sec. 2.3.2, where we examined the dynamics of a single-photon initally in a defect-cavity), i.e. a nonvanishing excitonic component in this case. Notwithstanding, as long as the ratio g/J is not significantly larger than zero, for all practical purposes the atom releases the entire amount

[2] We will analyze this point better in the next chapter, by dicussing the general non-Markovian behavior of quantum processes in open systems.

[3] It has been shown that bound states embedded into the band, note also as bound states in continuum (BIC), can exist in a tight-binding structured continuum without point-like gaps provided that the interaction of the localized state with the continuum is engineered in such a way to suppress discrete-continuum coupling at some frequencies inside the band [26].

of initial excitation to the field [cf. Fig. (3.3c)]. As g further approaches J [see Figs. (3.3d) and (e)] the amount of excitation that remains trapped within the atom becomes more significant, with $p_e(t)$ reducing to a stationary oscillation in the long-time limit. The oscillatory contribution $\alpha_b(t)$, given in (3.13), has an amplitude proportional to c_{e0}^2, that is the square value of the excitonic component for both bound states (see 2.88). From (2.91) it can be seen as c_{e0}^2 ranges from 0 (for $\eta \ll 1$, atom decoupled) to 1/2 (for $\eta \gg 1$, Jaynes-Cummings limit) and, consequently, $\alpha_b(t)$, oscillating at frequency ω_{0+}, has amplitude ranging from zero to 1. In the latter case the discrete eigenvalue ω_{0+}, given in (2.86), approaches to g while, from (3.17), it results $a_u(t) \approx 0$ and hence $a(t) \approx a_b(t) \approx \cos(gt)$: as expected, we retrieve vacuum Rabi oscillations corresponding to the coherent interaction between the atom and the 0th cavity [see Fig. (3.3f)]. In this limit, as opposed to the case where $\eta \ll 1$, the free-field band 'seen' by the emitter has negligible width, hence an effective single-mode behavior takes place. To summarize, one can easily identify three main regimes:

(i) almost exponential decay;

(ii) non-exponential decay (showing secondary oscillations) with no significant population trapping;

(iii) significant population trapping giving rise to fractional decay.

3.2.1.2 Field's excitation amplitudes

The photon excitation amplitude at the xth cavity is expressed also as sum of an unbound $\psi_u(x,t)$ and a bound $\psi_b(x,t)$ contribution (see (3.15) and (3.16)). With the help of (2.99), (2.100) and (2.101), for $N \gg 1$, the former can be arranged in a wave-packet form as:

$$\psi_u(x,t) = \frac{\eta}{\pi}\int_{-\pi}^{\pi} dk\, \frac{e^{-i\omega_k t}\,|\sin k|}{i\eta^2 + 4|\sin k|\cos k}\left(e^{ikx} - \frac{\eta^2 e^{i|kx|}}{\eta^2 + 4i|\sin k|\cos k}\right) \tag{3.23}$$

This describes the propagating fraction of the initial atomic excitation. Also in this case, by using the Jacobi-Anger expansion, it is possible to put $\psi_u(x,t)$ in a Bessel-expansion form as done for $\alpha_u(t)$ in (3.17), the coefficients a_n in this case resulting functions of x. This is sufficient to prove that $\psi_u(x,t)$ decays to zero at any x for enough long times. Now we want to analyze in details the localized fraction of the field, resulting from the spatial profile of the bound states. We have already discussed the field localization at $t \to \infty$ for the defect-CCA in Sec 2.3.2: the presence of a bound state with exponential decreasing probability, associated to discrete eigenvalue, allows a fraction of the initial excitation to remain localized around the defect-cavity. Now, from the discussion of Sec 2.3.3, we know that the two bound states associated with $\omega_{0\pm}$ have also a spatial profile of the form $A_0 e^{-|x|/\lambda_0}$ (see (2.95)), with $|A_0|^2 \to 1/2$, $\lambda_0 \to 0$ (and,

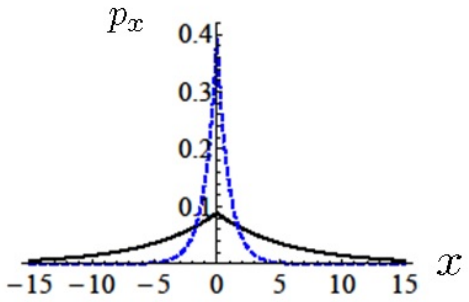

Figure 3.4: Probability profiles for bound states at resonance [see (2.88)) and (2.95))], with $\eta = 1.6$ (blue dashed line) and $\eta = 0.6$ (black line). The localization length is the monotonic decreasing function $\lambda_0(\eta)$ given in (2.95)).

at the same time, $c_{e0}^2 \to 1/2$) for $\eta \gg 1$. At resonance, a bound state with large excitonic component has, at the same time, large amplitude at $x = 0$ and small localization length. In Fig (3.4) are sketched two probability profiles for bound states with $\eta = 1.6$ (blue dashed line) and $\eta = 0.6$ (black line): the higher is the coupling constant, the narrower is the probability profile. This is in agreement with what discussed, indeed, in the $\eta \gg 1$ limit, the dynamics of the initially excited atom must involves only the 0th cavity.
In Fig (3.5) we show the time evolution of the photon probability distribution along the cavity array for the three representative values, $\eta = 0.1$ (a), $\eta = 0.8$ (b), $\eta = 2$ (c), corresponding to regimes (i), (ii) and (iii), respectively. For exponential decay [regime (i), cf. Fig. (3.3a)], the photon wave function slowly spreads along the array as shown Fig (3.5a) exhibiting a wiggled profile. At long enough times, the probability to find the photon within a finite region around the atom vanishes [see bottom panel in Fig (3.5a) which shows p_x at a very large time]. In the opposite regime [see Fig (3.5c)], when population trapping takes place [regime (iii), cf. Fig. (3.3e)-(f)] most of the photon wave function remains localized around the atom. Such localised light is periodically absorbed and next reemitted by the atom as it is clear from the top-panel diagram. In this limit, the unbound-states contribution to the field, given in (3.23), becomes negligible, hence $\psi(x,t) \approx \psi_b(x,t)$ at any x and t large enough. Due to the presence of strongly localized bound states, in the strong-coupling limit, $\psi_b(x,t)$ becomes strongly peaked around the central cavity, whose corresponding probability amplitude oscillates as $\sin(\omega_{0+}t) \approx \sin(gt)$ according to (3.16), hence most part of the field is localized close to the atom and a continuous atom-field energy exchange goes on at angular frequency $\approx 2g$.

3.2.1.3 Photon localization without fractional decay

The bound-state contribution $\psi_b(x,t)$, as well as the corresponding contribution $\alpha_b(t)$ to the atomic excitation amplitude, oscillates with finite amplitude at any finite η. Using (3.16), (2.89),

(2.90) and (2.91) we can rearrange it in an exponential form as:

$$\psi_b(x,t) = A\, \mathrm{e}^{-\frac{|x|}{\lambda_0}} \chi(t)\,, \tag{3.24}$$

where $\chi(t) = -i\sin(\omega_{0+}t)$ [$\chi(t) = \cos(\omega_{0+}t)$] for even (odd) $|x|$, while A and the localization length λ_0 (given by (2.95) and here reported for convenience) are:

$$A = \frac{\eta^5}{\left(\eta^4 + 2\sqrt{\eta^4+4}+4\right)\sqrt{\sqrt{\eta^4+4}-2}}, \quad \lambda_0 = \log\left[\frac{1}{2}\left(\sqrt{\sqrt{\eta^2+4}-2} + \sqrt{\sqrt{\eta^2+4}+2}\right)\right]^{-1} \tag{3.25}$$

In the regime (ii), as shown in Fig (3.5b), despite negligible population trapping and hence in the presence of almost-full atomic decay, a small yet appreciable fraction of the photon wave function remains localized in the neighborhood of the atom (central region of the top-panel diagram). The corresponding bottom panel shows the field profile at very long times: although most of the emitted light propagates away from the emitter, a significant photon density survives indefinitely next to the atom. Since at long enough times the field is reduced to the localized term $\psi_b(x,t)$ and the atomic amplitude to the corresponding trapped excitation amplitude $\alpha_b(t)$, both non-decaying oscillating functions representing respectively photonic and excitonic part of the surviving excitation, it is natural to assess the relative importance of each of the two contributions. In order to do this, it is convenient to define (at long times) the time-averaged localized mean photon energy as $\bar{\varepsilon}_{f\mathrm{loc}} = \sum_x \overline{|\psi_b(x,t)|^2}$ (in units of the atomic frequency) and, correspondingly, the time-averaged trapped mean atomic energy as $\bar{\varepsilon}_{a\mathrm{tr}} = \overline{|\alpha_b(t)|^2}$. Clearly the time average of $\sin^2(\omega_{0+}t)$ and $\cos^2(\omega_{0+}t)$ in $|\psi_b(x,t)|^2$ and $|\alpha_b(t)|^2$ are equal to $1/2$ and the averaged energies read:

$$\bar{\varepsilon}_{f\mathrm{loc}} = \sum_{x=-N/2}^{N/2-1}\left(A\mathrm{e}^{-\frac{|x|}{\lambda_0}}\right)^2 \overline{|\chi(t)|^2} = \frac{A^2}{2}\sum_{x=-N/2}^{N/2-1}\mathrm{e}^{-\frac{2|x|}{\lambda_0}} \overset{N\gg 1}{\longrightarrow} \frac{A^2\coth\lambda_0^{-1}}{2} = \frac{\eta^4}{2\eta^4+8} \tag{3.26}$$

$$\bar{\varepsilon}_{a\mathrm{tr}} = \overline{|\alpha_b(t)|^2} = 2c_{e0}^4 = \frac{\eta^8}{2\left(\eta^4+2\sqrt{\eta^4+4}+4\right)^2} \tag{3.27}$$

The first is equivalent to the time-averaged probability that a photon is found at $|x| \lesssim \lambda_0$ at long times and it is obtained as the $N \to \infty$ limit for an N-sites array whose central cavity (corrisponding to the 0th site) is coupled to the atom. A major feature in (3.26) and (3.27) is the different functional behaviour of $\bar{\varepsilon}_{f\mathrm{loc}}$ and $\bar{\varepsilon}_{a\mathrm{tr}}$. In particular, for small η, $\bar{\varepsilon}_{f\mathrm{loc}} \sim \eta^4$ while $\bar{\varepsilon}_{a\mathrm{tr}} \sim \eta^8$. Such different scaling is evident in Fig (3.6), where we plot $\bar{\varepsilon}_{f\mathrm{loc}}$ and $\bar{\varepsilon}_{a\mathrm{tr}}$ vs η. Either function

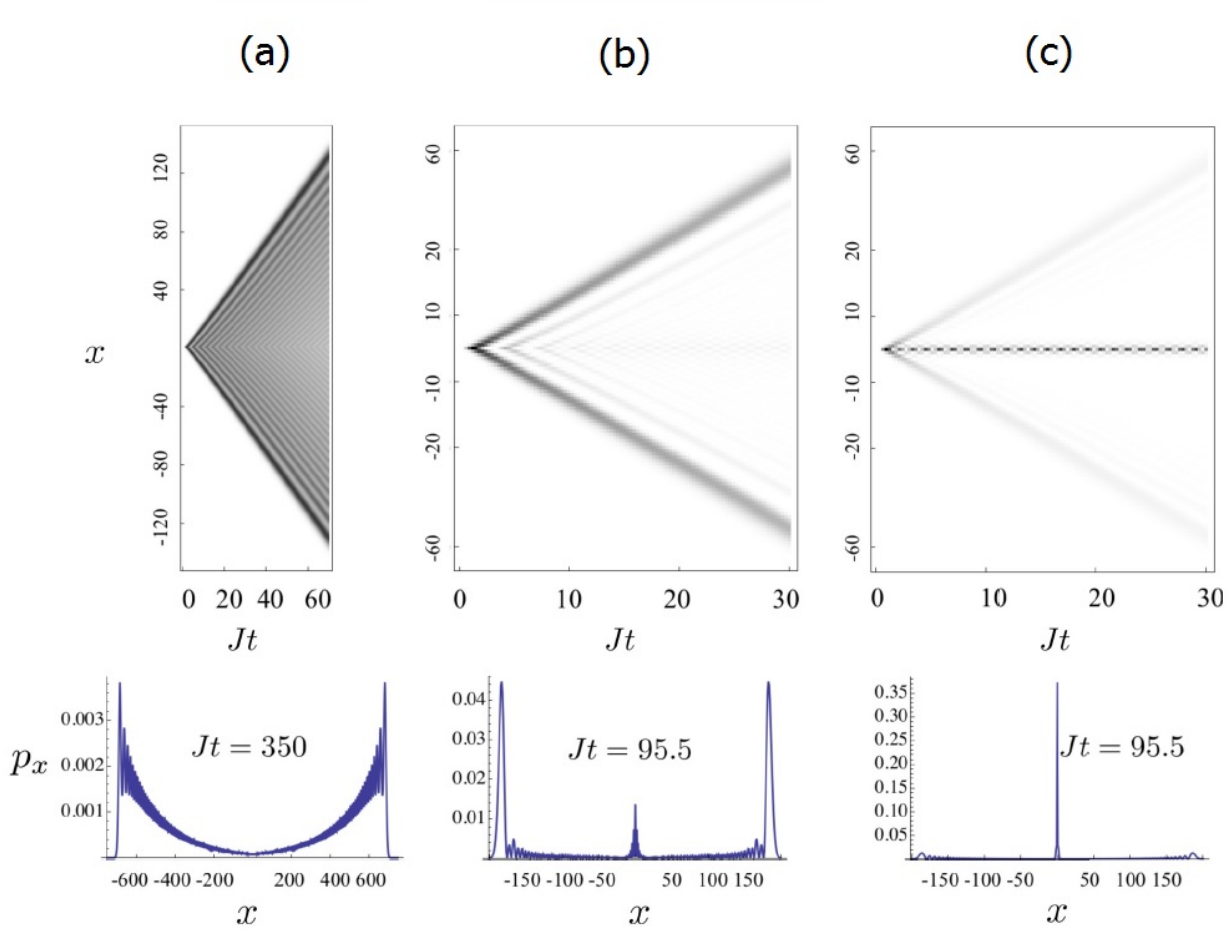

Figure 3.5: Space-time diagram of the photon probability distribution function $p_x(t)$ along the cavity array (top panels) for $\eta = 0.1$ (a), $\eta = 0.8$ (b), $\eta = 2$ (c). The bottom panels display p_x at a very large time, specifically $Jt = 350$ (a) and $Jt = 95.5$ [(b) and (c)]. Throughout, time is measured in units of J^{-1}.

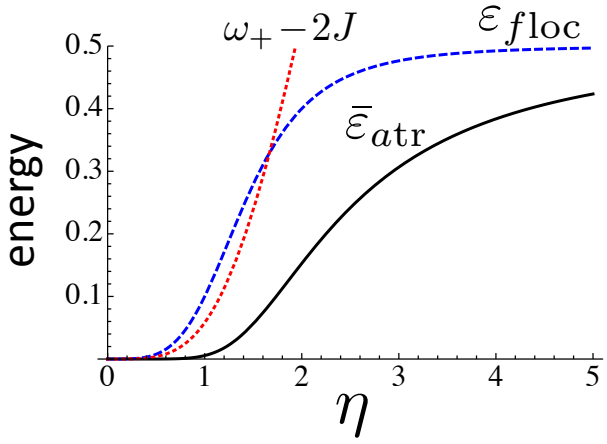

Figure 3.6: Time-averaged trapped mean atomic energy $\bar{\varepsilon}_{a\mathrm{tr}}$ (black solid line) and localized mean field energy $\bar{\varepsilon}_{f\mathrm{loc}}$ (blue dashed) against $\eta = g/J$. For comparison, we also plot the behavior of $\omega_{0+} - 2J$ (in units of J and setting $\omega_c = 0$), as given by (2.86), which measures the occurrence of bound states. $\bar{\varepsilon}_{a\mathrm{tr}}$ and $\bar{\varepsilon}_{f\mathrm{loc}}$ are in units of the atomic frequency.

vanishes at the origin and saturates to 1/2 for $\eta \gg 1$ corresponding to the expected behaviours in regime (i) and (iii), respectively. Moreover, from Fig (3.6), it is clear that the averaged energy of the localized field in general exceeds the atomic one and, compared to $\bar{\varepsilon}_{a\mathrm{tr}}$, converges to $1/2$ more quickly. Thus, it is possible to identify a particular range for η within which, at long times, significant field localization occurs but only a negligible fraction of the localized field energy is periodically returned to the atom. Clearly there are not mathematical thresholds which strictly define the onset of atomic excitation-trapping or field localization. However, because of the different scaling law, their behaviours at intermediate values are quite different, therefore we can identify physical thresholds beyond which each function is significantly different from zero. These thresholds are $\eta \simeq 0.4$ for $\bar{\varepsilon}_{f\mathrm{loc}}$ and $\eta \simeq 0.9$ for $\bar{\varepsilon}_{a\mathrm{tr}}$. This explains why as η grows from zero, field localization becomes significant before population trapping. As a consequence, within this range, the time-oscillating profile of the localized field entailed by the sinusoidal functions of $\omega_{0+}t$ [featured in $\chi(t)$] is essentially due to an energy redistribution of the field among the cavities next to $x = 0$. This behaviour can be appreciated by a closer inspection of the central region around $x = 0$ in the space-time diagrams in Figs (3.5b) and (c), which we display on a magnified scale in Figs (3.7a) and (b), respectively. In the latter case, as remarked above, the overall field intensity exhibits a periodic modulation (due to full periodic absorption of the atom). In the former case, instead, the overall intensity is nearly constant in time but periodically undergoes a substantial redistribution in space as witnessed by the long-time checkerboard-like pattern in Fig (3.7a).

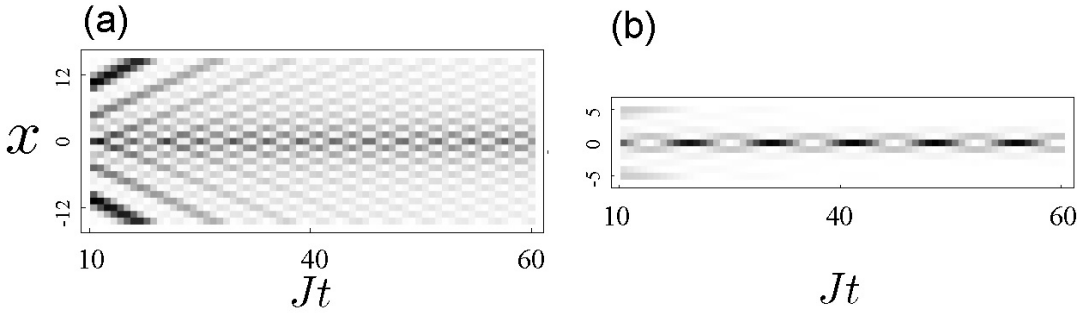

Figure 3.7: Space-time diagram of the photon probability distribution function p_x in the vicinity of $x = 0$ for $\eta = 0.8$ (a) and $\eta = 2$ (b). Time is measured in units of J^{-1}.

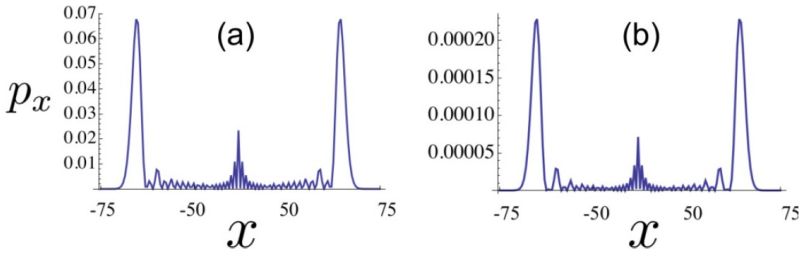

Figure 3.8: Photon probability distribution for $\eta = 0.9$ and $\Gamma/J = 0$ (a) and $\Gamma/J = 0.1$ (b) at time $Jt = 30$. The latter corresponds to $\Gamma t = 3$. Note that the scale of the p_x axis in (b) is smaller than the corresponding one in (a).

3.2.1.4 Effect of dissipation

To account for cavity leakage, in line with standard methods used in the literature, we add to Hamiltonian (2.76) a non-Hermitian term $\hat{H}_{leak} = -i\Gamma \sum_x \hat{a}_x^\dagger \hat{a}_x$, where Γ is the decay rate of each cavity. To estimate how the effect discussed above (occurrence of photon localization in absence of fractional decay) is affected, we consider the paradigmatic case where $\eta = 0.9$ and $\Gamma/J = 0.1$ (hence dissipation is rather significant). In Fig (3.8) we plot the distribution of the photon probability along the array. For comparison, the same function at the same time in the lossless case is also displayed. Clearly, the dominant effect of dissipation consists of a rescaling of the photon probability, which is expected as a consequence of the leakage. Remarkably, though, the changes in the function shape are minor and the photon localization around the atom's location is still well evident. Correspondingly, for the same values of the parameters, the atomic excitation probability exhibits a full decay (not shown), which is in fact complete at $Jt \simeq 10$ [see also Fig (3.3d)]. Therefore, on a qualitative ground and as long as the array has not decayed to the vacuum state, the presence of dissipation does not spoil the effect that photon localization occurs in absence of fractional decay. For different values of the parameters, we

numerically observed that, unless Γ/J is quite high, dissipation has in general little effect on the shape of the photon's probability distribution function. A systematic comprehensive analysis of the effect of dissipation is beyond the goals of the thesis.

3.2.2 Detuned atom-cavity coupling

It is known that an atom strongly detuned from a cavity-mode does not exchange energy with it. As discussed in Chap.1, for large detuning, the atomic probability amplitude oscillates in time with a small amplitude around a value close to unity. Hence, in the limit of very large detuning (dispersive regime) the atom does not decay at all.
Here we analyze the general behaviour, as a function of the atom-cavity detuning, of the time-averaged energies $\bar{\varepsilon}_{a\mathrm{tr}}$ and $\bar{\varepsilon}_{f\mathrm{loc}}$ we have introduced above. We expect that the atomic trapped energy, for a given η, increases more quickly than the corresponding localized energy for increasing values of the detuning. Indeed, for a very far-detuned interaction, the atom cannot release energy to the field. In Sec 2.3.3 we have discussed the general expressions of the bound states, given by (2.93), and we have expressed the localization lengths, given in (2.94), as a function of the eigenvalues $\omega_\pm$ which, in turn, are functions of g, J and $\delta_{ac} = \omega_a - \omega_c$ (the energy scale is defined here considering $\omega_a = 0$). It should be stressed that the RW approximation holds if $g, \delta_{ac} \ll \{\omega_c, \omega_a\}$ and $J \ll \omega_c$.
In the following the atom-cavity detuning is indicated with δ and its rescaled value with $\tilde{\delta} = \delta/J$. As remarked above, the eigenenergies corrspond to the discrete poles of the Green's function, i.e. the (real) solutions of quartic equation (2.85). Their explicit expressions are reported in Appendix C. By means of these solutions, using (2.94), in Figs (3.9a) and (c) we plot the lengths λ_+ and λ_- associated, respectively, with $|\psi^+\rangle$ and $|\psi^-\rangle$, as a function of η and $\tilde{\delta}$. It can be seen that, if $\delta > 0$, the localization length associated with $|\psi^+\rangle$ is smaller than the corresponding value at resonance (given in (3.25)), while λ_- is larger than λ_0. Moreover, Figs (3.9b) and (d) show also the behaviour of the squared excitonic components $|c_{e\pm}|^2$ (cf. (2.94)) as a function of η and $\tilde{\delta}$. They are also unbalanced so that, as $\tilde{\delta}$ grows from zero, the bound state '+' (the bound state '-') has $|c_{e+}|^2$ ($|c_{e-}|^2$) larger than (smaller than) the corresponding value at resonance c_{e0}^2 (given in (2.91)). Hence, by increasing the detuning ($\delta > 0$) for a given η, $|\psi^+\rangle$ will show a more lolcalized profile and, at the same time, its excitonic component will increase and $|\psi^-\rangle$ will exhibit an opposite behaviour. However, Fig (3.9) shows also that localization lengths as well as excitonic components of $|\psi^+\rangle$ and $|\psi^-\rangle$ are not simmetrically unbalanced. For $\delta > 0$, λ_+ and $|c_{e+}|^2$ show a rapid transition, respectively to zero and one, when δ grows beyond the band-edge value $2J$. This variation is the more rapid, the smaller the coupling. On the other hand λ_- and $|c_{e-}|^2$ exhibit a different behaviour, showing always a smooth variation within the $\tilde{\delta} > 0$-semiaxis for any η. For $\delta < 0$ the situation is reversed (not shown in figure), indeed, the negative threshold is $\delta = -2J$ and the '-' bound state has localization length and excitonic component which vary quickly beyond the negative band-edge. This is a reflection of the behaviour of the two eigenvalues $\omega_\pm$. These are plotted in Fig (3.10), referred to the center of the

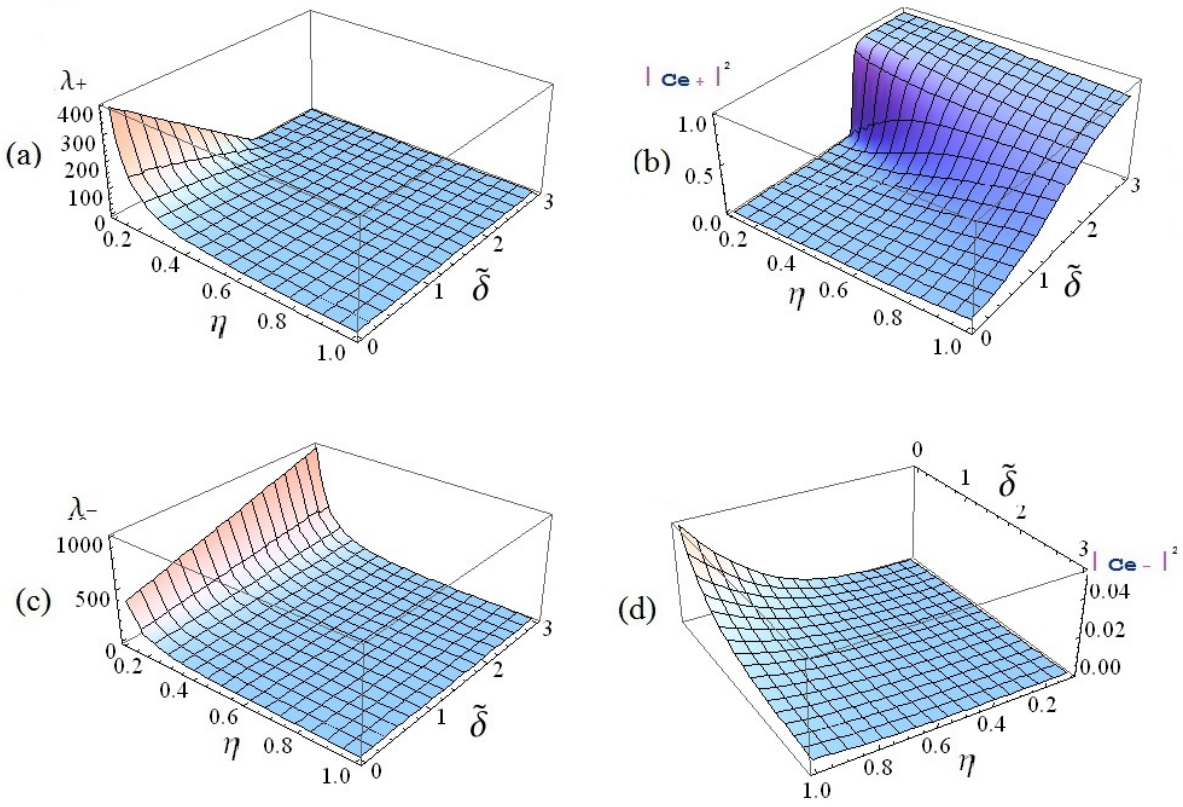

Figure 3.9: Localization lengths of the bound states and square values of the excitonic components as a function of η and $\tilde{\delta}$: λ_+ (a), λ_- (c), $|c_{e+}|^2$ (b), $|c_{e-}|^2$ (d).

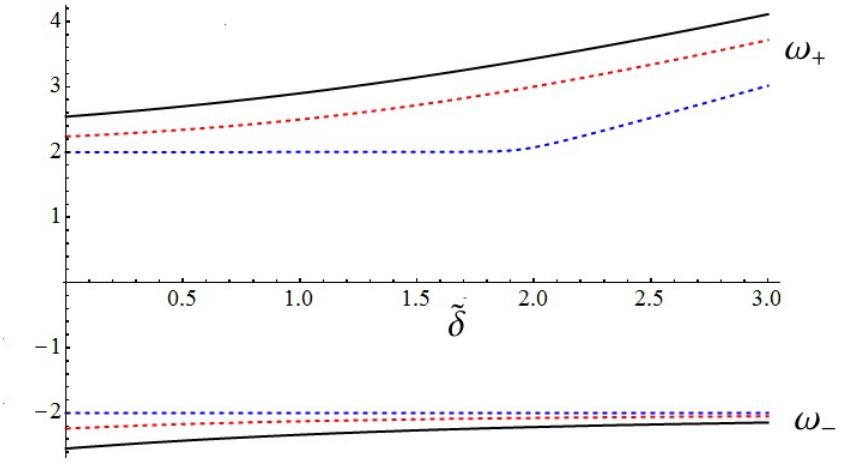

Figure 3.10: Discrete eigenvalues ω_+ and ω_- in units of J referred to the center of the band, real solutions of (2.85), as a function of the detuning for $\eta = 0.2$ (blue dashed), $\eta = 1.5$ (red dotted) and $\eta = 2$ (black).

band, when $\tilde{\delta}$ varies around the positive band-edge, for different values of η. When η is small enough, ω_+ reaches its minimum value at $\tilde{\delta} \approx 2$ and, under this threshold, it is quickly stopped at $\omega_+ \approx 2J$. For higher values of η, when the detuning is decreased under $\tilde{\delta} = 2$, it approaches the corresponding resonant-value more gradually. The behaviour of ω_- for negative detuning around $\tilde{\delta} = -2$ is analogous. In Fig (3.10) the negative eigenvalue is also shown. It smoothly crosses the threshold $\tilde{\delta} = 2$ and approaches the negative band-edge value for detuning large enough. In the limit $\tilde{\delta} \gg \eta$ (dispersive regime) we found a purely excitonic state $|\psi^+\rangle$ (with $\lambda_+ = 0$) and a completely delocalized state $|\psi^-\rangle$ (with $c_{e-} = 0$) or opposite situation for negative detuning.

Here we want to analyze the general behaviour of $\bar{\varepsilon}_{a\mathrm{tr}}$ and $\bar{\varepsilon}_{f\mathrm{loc}}$, therefore we are not interested in the propagating fraction of the excitation. So we calculate the state $|\Phi(t)\rangle$ with an expression analogous to (3.10), but only including the bound-states contributions to the evolution. We start with the same initial condition $|\Phi(0)\rangle = |e\rangle$, hence the polaritonic state at time t reads:

$$|\Phi_b(t)\rangle = \sum_{\mu=\pm} c^*_{e\mu}\, e^{-i\omega_\mu t} |\psi^\mu\rangle \tag{3.28}$$

with bound-states $|\psi^\pm\rangle$ given in (2.93). Thus, the atomic amplitude reads:

$$\alpha_b(t) = \langle e|\Phi_b(t)\rangle = \sum_{\mu=\pm} |c_{e\mu}|^2 e^{-i\omega_\mu t} = \eta^2 \left[\left| \frac{A_+}{\omega_+} \right|^2 e^{-i\omega_+ t} + \left| \frac{A_-}{\omega_-} \right|^2 e^{+i\omega_- t} \right] \tag{3.29}$$

where, from (2.94), we took into account the relation $c_{e\pm} = gA_{\pm}/\omega_{\pm}$. By projecting (3.28) onto $|x\rangle$, the expression for the bound-states contribution to the field amplitude reads:

$$\psi_b(x,t) = \langle x|\Phi_b(t)\rangle = \left[\frac{|A_+|^2}{\omega_+}e^{\left(-\frac{|x|}{\lambda_+}-i\omega_+ t\right)} + \frac{|A_-|^2}{\omega_-}e^{\left(-\frac{|x|}{\lambda_-}+i\omega_- t\right)}\right] \tag{3.30}$$

Following the definition of $\bar{\varepsilon}_{a\mathrm{tr}}$ given in (3.27) for the resonant case, we obtain:

$$\bar{\varepsilon}_{atr} = \overline{|\alpha_b(t)|^2} = \eta^4\left[\left|\frac{A_+}{\omega_+}\right|^4 + \left|\frac{A_-}{\omega_-}\right|^4\right] \tag{3.31}$$

Here the time-average of $|\alpha_b(t)|^2$ is obtained from (3.29) which includes oscillating terms with zero time-average. Thus, the trapped energy depends on $|A_\pm|$ and $\omega_\pm$ which are, in turn, functions of η and δ. In the same way, following the definition of $\bar{\varepsilon}_{f\mathrm{loc}}$ given in (3.26), from (3.30) the field-localized mean energy reads:

$$\bar{\epsilon}_{floc} \to \sum_{x=-\infty}^{+\infty}\overline{|\psi_b(x,t)|^2} = \eta^2\left[\frac{|A_+|^4}{|\omega_+|^2}\left(\frac{e^{2/\lambda_+}+1}{e^{2/\lambda_+}-1}\right) + \frac{|A_-|^4}{|\omega_-|^2}\left(\frac{e^{2/\lambda_-}+1}{e^{2/\lambda_-}-1}\right)\right] \tag{3.32}$$

where, also in this case, the functional dependence on η and on δ is implicitly contained in $|A_\pm|$, $\lambda_\pm$ (given in (2.94)) and $\omega_\pm$. Using for the latter ones the exact solutions of (2.85) (reported in Appendix C), we plot in Fig (3.11) the behaviour of $\bar{\varepsilon}_{f\mathrm{loc}}$ and $\bar{\varepsilon}_{a\mathrm{tr}}$ and their ratio as a function of η and $\tilde{\delta}$. As expected, the trapped atomic energy turns out to be a monotonic function of both η and $\tilde{\delta}$ (Fig (3.11b)). Setting $\tilde{\delta} > 2$, it results $\bar{\varepsilon}_{a\mathrm{tr}} \approx 1$ when the coupling is small enough. By increasing η from zero, the trapped energy approaches $1/2$ (i.e. its saturation value of the strong-coupling resonant case) when $\eta \gg \delta$. On the other hand, for $\tilde{\delta} < 2$, the trapped energy shows a behaviour similar to that of the resonant case, approaching $1/2$ from zero when η is increased. We can see that $\bar{\varepsilon}_{a\mathrm{tr}}(\tilde{\delta})$ for very low coupling is a 'step-function' in the limit $\eta \to 0$ (clearly, the singular case $\eta = 0$ is not included), showing a sudden variation around $\tilde{\delta} = 2$. This behaviour reflects that of the localization length and excitonic-component of $|\psi_+\rangle$ plotted in Fig (3.9b), which, at small η, provides the main contribution to the atomic dynamics and it arises from the mathematical properties of $\omega_\pm$. In this case, indeed, the condition $\tilde{\delta} \gtrless 2$ determines if the atom can release its energy to the field or less. At very small coupling and $\tilde{\delta} > 2$ the atomic excitation is locked and the system works in the dispersive regime, i.e. the atom exchanges a small fraction of its energy, at long times, only with the central cavity and it oscillates with a very small amplitude around a value close to one (see (1.12)), at the effective-Raby frequency $g' = \sqrt{g^2 + \delta^2/4} \approx \delta/2$ [cf. Fig 1.3]. For $\tilde{\delta} < 2$, instead, the atomic frequency falls inside the photonic band and the atom will release entirely its excitation to the field showing an alomst

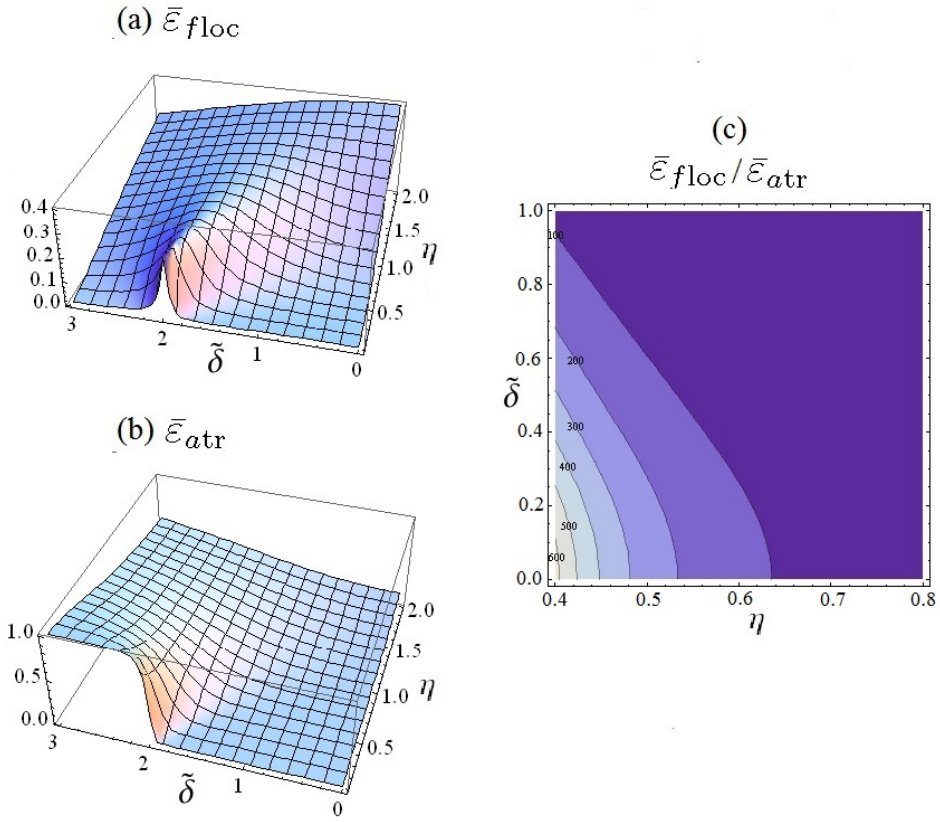

Figure 3.11: 3D Plots of $\bar{\varepsilon}_{floc}$ (a) and $\bar{\epsilon}_{atr}$ (b) for $0.1 < \eta < 2$, $0 < \tilde{\delta} < 3$. Contour plot of $\bar{\varepsilon}_{floc}/\bar{\epsilon}_{atr}$ for $0.4 < \eta < 0.8$, $0 < \tilde{\delta} < 1$ (c).

markovian behaviour. Setting η to a generic value, the two opposite situations of resonant and dispersive coupling are anyhow reached but now, the transition to the dispersive regime occurs more gradually. As shown in (Fig (3.11b)), this transition is the more slow the larger the coupling. Clearly, at any finite η, the release of atomic energy to the localized field is possible even if $\tilde{\delta} > 2$ because the two bound states have nonvanishing photonic components. This is a consequence of the fact that, at any finite coupling, the two discrete eigenvalues are not collapsed into the band. In Fig (3.11a) we plot the localized mean energy as a function of η and $\tilde{\delta}$. In this case the profile of $\bar{\varepsilon}_{f\mathrm{loc}}$ vs η is monotonic too, but its behaviour as a function of $\tilde{\delta}$ is not monotonic for η small enough. When the coupling is not too large (approximately less then 1.7), the localized energy against $\tilde{\delta}$ increases until reaching a maximum and then, by further increasing the detuning, it drops to zero. This is also shown in Fig (3.12a) for $\eta = 0.7$, where the point at which the two energies are equal roughly corresponds to the maximum of $\bar{\varepsilon}_{f\mathrm{loc}}$. Fig (3.12b) shows, for $\eta = 2$, a monotonic behaviour of both $\bar{\varepsilon}_{f\mathrm{loc}}$ and $\bar{\epsilon}_{atr}$. For η small enough, the function $\bar{\varepsilon}_{f\mathrm{loc}}(\tilde{\delta})$ is very peaked around $\tilde{\delta} = 2$, correspondingly to the rapid transition of the atomic trapped energy. This reflects the sudden drop of λ_+ when $\tilde{\delta}$ crosses the band-edge value

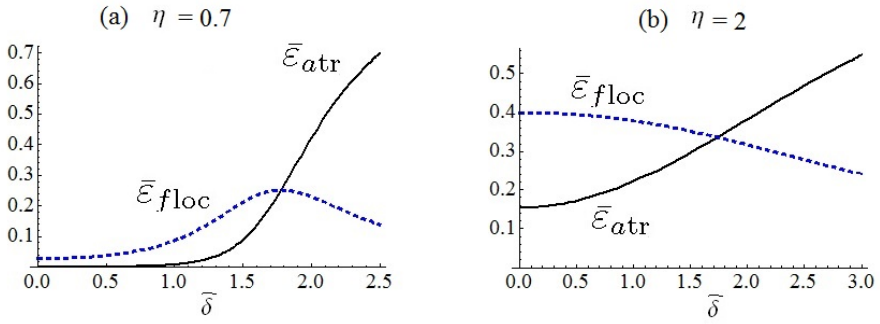

Figure 3.12: Plots of $\bar{\epsilon}_{floc}$ and $\bar{\epsilon}_{atr}$ as a function of $\tilde{\delta}$ for $\eta = 0.7$ (a) and $\eta = 2$ (b).

[see Fig (3.9a)], indeed the excitonic bound state ($|\psi_+\rangle$ for $\delta > 0$), at small η, shows a rapid transition to a completely localized state.
Population trapping as a function of the atom-field detuning has been examined for several models of photonic band gab structures [29, 30, 33]. John and Wang [32] proposed for the first time a simple qualitative model for an infinite PBG structure based on the idea of a spherical Brillouin zone. They introduced an isotropic model, assuming that a propagating photon experiences the same periodic potential no matter what the polarization or the direction of propagation is. This model is characterized by a semi-infinite band with divergent d.o.s. at the band edge. When the atomic frequency is chosen at the band-edge, a substantial fraction of the population in the initial excited atomic state remains trapped and $P_e(t) \to 4/9$ at long times. This population trapping is significantly reduced if the atomic fraquency falls inside the band ($\delta > 0$), while $P_e(t) \to 1$ for atomic transition far enough from the band-edge ($\delta < 0$) [30]. Our model, in the $\eta \ll 1$ limit, shows qualitatively a similar behaviour. In this case, indeed, if the atomic frequency is chosen near the positive band-edge ($\tilde{\delta} > 2$), the long time dynamics of the atomic and field excitation is dominated by the '+' bound state and the behaviour is similar to a corresponding semi-infinite band model (the other bound state plays no role). In general, in a system characterized by a structured reservoir with divergent spectral density, external bound states with significant excitonic component can arise even at small coupling, by suitably choosing the atomic frequency near or outside the band-edge.
In Fig (3.11c) is shown a contour plot for the ratio $\bar{\epsilon}_{floc}/\bar{\epsilon}_{atr}$ as a function of η and $\tilde{\delta}$. The values of η are chosen within the range for which, at resonance, there is photon localization with negligible population trapping. The ratio is always a monotonic decreasing function of both η and $\tilde{\delta}$, hence, although for a given (not too large) value of η it is possible to localize more energy into the field by adjusting the detuning, correspondingly an increase of $\bar{\epsilon}_{atr}$ will occur so that their ratio is decreased [see also Fig (3.12a)]. The contour plot shows that the effect of localization without population trapping is present even if the atom is detuned from the cavity mode but, as δ increases, the range of η for which the effect persists is shrinked.

3.3 Single photon scattering

Now we briefly analyze the coherent transport of a single photon, which propagates through the array from an extreme toward the center and is scattered by the TLS. By setting η and adjusting the detuning, the atom can be seen as a controllable quantum switch for the photon coherent transport.

We emphasize that on energetic grounds a single photon cannot excite the photon-atom bound states described above and, therefore, these states are of no relevance in single-photon scattering calculations. The TLS (partially) absorbs an incoming single photon and a decomposition of the system's initial state into the (polaritonic) single-particle eigenstates given in (2.98), with $x-$ and $e-$components respectively in (2.99) and (2.101), does not involve the bound states. Thus, the excited TLS will eventually decay into its ground state. The bound states can be energetically reached via multiphoton scattering processes. For example, in [19] is demonstrated that when a propagating two-photon wave packet interacts with the TLS, a sizable fraction of the photon population becomes trapped at the TLS site. In other words, once the TLS is appreciably excited by one of the incoming photons, the remaining photon sees a modified (saturated) TLS and is thus (partially) scattered into the hitherto unreachable bound photon-atom states via multiparticle scattering processes. After the scattering is complete, the bound states are again decoupled from the continuum and, thus, cannot decay.

The reflection amplitude $r(k)$ is given in (2.100) and the corresponding reflection coefficient $R(k) = |r(k)|^2$ is maximum, at resonance, for $k = \pm\pi/2$, i.e for a photon resonant with the atomic frequency ($\omega = 0$, with the energy scales adopted here) that results, hence, completely reflected by the atom. In this case the TLS behaves as a perfect mirror, therefore as proposed in [17], a TLS with tunable frequency can be used as a quantum switch to control the coherent transport of photons.

Figs (3.13a) and (b) show a phase diagram of $R(k)$, for two non-resonant values of k, as a function of η and $\tilde{\delta}$. The scattering process, as it can be seen, degenerates to a total reflection for each k in the limit $\eta \gg 1$ (in the white area the reflection is nearly one). In this limit there is no energy exchange between free propagating (single) photons and the atom because all unbound states have almost vanishing excitonic components (cf. (2.101)).

In Fig (3.14a) and (b) are shown the reflection coefficients as a function of k, respectively at resonance and with $\tilde{\delta} = -1$. Because of the nonlinear dispersion, the line shape of the reflection coefficient results more general with respect the Breit-Wigner or Fano resonances [17]. For detuning small enough, $R(k)$ fits well the Breit Wigner line shape in the region $k \approx \pm\pi/2$, indeed by expanding the cosine around $k = \pm\pi/2$ we have:

$$r(k) \approx \frac{ig^2}{2J(-\delta - \pi J \pm 2Jk) - ig^2} \tag{3.33}$$

whose square value represents a B-W resonance with line width proportional to η^4.

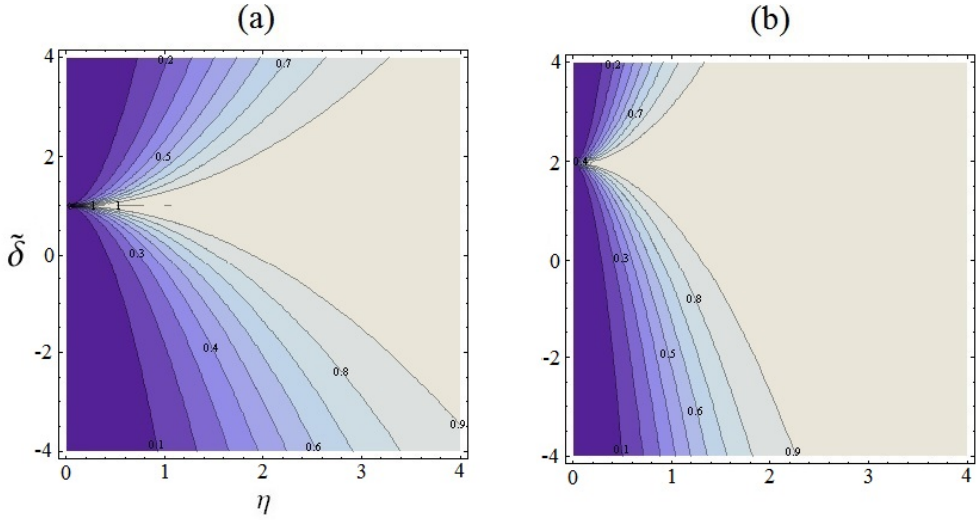

Figure 3.13: Contour plots of the reflection coefficient $R(k) = |r(k)|^2$ [see (2.100)] as a function of η and $\tilde{\delta}$ for $k = \pi/3$ (a) and $k = \pi/15$ (b).

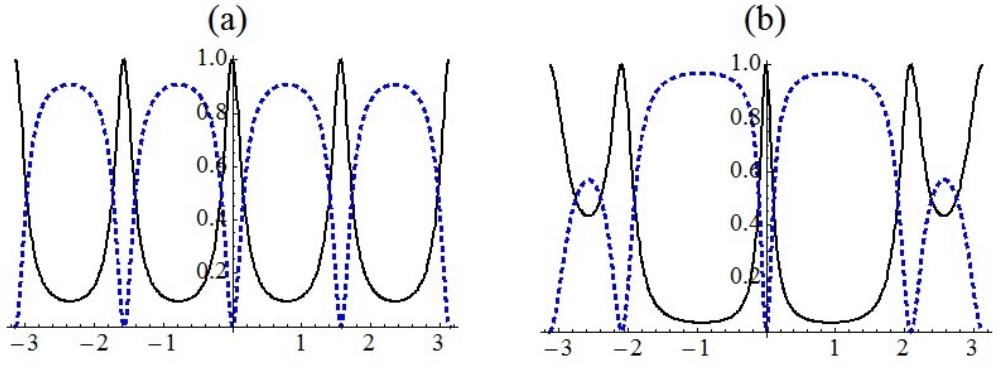

Figure 3.14: Reflection coefficient $R(k) = |r(k)|^2$ (black solid) and transmission (blue dotted) as a function of k for $\tilde{\delta} = 0$ (a) and $\tilde{\delta} = -1$ (b).

Chapter 4

Static disorder in Coupled Cavity Arrays

It is well-known that electrons in a crystalline solid show electrical conductivity thanks to a constructive interference among various scattering trajectories. The wave nature of the electron gives rise to allowed energy bands and forbidden gaps for its motion in the solid. Disorder in the crystal hinders electrical conductivity, and for some energies the electronic wavefunctions are localized in space. The phenomenon of localization, being, in the first instance, a property of the states in random quantum mechanical systems, has its most striking experimental manifestation in the transport properties of condensed matter systems. Indeed, the one-particle wavefunctions in macroscopic, disordered quantum systems at the absolute zero can be exponentially localized. This means that, on average, their amplitudes are exponentially decaying in space at infinity. This remarkable phenomenon, first discussed by Philip W. Anderson in 1958 [60] but fully appreciated only in the last decades, arises from wave interference, an effect common to both photons and electrons. Beyond a critical amount of impurity scattering, Anderson discovered, the diffusive, zigzag motion of the electron is not just reduced, it can come to a complete halt. The electron becomes trapped and the conductivity vanishes. This effect, known as *Anderson localization*, is a general wave phenomenon that applies also to the transport of electromagnetic waves, acoustic waves, spin waves, etc. It has also been observed by localization of a Bose-Einstein condensate in a 1D disordered optical potential [78], by localization of light in an optical fiber medium [73], in certain dielectric microstructures [74] and strongly confined Anderson-localized cavity modes are been generated by deliberately adding disorder to photonic crystal waveguides [79]. Anderson localization finds its origin in the wave interference between multiple-scattering paths. In the strong scattering limit, the distructive interferences can completely halt the waves inside the disordered medium.
In Sec. 2.3.2 we have seen that an uniform CCA whose perfect periodicity has been broken at just one site, where the cavity mode has a frequency different from the others, has a localized eigenstate, associated with an eigenvalue out of the band, whose spatial extension depends on the absolute-value difference between the defect-mode frequency and the array's modes one. The defect-cavity acts as a scattering center and, if it is initially excited, there will be fractional

decay and photon localization with exponential profile, at long times, around the defect. In Chap.3 we have investigated the photon localization and population trapping which arise from the emission of a TLS coupled to the central cavity of an uniform CCA. In this case the atom acts as a scatterer for a photon propagating through the array and impinging on it. Localization and trapping of the polaritonic excitation, taking place when the atom is initially excited, are phenomena mathematically related to the presence of a pair of localized states, both with exponential profile qualitatively similar to the defect-CCA's bound state. If now we couple the atom, initially excited, to an infinite CCA with a defect-cavity located in a generic site, we expect that a fraction of the atomic excitation will be back-scattered by the defect and will excite again the atom and so on. In this way we should expect a significant revival of the atomic population even in the strong-hopping limit in which, for an uniform CCA, the atom would decay showing a nearly Markovian behaviour. Of course, the frequency of these secondary revivals will depend on the distance between the atom and the defect-cavity, i.e. on the time taken by the atomic excitation to reach the defect and come back to the atom. If we now consider a completely disordered infinite CCA, with random cavity frequencies statistically independent on the position (but uniform in the hopping rate), each cavity will behave as a defect and will back-scatter a fraction of the atomic excitation impinging on it. In this way, for strong enough disorder, there will be incoherent sum of excitation amplitudes in almost all sites except in the central one, from which the atom would begin to decay eventually releasing its energy to the field if the system was uniform. In other words, the atomic strong-hopping Markovian decay is prevented and, for strong enough disorder, the atom can't get rid of its excitation.
As we will see below, one of the main aspects of one-dimensional Anderson Localization is that, in presence of static disorder, all the eigenstates are localized and exhibit a probability profile, in $x-$representation, the more localized the stronger the disorder.
This is the scenario of Anderson localization for Coupled Cavity Arrays we shall analyze in this chapter. More precisely here we study the atomic emission, in the strong-hopping limit, for different strengths of static disorder described by random cavity-mode frequencies with normal probability distribution. Using the *open quantum systems* approach, we analyze, from a more general perspective, the Non-Markovianity for the coupling between the TLS and the disordered-CCA. The latter performs a particular environment, characterized by a given set of eigenmodes whose energy and position-distribution depend on the disorder strength. The measure for the Non-Markovianity of the quantum process, which we will introduce in Sec. 4.2, quantifies the complexive back-flow of information from the environment to the system during the entire dynamics. This quantity does not depend on the initial atomic state, but it represents a general property of the quantum dynamics arising from the TLS-environment coupling and vanishes for Markovian processes. In this latter case (never exactly verified if the environment consists of a CCA, either uniform or disordered) the information 'stored' into the TLS state will always flow away from the system to the environment and all possible atomic initial states will be brought into a single common final state that, in all cases described by the general Fano-Anderson Hamiltonian (1.1) with an almost-flat spectral density, is the ground one. We link the Non-Markovianity measure with a representative quantity of the disorder strength of the CCA,

which we introduce in the next section, that measures the spatial extention of the near-resonant eigenstate for a given dirorder realization. In this way we demonstrate that the quantum evolution of an atom interacting with a disordered array, for small enough disorder and by averaging over many realizations with a given standard deviation, is comparable to that for which the environment consists of an open ($\gamma \neq 0$) non-dissipative single-mode cavity with a suitable volume (i.e. with a suitable coupling constant).

4.1 Anderson Localization in Coupled Cavity Arrays

In what follows we describe a model which accounts for the disordered CCA, described by the following 1D Anderson Hamiltonian with uniform hopping and random local frequencies:

$$\hat{H} = \sum_{x=-\infty}^{+\infty} \omega_x \hat{a}_x^\dagger \hat{a}_x + J \sum_{x=-\infty}^{+\infty} \left(\hat{a}_x^\dagger \hat{a}_{x+1} + h.c. \right) \tag{4.1}$$

In Fig (4.1) is sketched the array with static disorder, in which the cavity at the $x-$site has a single-mode of random frequency ω_x, statistically independent on the position. Our analysis will be restricted to the strong-hopping limit of the TLS-CCA coupling, so that the eigenfunctions of the disordered bare array are not substantially modified. The disorder may be due to an imperfect production technique (in figure different cavity-volumes are associated with different mode-frequencies) or may be deliberately added [79].
Analogous models were proposed, in its pioneeristic work dating back to 1958 [60], by Philip W. Anderson to study the diffusion of an electron in 1D, 2D and 3D crystalline structures. What he found was that even weak potential perturbations causes a suppression of electronic diffusion. He postulated that a disordered potential will cause the plane wave like Bloch states of the non-disordered system to scatter and destructively interfere with one another. This interference causes the new eigenstates of the system to be spatially localized in the material. As a consequence, an electron that occupies a localized state will not be able to conduct through the system. This is the phenomenon of Anderson localization we have introduced above and in solid-state physics it is due to the presence of crystalline impurities, topological defects, vacancies, dislocations etc. Moreover, Anderson showed that the dimensionality of the system and strength of the disorder play a key role. In 1D and 2D, for arbitrary disorder, the space-probability distribution for a single excitation remains localized within a region whose dimension depends on the disorder. In 3D, instead, for small enough disorder, the probability distribution diffuses in time. Three-dimensional systems show regions, in energy space, of localized and extended states that are sharply separated at particular values of energy. These energies are referred to as mobility edges [1]. Much progress in understanding localization was due to the development of an *one parameter scaling theory* [65] which was based on the earlier work by Thouless on

[1] This makes possible the Anderson quantum phase transition in certain three-dimensional solids.

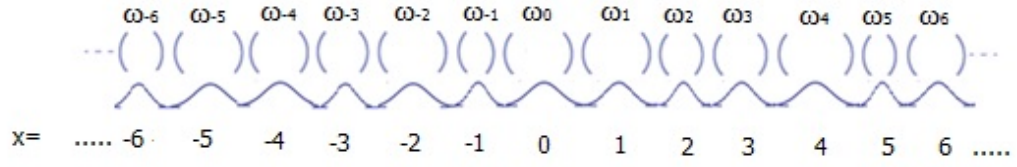

Figure 4.1: Coupled cavity array with static disorder. The single-mode cavity frequencies ω_x are random variables statistically independent on the position. The random distribution of the frequencies may be due to an imperfect fabrication technique that gives rise to cavities with different mode-volumes. The hopping rate is assumed uniform.

the quantum conduction in thin wires [64]. The theory describes the flow of the dimensionless conductance $\mathcal{G}(L)$ under rescaling:

$$\beta(\mathcal{G}) = \frac{d \log \mathcal{G}(L)}{d \log L} \tag{4.2}$$

where L is the linear size of the system and $\beta(\mathcal{G})$ is independent on L but depends on the model studied. Thouless point is that Anderson localization sets in when the energy level widths are smaller than the level separation. The ratio of both energies is the dimensionless Thouless conductance $\mathcal{G}(L)$, so the condition $\mathcal{G} < 1$ represents a criterion for Anderson localization. The one-parameter scaling theory predicts that, when the time-reversal and spin-rotation symmetries are preserved (in the absence of magnetic field and spin-orbit coupling, for condensed-matter systems), in 1D and 2D all one-particle states are localized, and therefore no mobility edge exists, even if disorder is very weak.

4.1.1 Quantitative description of localization for the 1D Anderson Hamiltonian

The tight-binding Anderson Hamiltonian (4.1), describing several one-dimensional systems including the disordered CCA, exhibits localized eigenstates for any kind of disorder with arbitrary strength. If, in the single excitation subspace, c_x is the probability amplitude at the xth site for a generic eigenstate of energy E, the time-independent Schrödinger equation reads:

$$E c_x = \omega_x c_x + J\,(c_{x+1} + c_{x-1}) \tag{4.3}$$

It is possible to prove that the amplitudes c_x show the asymptotic behaviour:

$$c_x = f_x e^{-|x|/\lambda} \tag{4.4}$$

where f_x is a random function of the position and, in the limit of zero disorder, for each eigenstate $\lambda \to \infty$. This is an intuitive but not very usefull definition of localization length.
For 1D systems the localization length may be calculated from the limiting behaviour of products of random matricies [66, 68]. This method provides, at the same time, a proof that each eigenstate has a localized profiles in presence of arbitrary disorder. It is an equivalent representation of the Schrödinger equation (4.3) and is based on the Tranfer Matrix defined as follows:

$$\begin{bmatrix} c_{n+1} \\ c_n \end{bmatrix} = \hat{T}_n \begin{bmatrix} c_n \\ c_{n-1} \end{bmatrix} \tag{4.5}$$

where the transfer matrix for the eigenstate with energy E is given by:

$$\hat{T}_n = \begin{bmatrix} (E - \omega_n)/J & -1 \\ 1 & 0 \end{bmatrix} \tag{4.6}$$

in which the ω_ns are the random frequencies for each cavity and (4.3) can be derived by carrying out the matrix multiplication in (4.5). For an $(N + 1)-$sites array we can calculate the total transfer matrix across the entire array by successive matrix multiplications:

$$\hat{Q}_N = \hat{T}_1 \hat{T}_2 \hat{T}_3 ... \hat{T}_N \tag{4.7}$$

that satisfies the theorem of Oseledets [61], i.e. there exists a limiting matrix for the infinite array:

$$\hat{\Omega} = \lim_{N \to \infty} \left[\hat{Q}_N \hat{Q}_N^\dagger \right]^{1/(2N)} \tag{4.8}$$

For 1D systems $\hat{T}_n$, $\hat{Q}_N$ and $\hat{\Omega}$ are 2×2 matricies. The two eigenvalues of the limiting matrix $\hat{\Omega}$ are inverses each other and we refer to these as $e^{\pm\tilde{\gamma}}$, where $\pm\tilde{\gamma}$ are the characteristic *Lyapunov exponents* of $\hat{Q}_N$ in the limiting case. In general, the smallest of these eventually determines the slowest possible exponential increase of the state for $x \to \infty$. To calculate the generic pair of amplitudes (c_x, c_{x-1}) for the given eigenstate using the transfer matricies, we choose the initial pair $(c_1, c_0) = (1, 0)$, the choice being arbitrary. Using (4.6) and (4.7) it is possible to show that the final vector can then be related to the lowest Lyapunov exponent (the negative one) by [68]:

$$-2\tilde{\gamma}(E) = \lim_{x \to \infty} \frac{1}{x} \log \left(c_x^2 + c_{x-1}^2 \right) \tag{4.9}$$

This means that the amplitudes c_x of the eigenstate of energy E are exponentially decreasing for $x \to \infty$ with characteristic length $\tilde{\gamma}^{-1}(E)$ and it is possible to identify this with the localization length of the eigenstate [2].

[2]This is proven to be a self-averaging quantity

Knowledge of the time-independent Green's function provides another way to define the localization length for a given eigenstate and to relate it to the spectral properties of the system. The absolute square of the Green's function matrix element $G(x, x'; E)$ represents the probability for the transition of an excitation of energy E from the site x to x'. This is also referred as transmission probability and, in all cases in which it decays exponentially for large distances, it may be used to define the localization length at energy E as follows:

$$\frac{1}{\lambda} = -\lim_{N\to\infty} \frac{1}{2N} \log \left|G^{+}(1, N; E)\right|^2 \tag{4.10}$$

where $G^{+}(1, N; E)$ is the analytic continuation of the Green's function between the sites 1 and N as defined in (2.5) and the localization length so obtained is always finite in 1D disordered systems. Moreover, for a finite discrete system, the matrix element $G(1, N; z)$ has a pole for each eigenvalue E_i whose residue is $c_1^i c_N^i$. In this way Thouless calculated the localization length[3] of the $j-$th eigenstate as its fall-off distance in the limiting case [63]:

$$\lambda_j^{-1} = \lim_{N\to\infty} \frac{1}{N-1} \sum_{i\neq j} \log\left(\epsilon_j - \epsilon_i\right) \tag{4.11}$$

in which ϵ_i are the eigenvalues in units of J. This formula is very useful to compute numerically the localization lengths. For a long statistically homogeneous array the sum over states can be replaced by an integral over the density of states and the localization length reads:

$$\lambda^{-1}(E) = \int_{-\infty}^{\infty} \rho(z) \log\left(E - z\right) dz \tag{4.12}$$

If the Green's function is known (or can be numerically calculated), it is possible to calculate $\rho(z)$ using the following useful expression [90]:

$$\rho(z) = -\frac{1}{\pi} \Im m\{Tr[\hat{G}^{+}(z)]\} \tag{4.13}$$

The parameter that we will use in the following, characterizing the localization of eigenstates, is the *inverse partecipation number* or *inverse partecipation ratio* [67]. It is a measure of the portion of space where the amplitude of the eigenfunction differs markedly from zero and, for a given normalized eigenstate with $x-$amplitudes $c_x = \langle x|\psi\rangle$, it is defined as:

$$IP = \sum_{x=1}^{N} |c_x|^4 \tag{4.14}$$

[3]The general formula is referred to 1D disordered systems with non-uniform hopping.

where N is the total number of sites and $1/N \leq IP \leq 1$. For completely extended eigenstates, such as in the case of the uniform CCA with cyclic boundary conditions, $IP = 1/N$ since the eigenfunction is evenly divided over the entire array. The opposite limit is reached by an eigenfunction whose $x-$representation is a $\delta-$Dirac centered on a given site. This is the case of the 1D Anderson Hamiltonian (4.1) with frequencies ω_x randomly selected from a generic distribution in the range $[-W, W]$ (for example an uniform, normal or Cauchy distribution) in the limit $W/J \gg 1$. As mentioned above, a disordered 1D system, described by a tight-binding-like Hamiltonian, shows Anderson localization for arbitrary disorder and its eigenstates will become the more localized the larger is the disorder strength W/J. Thus, in the limit $W/J \gg 1$, each of them shows a $\delta-$Dirac profile (each eigenstate being centered on a different site), indeed when $J \to 0$ the Anderson Hamiltonian (4.1) is diagonal in the $x-$representation and there is no longer photon hopping. In this case all eigenstates have $IP = 1$ and the corresponding eigenvalues coincide with the disordered mode-frequencies. The density of states of the disordered CCA can be obtained, for example, by numerical computation of the Green's function and by means of (4.13). In general, the dirorder removes the divergences at $E = \pm 2J$ of the uniform d.o.s., given in (2.60), and states with energy $|E| > 2J$ begin to appear.
In what follows we will use only normal distributions to simulate the disordered CCA, i.e. we consider the random frequencies ω_x distributed with gaussian probability density independent on the position (uncorrelated disorder), given by:

$$P(\omega) = \frac{1}{\sigma\sqrt{2\pi}} e^{-\frac{\omega^2}{2\sigma^2}} \tag{4.15}$$

where σ is the standard deviation for a given disorder realization and $< \omega_x >= 0$, i.e. the distribution is centered on the band center value of the uniform CCA. In general, for not too strong disorder, the resulting band of eigenvalues, as well as the density of states in the band central region, only deviates slightly from the corresponding quantities of a perfectly ordered array. In Fig (4.2) the disordered d.o.s., obtained by a numerical computation with $\sigma/J = 1$, is compared with the corresponding function (2.60) of the uniform CCA. They almost coincide around the band center, but the disordered d.o.s vanishes for large energies, showing two tails at $|E| > 2J$. Fig (4.3a) and (b) show the probabability-amplitude profiles for three eigenfunctions and the corresponding eigenvalues band obtained by numerical diagonalization of Hamiltonian (4.1) with $N = 200$ for two realizations of the gaussian disorder, characterized by standard deviations $\sigma = 0.1$ (a) and $\sigma = 1$ (b) in units of J. Several eigenmodes with eigenvalues near the edges of the band become exponentially localized in space with localization length smaller than the near band-center modes [70, 75], as shown in insets (1) and (2) of Fig (4.3a). For low enough disorder, the eigenfunctions near the band center remain almost extended inside the finite system [see Fig (4.3a), inset 3], i.e. they have $IP \approx 1/N$. These modes will be localized in an infinite system, but on a much larger length scale. As the disorder strength is increased, a larger fraction of the modes becomes localized within the finite array and for a given N, when σ/J is large enough, all eigenfunctions will show a localized profile within the N sites,

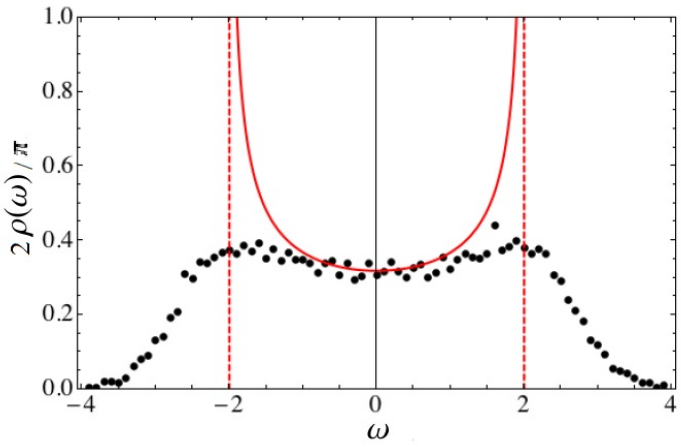

Figure 4.2: Numerical computation of the density of states for a disordered CCA with $\sigma/J = 1$ (black dots). The red line plots the corresponding d.o.s. of the uniform CCA, as given in (2.60), with $J = 1$ and corrected by a constant factor. From [80].

as shown in Fig (4.3b). As remarked above, they will be equally localized, each on a different site, with $IP \approx 1$ when $\sigma/J \gg 1$. We can justify this behaviour by means of (4.12) in which the asymptotic vanishing profile of the disordered d.o.s. must be considered. Alternatively, we can see that, for the state with maximum rescaled eigenvalue ϵ_M and N finite, the sum in (4.11) takes its maximum value, thus the localization length λ_M is minimum. Moreover, we can see that localized eigenfunctions near the top of the band are flat phased, i.e. their wave amplitude is in phase at all sites [see insets (2) of Fig (4.3a) and (b)]; while localized eigenmodes at the bottom of the band are staggered [cf. insets (1) of both figures], i.e. their wave function's amplitude has a π phase flip between adjacent sites. Notably, these localized eigenmodes are localized at well-separated regions in space and have a similar width.

4.1.2 TLS emission into the disordered-CCA environment

Now we focus on the atomic emission into the disordered CCA sketched in Fig (4.1), where we consider the atom coupled to the central cavity of the array. Here also we present numerical computations of both atomic probability and field evolution considering the initial atom-field state $|\Phi(0)\rangle = |e\rangle$. In order to describe the coupling between the TLS and the disordered CCA, we express the Anderson Hamiltonian (4.1) in the single excitation subspace. The coupling term in RW approximation is $\hat{H}_{ac}$, already introduced in (2.77). Thus, the total Hamiltonian in the $x-$representation reads:

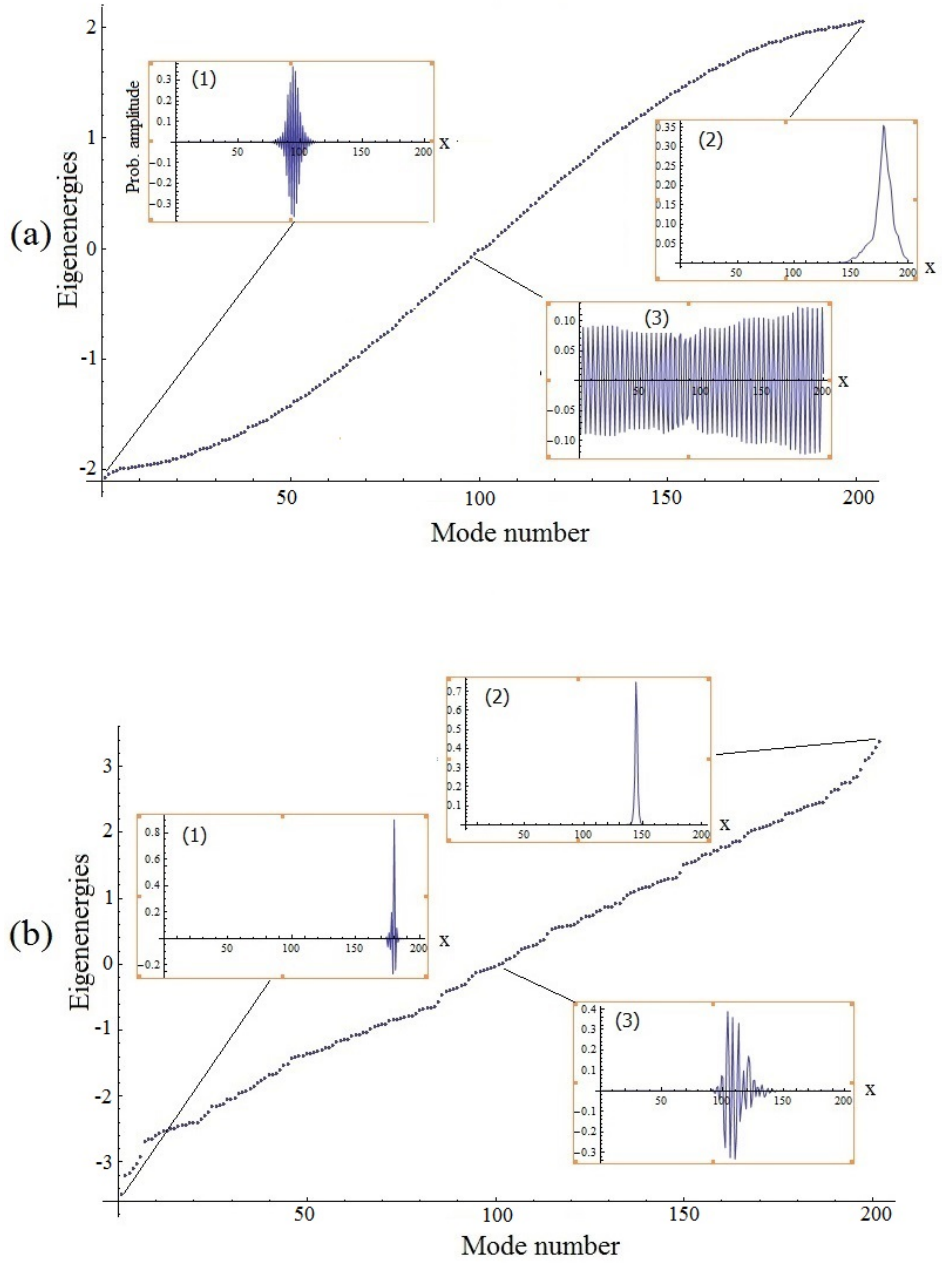

Figure 4.3: Eigenvalues band and $x-$amplitude profiles for three eigenstates obtained by numerical diagonalization of Hamiltonian (4.1) with $N = 200$ for two realizations of the gaussian disorder, characterized by standard deviations $\sigma = 0.1$ (a) and $\sigma = 1$ (b). The eigenergies are in units of J. The band still shows a cosine-shaped profile for weak disorder (a) but no more in (b), in which there are several eigenvalues external with respect the uniform-band limits $\pm 2J$. In each of the two figures, insets (1) and (2) relate, respectively, to the eigenstates with larger and smaller eigenvalue, while inset (3) relates to the band center eigenstate.

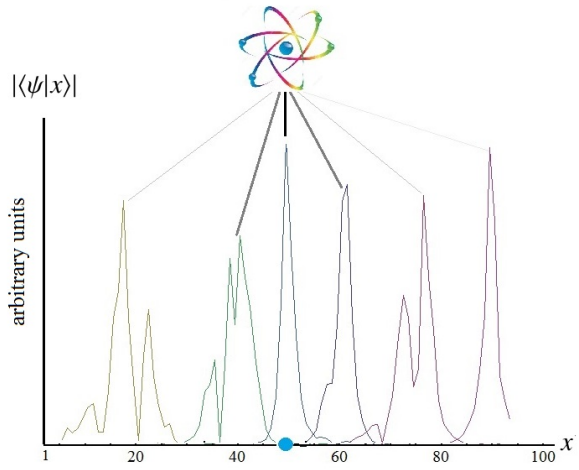

Figure 4.4: Simplified representation of the atomic coupling with a few of localized modes for a disordered 100-sites array. The atom interacts with six localized modes centered on different sites and the corresponding coupling constants are represented by the lines in greyscale. If the disorder srength is large enough, the modes localized around distant sites have a small overlap with the central atomic site, i.e. the corresponding coupling constants are small (grey thin lines). The atom is mainly coupled with the central mode and the corresponding coupling constant is the largest (black solid line).

$$\hat{H} = \sum_{x=1}^{N} \left[\omega_x |x\rangle\langle x| + J\left(|x\rangle\langle x+1| + h.c.\right)\right] + g\left(|x_0\rangle\langle e| + h.c.\right) \tag{4.16}$$

An $N-$sites (odd) array with open boundary conditions is considered and the atom is coupled to the central cavity in $x_0 = (N+1)/2$. As in the previous chapter, the energy scale adopted corresponds to $\omega_a = 0$. The cavity-frequencies ω_x are randomly generated with the gaussian PDF given in (4.15) centered on the atomic frequency and standard deviation σ. We are interested in the disorder-induced modifications of the atom-field dynamics when the bare uniform array behaves as an almost-Markovian reservoir of modes and we choose to study the atom-field dynmics in the strong-hopping regime with $g/J = 0.1$. In Sec. 3.2.1.1 we discussed the behaviour of a TLS decaying into a generic bath and we demonstrated that in strong-hopping regime the atom-photon bound states contributions to the dynamics can be neglected because only states with energies very close to the atomic one are involved in the atomic emission process.
As discussed above, although the 1D Anderson Hamiltonian admits only localized eigenstates, when the disorder strength is not too large, i.e. when σ/J is small enough, several eigenstates with energies near the band center are almost completely extended within the length of the finite array. The eigenstates of (4.16) have localization properties quite similar to the corresponding disordered bare-array ones, but they have also excitonic components. The analysis we want to lead is based on the fact that the x-profile of the eigenstates is not substantially modified by

the presence of the atom-field coupling term in (4.16), but only by the disorder-induced Anderson localization. We have to retrive, in the thermodynamic limit, the scattering states with $x-$amplitudes given in (2.99), excitonic components in (2.101) and the corresponding bound states (2.88) when $\sigma/J \to 0$. For strong enough disorder, as discussed in the case of the bare disordered CCA, the atom-CCA system admits only single-site localized eigenstates. Thus, in strong-hopping coupling and when $\sigma/J \gg 1$, only the eigenstate peaked on x_0 shows an excitonic component substantially different from zero. This can be easily demonstrated by considering perturbatively the Jaynes-Cummings coupling term in (4.16) and, by the knowledge of the unperturbed eigenstates (each of them with $IP \approx 1$, centered on a different site), the excitonic components can be obtained by expanding the eigenstates up to first order in g/J.
The CCA, in general, behaves as a particular bath of modes from the perspective of the atom. We have seen that the Fano-Anderson Hamiltonian (2.78) for an uniform array describes a bath of modes which the atom (site in the central position) is coupled to, with uniform coupling constant $g/\sqrt{N}$. Disorder, as well as other configurations of the atom-CCA [4], breaks the traslational invariance and, in general, a non-uniform dispersion of the coupling constants arise. We expect that the coupling of the atom with a generic eigenmode $|\psi_l\rangle$ of the disordered bare-CCA is proportional to $\langle\psi_l|x_0\rangle$, i.e. the atom is coupled with eigenmodes showing a large overlap with the cavity's site containing it. We can easily formalize this argument by expressing (4.16) into the basis of the eigenstates $|\psi_l\rangle$ of the Anderson Hamiltonian (4.1) that, in the single excitation subspace, corresponds to the first term of (4.16). So the atom-CCA Hamiltonian is rewritten as:

$$\hat{H} = \sum_l \left[\omega_l |\psi_l\rangle\langle\psi_l| + (g_l|\psi_l\rangle\langle e| + h.c.)\right] \quad with \quad g_l = g\langle\psi_l|x_0\rangle \tag{4.17}$$

where ω_l are the corresponding eigenvalues and g_l is the coupling constant between the atom and the l-th mode of the disordered CCA. For a given disorder realization $0 < g_l < g$ and, if σ/J is sufficiently large so that the CCA shows localized eigenmodes centered on different positions within the N sites, the coupling constant dispersion shows a well-shaped x-profile with maximum at $x = x_0$. Clearly this profile reflects how large is the amplitude of each eigenmode at the central site and, in the two limiting cases $\sigma = 0$ and $\sigma \gg J$, the coupling dispersion is, respectively, completely flat (i.e. $g_l = g/\sqrt{N}$ for each l, in presence of cyclic boundary conditions) and $g_l = g\delta(l - x_0)$ (for both open and cyclic boundary conditions). In the latter case, in which the only mode with nonvanishing x_0-amplitude is the central one and the eigenvalues ω_l coincide with the cavity random-frequencies ω_x, the atom interacts only with the central cavity and a detuned Jaynes-Cummings dynamics with coupling constant g and detuning $-\omega_{x_0}$ is found. So, if the atomic frequency ω_a (which we have chosen as the zero-frequency) can be adjusted, standard Vacuum Rabi oscillations at frequency $2g$ are found in the strong disordered system, by setting $\omega_a = \omega_{x_0}$. In general, when the disorder is not too strong, the atom exchanges energy with a given set of eigenmodes, depending on the coupling dispersion,

[4] For example, for an atom coupled to the x_s-th cavity of a semi-infinite uniform array, the coupling-constant dispersion is $g(k) \propto \sin(kx_s)$ [26].

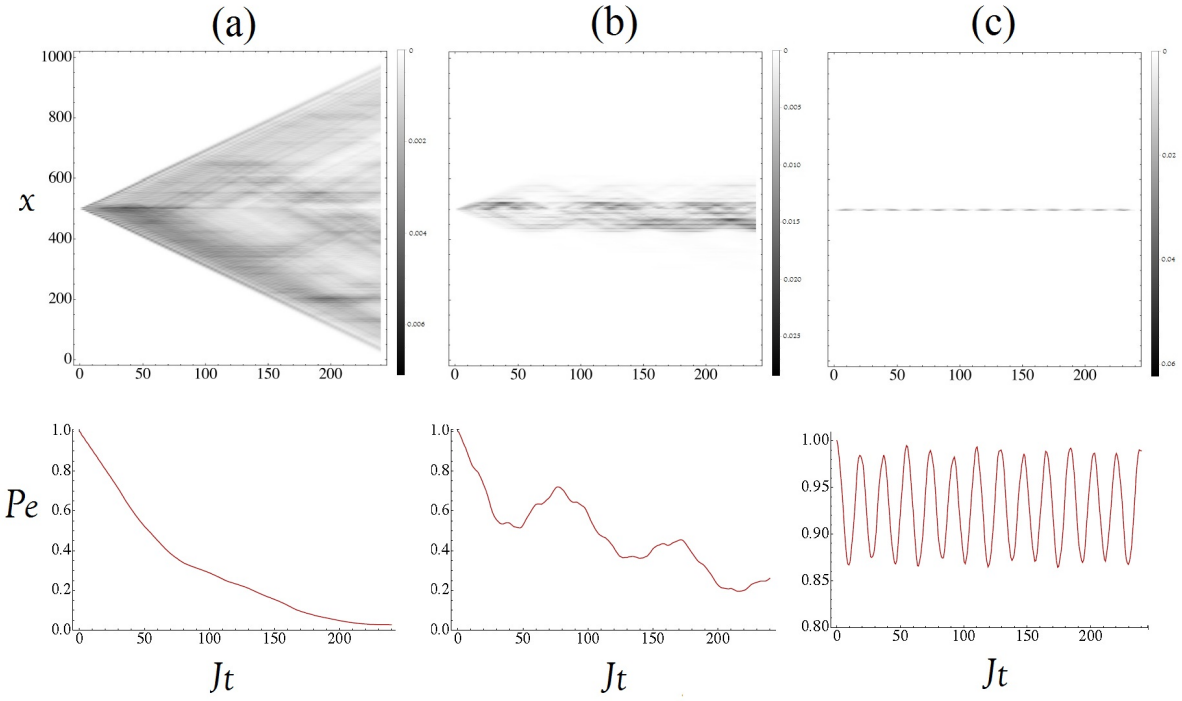

Figure 4.5: Space-time diagram of the photon probability distribution along the disordered array (top panels) for three realizations of the gaussian disorder obtained by numerical diagonalization of Hamiltonian (4.16) with $g/J = 0.1$ and $N = 1001$: $\sigma/J = 0.1$ (a), $\sigma/J = 0.5$ (b), $\sigma/J = 1.5$ (c). The bottom panels display the corresponding evolutions of the atomic probability $P_e(t)$.

i.e. on σ/J. In Fig(4.4) is depicted a simplified situation in which, for a 100-sites disordered array, the atom mainly interacts with six localized modes. The lines in greyscale represent the six corresponding coupling constants and the largest of these is represented by the black solid line which indicates the coupling with the central mode. In Fig (4.5) are shown three numerical simulations for the time evolution of the atomic excitation and photon probability distribution along an array of $N = 1001$ cavities, for different realizations of the gaussian disorder. The atom is coupled to the central cavity in strong-hopping regime, with $g/J = 0.1$. For small disorder, the dynamics, plotted in Fig (4.5a), is quite similar to the case of a TLS nearly resonant with the uniform CCA. In this case a major part of the eigenstates are completely extended within the N sites, i.e. almost each state shows a significant overlap with the central site, and the atom interacts with an almost flat spectral-density bath. Correspondingly the photon wave function spreads along the array [cf. Fig (3.5a)]. For large values of σ/J, Anderson localization takes place and the field does not propagate toward the external regions of the array and remains confined within the central region, as shown in Fig (4.5b). Qualitatively this can be easily justified. The main contributions to the photonic amplitude evolution at the generic x-th site arise from eigenstates which significantly overlap the x-th position. If σ/J is large enough, the system has only localized eigenstates and, when the distance $|x - x_0|$ exceeds a certain value, the atom will be significantly coupled only with eigenmodes for which $\langle\psi|x\rangle \approx 0$. In this way, the initial atomic excitation can't reach the x-th cavity or the more distant ones. Fig (4.5c) represents the strong-disorder case, for which the atom mainly interacts with the central cavity and, in this particular disorder realization, the x_0-cavity frequency is not close to the zero and a far-detuned Jaynes-Cummings interaction comes out.

4.2 Non-Markovian open quantum dynamics

In Chap 2 we have seen that, under certain conditions, the dynamics of a TLS interacting with a particular environment can be described by a quantum Markovian process. In Chap 3, by analyzing the TLS-CCA interaction in different coupling regimes, we found Markovian dynamics in the limiting case $g/J \to 0$ and referred to the strong-hopping dynamics (with non vanishing $g/J \ll 1$) as 'almost Markovian'.
The aim of this Section is to characterize, by means of a well-defined quantifier, the non-Markovianity of the process describing the interaction of a TLS with the disordered CCA, which we expect depends on the disorder strength. First some key concepts are introduced, in order to give a general, but non-exhaustive, characterization of the open quantum processes and to analyze the border between Markovian and non-Markovian dynamics.

4.2.1 Markovian processes and quantum dynamical maps

In classical probability theory and statistics a Markov process can be used to model a random system that changes states according to a transition rule that only depends on its current state. In other words, a process satisfies the so-called Markov property if one can make predictions for the future of the process based solely on its present state. In this sense it can be thought of as a 'memoryless' process [38]. We will see how the concept of Markovianity is expressed in the quantum case.
In Chap 1 we used the Linblad master equation to analyze the dynamics of a TLS decaying into a damped cavity. This approach was also used in Sec. 2.2.1 to introduce the spontaneous emission of a TLS. Master equations with a generator in the Linblad form describe a particular class of Markovian quantum processes. In the open quantum systems theory, a master equation of general form:

$$\frac{d}{dt}\rho_S(t) = \mathcal{L}(t)\rho_S(t) \tag{4.18}$$

can be used to describe the evolution of the system's reduced density matrix $\rho_S(t)$ interacting, by means of an Hamiltonian term H_I, with a given environment E. The dynamics of the total 'S+E' system, described by the Hamiltonian:

$$H = H_S + H_E + H_I \tag{4.19}$$

is closed, i.e. it is given by a unitary time evolution. In general, a time-dependent generator $\mathcal{L}(t)$ defines a master equation in the *time local* form (4.18) as a linear first-order differential equation for the open system state. It can be shown that, in order to preserve the Hermiticity and trace of the density matrix, this generator must be of the form [42, 43]:

$$\mathcal{L}(t)\rho_S(t) = -i\left[H_S(t), \rho_S\right] + \sum_k \gamma_k(t)\left[V_k\,\rho_S(t)\,V_k^\dagger - \frac{1}{2}\left\{V_k^\dagger V_k,\, \rho_S(t)\right\}\right] \tag{4.20}$$

where $H_S(t)$ and $V_k(t)$ are time-dependent operators, the former being self-adjoint and $\gamma_k(t)$ are the time-dependent decay rates. In some particular cases of Markovian evolution, the generator in (4.20) is defined by means of time-independent operators and positive time-independent rates, that corresponds to the Linblad master equation, example of which are given in (1.14) and (2.33). To better analyze this point and to give an exact definition of Markovian quantum processes, we introduce another key concept in the theory of open quantum systems: the *quantum dynamical map*, defined as follows:

$$\varepsilon(t_2, t_1)\rho_S(t_1) = \rho_S(t_2) \qquad t_2 \geq t_1 \tag{4.21}$$

i.e. $\varepsilon(t_2, t_1)$ maps any open system state at time t_1 to the corresponding open system state at time $t_2 \geq t_1$. Open quantum dynamics can be described by means of such a map if it satisfies certain conditions: ε must be linear, trace-preserving and it must be also completely positive[5] [43, 46]. Considering the map $\varepsilon(t, 0)$ as a smooth time-dependent function, differentiating (4.21) with $t_2 = t$ and $t_1 = 0$, the corresponding linear generator of the master equation [6] is easily obtained:

$$\mathcal{L}(t) = \varepsilon^{-1}(t, 0)\frac{d}{dt}\varepsilon(t, 0) \tag{4.22}$$

in which we have assumed that the inverse $\varepsilon^{-1}(t, 0)$ of the map $\varepsilon(t, 0)$ does exist or, in other words, we have assumed the differentiability of the map in a such a way that:

$$\lim_{\tau \to 0} \frac{\varepsilon(t + \tau, t) - I}{\tau} := \mathcal{L}(t) \tag{4.23}$$

is well-defined at any time. Not all quantum processes are defined by means of differentiable maps. In some cases, e.g. for very strong system-environment couplings, the inverse of the map and, hence, also the time local generator $\mathcal{L}(t)$ does not exist. However, it is possible to demonstrate that, for an analytic time-dependence, $\varepsilon^{-1}(t, 0)$ [7] and $\mathcal{L}(t)$ do exist apart from isolated singularities of the time axis [43]. By means of these considerations we can define a quantum process as Markovian if it is defined by means of a linear, completely-positive trace-preserving map (CPT) which satisfies the following condition:

$$\varepsilon(t + \tau, 0) = \varepsilon(t + \tau, t)\varepsilon(\tau, 0) \qquad \forall t, \tau \geq 0 \tag{4.24}$$

i.e. if $\forall t, \tau \geq 0$ the CPT map $\varepsilon(t + \tau, 0)$ can be written as a product of the two CPT maps $\varepsilon(t + \tau, t)$ and $\varepsilon(\tau, 0)$. This condition is known as *divisibility* of the map. Hence, *all divisible CPT maps describe Markovian prcesses*. There are many quantum processes which are not divisible. For instance if $\varepsilon(t, 0)$ is not invertible, a linear map $\varepsilon(t + \tau, t)$ which fulfills (4.24) may not exist [48]. Moreover, it can be demonstrated that a CPT map is divisible if and only if the corresponding generator can be written in the form (4.20) with $\gamma_k(t) \geq 0$ [8] [46].

[5] A linear map $\mathcal{M}$ acting on a matrix space $\mathcal{S}$ is positive if it transorms positive semidefinite matrices into positive semidefinite matricies. In addition, $\mathcal{M}$ is said to be completely positive if for any matrix space $\mathcal{S}'$ such that $dim(\mathcal{S}') \geq dim(\mathcal{S})$, and $\rho' \in \mathcal{S}'$, $\rho' \geq 0 \Rightarrow \mathcal{M} \otimes I(\rho') \geq 0$. Not all quantum process are described by completely positive maps. Due, e.g., to the presence of initial system-environment correlations, only positive maps are involved [57]. Complete positive maps are much easier to characterize than maps that are merely positive [46].

[6] There exists a powerful method for the microscopic derivation of time-local master equations of the form (4.18) which is known as time-convolutionless projection operator technique [42]. This technique yields a systematic expansion of the generator of the master equation in terms of ordered cumulants.

[7] The inverse of the map is not required to be completely positive. In general, it is not only not completely positive, but even not positive.

[8] This theorem is a consequence of the famous *Gorini-Kossakowski-Sudarshan-Lindblad* theorem. The authors (A. Kossakowski and co-workers and, indepentently, G. Lindblad) analyzed the case of a time-homogeneous equation, i.e. a time-independent generator $\mathcal{L}(t) = \mathcal{L}$ that they discovered to be the generator of a semigroup of

Thus, *a quantum process is Markovian if and only if it can be described by a time-local master equation of the form (4.20) with non-negative rates.* So the Linblad master equation, that is the particular case of (4.20) with time-independent operators and non-negative time-independent rates, descibes a restricted class of Markovian processes. Such processes belong to the *dynamical semigroup* of CPT maps [40, 41], i.e. their time-independent generator $\mathcal{L}$ is defined as:

$$\varepsilon(t,0) = e^{\mathcal{L}t} \tag{4.25}$$

from which trivially descends the divisibility condition (4.24). Here we don't give a proof of the theorem just stated, but it can be seen that if the dynamical map $\varepsilon(t,0)$ is divisible with a unique map $\varepsilon(t+\tau,t)$ depending smoothly on τ, we can use (4.23) to obtain the generator $\mathcal{L}(t)$. Since $\varepsilon(t+\tau,t)$ is CPT and satisfies $\varepsilon(t,t) = I$, the corresponding generator will preserve the Hermicity and the trace of the density matrix and it must be in Linblad form for each fixed t, that is, it must have the form (4.20) with $\gamma_k(t) \geq 0$ [48].
It is in general not trivial to derive a Linblad master equation starting from a given system-environment model with a microscopic Hamiltonian of the form (4.19). Such a derivation requires the validity of several approximations, the most important one being the so-called Markov approximation. This approximation presupposes a rapid decay of the two-point correlation functions of those environmental operators that describe the system-environment coupling H_I. More precisely, if τ_E describes the time scale of these correlations and τ_R the relaxation or decoherence time of the system, the Markov approximation demands that:

$$\tau_E \ll \tau_R \tag{4.26}$$

which implies that the environmental correlations decay on a time scale much faster than the open system's relaxation or decoherence time, i.e. the system's dynamics is characterized by variables with two very different time scales, the environmental variables being fast and the system ones being slow [43]. The Markov approximation is justified in many cases of physical interest. Typical examples are the weak coupling optical master equations describing the interaction of radiation with matter, as those we discussed in Chap 1 and 2. When deriving the evolution equations for an open quantum systems from microscopic models, the adjective 'Markovian' is widely used to design master equations obtained under the so-called 'Born-Markov' approximation. More concretely, the Born approximation truncates the perturbative expansion of $\rho_S(t)$ in the interaction Hamiltonian $H_I = \sum_i S_i \otimes E_i$ (where the operators S_i (E_i) are defined in the system's (environment's) Hilbert space), at first non-trivial order. This leads to some differential equation of the form [42, 46]:

completely positive quantum dynamical maps if and only if it has the well-known Linblad form [40].

$$\frac{d}{dt}\rho_S(t) = -i\left[H_S(t), \rho_S\right] + \sum_{i,j} \Omega_{ij}(t)\rho_S(t)S_j + S_j\rho_S(t)\Omega_{ij}^{\dagger}(t) - S_j\Omega_{ij}(t)\rho_S(t) - \rho_S(t)\Omega_{ij}^{\dagger}S_j \quad (4.27)$$

where

$$\Omega_{ij}(t) = \int_0^t ds\, C_{ij}(s)e^{-iH_S s}S_i e^{iH_S s} \quad with \quad C_{ij}(s) = Tr\left[E_j e^{-iH_E s}E_i e^{iH_E s}\rho_E\right] \quad (4.28)$$

C_{ij} are the correlation functions of the environment, which is in the state ρ_E and has free Hamiltonian H_E. If these correlations are narrow in time, i.e. if the condition (4.26) is fulfilled, the upper limit in the integral in (4.28) can be extended to infinity and, more rigorously, this defines the Markov approximation. Despite the fact that the 'Born-Markov' approximation leads to master equations with time-independent coefficients, they do not always define a valid quantum dynamical semigroup because they break the completely positivity. Thus, these models should not be referred as 'Markovian' in strict sense. If the 'Born-Markov' approximation is combined with a secular approximation (i.e. neglecting fast oscillating terms in the evolution equation, as the RW approximation described in Chap 1, that we adopt for all models here described) a valid quantum dynamical semigroup is obtained, and then the dynamics can be certainly called Markovian.
Condition (4.26) is characteristic of a memoryless environment. This can be viewed better if we consider a simple collisional model describing the system-environment interaction [46]. In this model, the interaction between system and environment is made up of a sequence of individual collisions at times $t_1, t_2, ...t_n$. Each collision produces a change in the state of the system ρ_S given by:

$$\rho_S(t_{n+1}) = Tr_E\left[U(t_{n+1}, t_n)\rho_S \otimes \rho_E U^{\dagger}(t_{n+1}, t_n)\right] = \varepsilon(t_{n+1}, t_n)\,\rho_S(t_n) \quad (4.29)$$

where ρ_E is the state of the environment assumed to be the same for every collision, and $U(t_{n+1}, t_n)$ is the unitary operator, describing the system-environment interaction, associated with the total Hamiltonian (4.19) of the closed 'S+E' system. The system's state ρ_S is obtained by tracing over the environmental states. The successive concatenations of these collisions lead to a quantum Markovian process. Indeed, from (4.29), it is straightforward to see that $\varepsilon(t_{n+2}, t_n) = \varepsilon(t_{n+2}, t_{n+1})\varepsilon(t_{n+1}, t_n)$ and since ε is a CPT map, the process is Markovian. At every time t_n the system interacts with the environmental state ρ_E via the unitary operation U. At the following time step t_{n+1}, the system finds again the environment in the same state ρ_E, forgetting any correlation caused by the previous interaction at t_n. Provided the limit $max_n|t_{n+1} - t_n| \to 0$, is well-defined, this process can be seen as a discrete version of quantum Markovian dynamics. Hence, Markovian evolutions may be thought as made up of a sequence of memoryless collisions, where the environmental state is the same and the total state of system and environment is

uncorrelated at each collision as if there were no previous interaction. Notably, any Markovian dynamics can be seen as a collisional model like this. Indeed, it can be demonstrated that a completely positive dynamics described by the map ε can be seen as the reduced dynamics of some unitary evolution acting on an extended state with the form $\rho_S \otimes \rho_E$ where ρ_E is the same independently of ρ_S [39]. Thus, since for Markovian evolutions a CPT map $\varepsilon(t_2, t_1)$ exists for all $t_2 \geq t_1$, we may write it[9] as:

$$\varepsilon(t_2, t_1)(\cdot) = Tr_E \left[U(t_2, t_1)(\cdot) \otimes \rho_E U^\dagger(t_2, t_1) \right] \tag{4.30}$$

where $U(t_2, t_1)$ may depend on t_2 and t_1 but ρ_E can be taken to be independent of time. This does not mean that we must impose system and environment to be uncorrelated at any time to get Markovian evolutions. Rather, the conclusion is that the obtained evolution may also be thought as the result of memoryless system-environment infinitesimal collisions, characterized by very fast decaying correlations fulfilling the conditions $\tau_E \ll t_{n+1} - t_n$ and (4.26).

4.2.2 Non-markovian quantum processes and information flow

In the case of deviations from the dynamics of a quantum Markov process one speaks of a non-Markovian process, implying that the dynamics is characterized by significant memory effects. Non-Markovian memory effects are typically significant for structured environments in the strong system-environment coupling regime. Various concepts of non-Markovianity were introduced recently to define the border between Markovian and non-Markovian quantum evolution. In order to quantify this concept, the so-called *measures of non-Markovianity* are introduced. Basically, each such a measures is a function which assigns a number (positive or zero) to each dynamics, in such a way that the zero value is obtained if and only if the dynamics is Markovian. Each measure must be formulated completely by means of the quantum dynamical map of the process. Quantum master equations with the time-local structures given by (4.18) and (4.20) are very useful for also the description of non-Markovian processes. It follows from the preceding discussion that in order for such a master equation to yield a nonzero measure, at least one of the rates $\gamma_k(t)$ must take on negative values for some interval of time. Moreover, it can be demostrated that temporarily negative rates in the master equation in general do not lead to a violation of the complete positivity of the dynamical map.
Many different measures of non-Markovianity have been proposed in the literature to quantify memory effects in open systems, based on, for examples, the divisibility of dynamical map [44, 45, 46], the distinguishability of states [47, 48, 49], quantum entanglement [51], quantum Fisher information [52], mutual information [53], geometrical characterization [56], the decay rate of the master equation itself [54] and two time correlation functions [55].

[9] This CPT map can be expressed by means of a Krauss sum, i.e. $\varepsilon(t_{n+1}, t_n)(\cdot) = \sum_{i,j} K_{ij}(\cdot)K_{ij}^\dagger$. The Krauss operators are given by $K_{ij} = \sqrt{p_j^E}\langle\phi_i^E|U(t_{n+1}, t_n)|\phi_j^E\rangle$, for $\rho_E = \sum_j p_j^E |\phi_j^E\rangle\langle\phi_j^E|$ [81].

Here we first show the explicit expression for the dynamical amplitude-damping map which describes the decay of a TLS into a generic bosonic reservoir initially in the vacuum state, with general Hamiltonian in rotating wave approximation given in (1.1) or (2.29). In this way we can define the exact border between Markovian and non-Markovian behaviour for such a general dynamics[10]. Shortly after, we give a brief description of the BLP measure of non-Markovianity [47, 48], a recent approach which defines and quantifies the emergence of quantum memory effects in terms of the exchange of information between the open system and its environment. In the next section we discuss in detail the geometrical measure due to S. Lorenzo, F. Plastina and M. Paternostro [56] which we will adopt in Sec. 4.2.4 to characterize the non-Markovian dynamics of a TLS decaying into the disordered CCA.
The model which we used to describe the coupling of a TLS to a reservoir of electromagnetic field-modes, labelled by the index k, with corresponding frequencies ω_k, coupling constant g_k and Hamiltonian in RW approximation conserves the total number of excitations, therfore it allows to derive an analytical expression for the dynamical map (4.21). This map can be represented in terms of the system's density matrix elements $\rho_{i,j}(t) = \langle i|\rho(t)|j\rangle$ (we omit the subscript 'S'), with $i, j = \{e, g\}$ as follows:

$$\begin{aligned} \rho_{ee}(t) &= |\Gamma(t)|^2\rho_{ee}(0), \\ \rho_{gg}(t) &= \rho_{gg}(0) + [1 - |\Gamma(t)|^2]\rho_{ee}(0), \\ \rho_{eg}(t) &= \rho^*_{ge}(t) = \Gamma(t)\rho_{eg}(0) \end{aligned} \tag{4.31}$$

where the function $\Gamma(t)$ was introduced in (3.22) as the solution of the integro-differential equation:

$$\frac{d}{dt}\Gamma(t) = -\int_0^t dt'\zeta(t-t')\Gamma(t') \tag{4.32}$$

corresponding to the initial condition $\Gamma(0) = 1$. This equation can be derived by imposing the Schrödinger equation for the probability amplitudes $\{\alpha_k(t)\}, \alpha_e(t)$ of the atom-bath system with no photons in the initial state (i.e. $\{\alpha_k(0)\} = 0$), in the interaction picture with respect H^{coup} in (2.29)[11]. The atomic probability amplitude is thus:

$$\alpha_e(t) = \alpha_e(0)\Gamma(t) \tag{4.33}$$

and the kernel $\zeta(t - t')$ is the two-time correlation function of the reservoir [42] and reads:

[10] A more detailed analysis which employees both master equation in Born-Markov approximation and the time-convolutionless approach can be found in Ref [42].

[11] This procedure was already used in the classic paper by Weisskopf and Wigner (1930) on the determination of the natural line width.

$$\zeta(t-t') = \sum_{k,k'} g_k g_{k'} \langle 0|a_k\, a_{k'} e^{i(\omega_{k'}-\omega_k)(t-t')}|0\rangle e^{i\omega_a(t-t')} = \sum_k |g_k|^2 e^{i(\omega_a-\omega_k)(t-t')} \tag{4.34}$$

where the coupling consants are considered real without loss of generality and the bosonic commutation relations have been taken into account. The generic bath of modes is characterized by a spectral density whose Fourier transform is $\zeta(\tau)$. The map defined by (4.31) is completely positive if and only if $|\Gamma(t)| \leq 1$. Moreover, by calculating the matrix elements of ρ at time $t+\tau$, we can check the divisibility condition (4.24):

$$\begin{aligned}
\rho_{ee}(t+\tau) &= \left|\frac{\Gamma(t+\tau)}{\Gamma(t)}\right|^2 \rho_{ee}(t), \\
\rho_{gg}(t+\tau) &= \rho_{gg}(t) + \left[1 - \left|\frac{\Gamma(t+\tau)}{\Gamma(t)}\right|^2\right]\rho_{ee}(t), \\
\rho_{eg}(t+\tau) &= \rho^*_{ge}(t+\tau) = \frac{\Gamma(t+\tau)}{\Gamma(t)}\rho_{eg}(t)
\end{aligned} \tag{4.35}$$

from which it follows that the corresponding $\varepsilon(t+\tau)$ is a CPT map if and only if $|\Gamma(t+\tau)| \leq |\Gamma(t)|$, i.e. the dynamical map of the model is divisible and the process is Markovian if and only if $|\Gamma(t)|$ is a monotonically decreasing function of time. This statement holds true also for the case in which $\Gamma(t)$ vanishes at some finite time. The corresponding time-local master equation can be written by introducing the following quantities:

$$\gamma(t) = -2\Re e\left(\frac{\dot\Gamma(t)}{\Gamma(t)}\right) = -\frac{2}{|\Gamma(t)|}\frac{d}{dt}|\Gamma(t)|, \qquad S(t) = -2\Im m\left(\frac{\dot\Gamma(t)}{\Gamma(t)}\right) \tag{4.36}$$

and the exact master equation for the reduced system dynamics in the form (4.20) reads [42]:

$$\frac{d}{dt}\rho(t) = -\frac{i}{2}S(t)[\sigma_+\,\sigma_-, \rho(t)] + \gamma(t)\left[\sigma_-\,\rho(t)\,\sigma_+ - \frac{1}{2}\sigma_+\,\sigma_-\rho(t) - \frac{1}{2}\rho(t)\sigma_+\,\sigma_-\right] \tag{4.37}$$

where $S(t)$ plays the role of a time-dependent Lamb shift. From (4.36) we can see that if at some time $|\Gamma(t)|$ is an increasing function, hence the divisibility of the map is broken, correspondingly the rate $\gamma(t)$ takes negative values. Thus, for the present model, a non-Markovian dynamics is equivalent to the nondivisibility of the dynamical map and to the occurrence of a negative rate in the master equation. From these consideration we can deduce that *the dynamics characterizing a TLS decaying into the uniform CCA is always non-Markovian.* Indeed, the bound-states contribution $\alpha_b(t)$ to the atomic probability amplitude, given in (3.13) for the resonant case, is an oscillatory term for any finite coupling constant g/J (and for any atom-cavity detuning), thus,

from (4.33), we deduce that, for this system, $|\Gamma(t)|$ is not a monothonic decreasing function. Due to the presence of such an oscillatory term, the corresponding map is not divisible ad the master equation takes periodically negative rates. For this reson we indicated as 'almost-Markovian' the dynamics of the system in the strong-hopping limit.
Recently Breuer, Laine and Pilo (BLP) proposed a definition of non-Markovian dynamics in terms of the behavior of the trace distance [47, 48]. They state that a quantum evolution, given by some dynamical map, is Markovian if the trace distance between any two initial states ρ_1 and ρ_2 decreases monotonically with time. The trace distance describes the probability of successfully distinguish two quantum states and the change in their trace distance can be interpreted as a flow of information between the system and the environment. It is defined as follows:

$$\mathcal{D}(\rho_1, \rho_2) = \frac{1}{2} Tr|\rho_1 - \rho_2| \quad with \quad |\rho| = \sqrt{\rho^\dagger \rho} \tag{4.38}$$

and it satisfies $0 \leq \mathcal{D} \leq 1$. For a TLS or a qubit, ρ is a 2×2 matrix which can be expressed in the Bloch form, i.e. :

$$\rho = \sum_{i=0}^{3} Tr[\rho\sigma_i]\sigma_i \equiv \sum_{i=0}^{3} r_i\sigma_i \tag{4.39}$$

with $\sigma_0 = I/\sqrt{2}$ and $\sigma_{1,2,3}$ are, respectively, the Pauli's matricies $\sigma_{x,y,z}$ and

$$r_i = Tr[\rho\sigma_i] \tag{4.40}$$

are the components of a four-dimensional vector $\vec{r} = (1/\sqrt{N}, \mathbf{r})$. Here $\mathbf{r} \equiv (r_1, r_2, r_3) \equiv (r_x, r_y, r_z)$ is the Bloch vector associated with ρ. In the two-dimensional Hilbert space we have $2\mathcal{D}(\rho_1, \rho_2) = |\mathbf{r}_1 - \mathbf{r}_2|$, i.e. the trace distance between two states is half of the Euclidean distance, on the Bloch sphere, between their corresponding Bloch vectors. It is preserved under unitary evolution, i.e. the information is preserved under the dynamics of closed systems, and all CPT maps are contractions for this metric, i.e. $\mathcal{D}(\varepsilon\rho_1, \varepsilon\rho_2) \leq \mathcal{D}(\rho_1, \rho_2)$. The change in the distinguishability of states of an open system can be interpreted as a flow of information between the system and the environment and the contraction property guarantees that the maximal amount of information the system can recover from the environment is the amount of information that previously flowed out the system. For a given Markovian process, described by a CPT divisible map, the trace distance between a pair of initial states is monotonically reduced and this can be seen as an unidirectional information flow between the system and the environment. This process will eventually lead the initial pair of states to coincide, i.e. their distinguishability is monotonically reduced to zero. If, on the other hand, the process is non-Markovian the trace distance between ρ_1 and ρ_2 does not show such a monotonic behaviour and there must be, for some interval of time, an increase of $\mathcal{D}(\rho_1, \rho_2)$, corresponding to the information back-flow. The information flowing from the environment back to the system allows the earlier

states of the system to have an effect on the later dynamics of the system; that is, it allows the emergence of memory effects. By means of these considerations, BLP defined the measure of non-Markovianity [48] as follows:

$$\mathcal{N}_T = \max_{\rho_{1,2}(0)} \sum_i \left[\mathcal{D}(\rho_1(b_i), \rho_2(b_i)) - \mathcal{D}(\rho_1(a_i), \rho_2(a_i))\right] \tag{4.41}$$

To calculate this quantity, one first determines for a given set of pair of initial states the total growth of the trace distance over each time interval $[a_i, b_i]$ for which $\partial_t[\mathcal{D}(\rho_1(t), \rho_2(t))] \geq 0$. This has to be maximized over the optimal initial pairs of states that, for 2×2 density matricies, are always antipodal points on the Bloch sphere [50]. Clearly $\mathcal{N}_T = 0$ for all Markovian processes.

4.2.3 Geometrical measure of non-Markovianity

In Ref [56] is described a non-Markovianity measure based on the change in volume of the set of accessible states of the evolving system[12]. Also this approach provides a measure for the non-Markovianity that is a characteristic of the map itself and does not depend on the initial state of the system. As a result, if the optimized trace distance decreases monotonically, so does the volume, which is however much easier to evaluate through the determinant of the dynamical map.
For a given CPT map $\varepsilon(t, 0)$, using the same definitions given in (4.39) and (4.40), the corresponding map for the Bloch vector can be written as:

$$\vec{r}(t) = \mathcal{F}(t)\,\vec{r}(0) \quad with \quad \mathcal{F}_{ij} = Tr\left[\sigma_i\,\varepsilon(t, 0)[\sigma_j]\right] \tag{4.42}$$

As $\mathcal{F}_{0j} = \delta_{0j}$, this is an affine transformation for the Bloch vector. Letting $q_i(t) = \mathcal{F}_{i0}$, the map $\mathcal{F}(t)$ reads:

$$\mathcal{F}(t) = \begin{bmatrix} 1 & 0 \\ \mathbf{q}(t) & \mathcal{A}(t) \end{bmatrix} \rightarrow \mathbf{r}(t) = \mathcal{A}(t)\mathbf{r}(0) + \mathbf{q}(t)/\sqrt{2} \tag{4.43}$$

It is straightforward to prove that the matricies $\mathcal{F}(t)$ and $\mathcal{A}(t)$ have the same determinant, i.e. $\|\mathcal{F}(t)\| = \|\mathcal{A}(t)\|$. The action of $\mathcal{F}$ is given by a rotation (possibly composed with an inversion), a shrink of the Bloch vector, and a final rotation with possibly a translation. The set of physical Bloch vectors for a TLS is given by [58]:

$$B_2 = \{\mathbf{r} \equiv (r_x, r_y, r_z) : (-1)^j h_j(\mathbf{r}) \geq 0 \ (j = 1, 2)\} \tag{4.44}$$

[12]This method is quite general and allows to deal with systems with both finite and infinite dimensional Hilbert space.

where $h_j(\mathbf{r})$ are the coefficients of the characteristic polynomial $det\,(xI - \rho)$. Hence, if $V(t)$ is the volume, within the Bloch sphere ($V \leq 1$), consisting of the set of evolved Bloch vectors at time t, we have:

$$\|\mathcal{A}(t)\| = \frac{V(t)}{V(0)} \tag{4.45}$$

Thus, the determinant of $\mathcal{A}(t)$ gives the contraction factor of the volume of accessible states with respect to its value at $t = 0$. For a given Markovian process, the accessible-states volume decreases monothonically during the evolution. Similarly to the trace distance characterization, a process is non-Markovian if, for some interval of time, $\partial_t \|\mathcal{A}(t)\| > 0$. This leads to define the following non-Markovianity measure:

$$\mathcal{N}_V = \frac{1}{V(0)} \int_{\partial_t V(t)>0} \partial_t V(t) = \int_{\partial_t \|\mathcal{A}(t)\|>0} \partial_t \|\mathcal{A}(t)\| \tag{4.46}$$

For the amplitude-damping map of a TLS in a generic reservoir of field-modes, defined in (4.31), the evolution of the Bloch vector is:

$$\mathcal{A}(t) = \begin{bmatrix} \Re e\Gamma(t) & \Im m\Gamma(t) & 0 \\ -\Im m\Gamma(t) & \Re e\Gamma(t) & 0 \\ 0 & 0 & |\Gamma(t)|^2 \end{bmatrix} \quad \Rightarrow \quad \|\mathcal{A}(t)\| = |\Gamma(t)|^4 = \left|\frac{\alpha_e(t)}{\alpha_e(0)}\right|^4 \tag{4.47}$$

Hence, in this case of atom-reservoir coupling with Hamiltonian (2.29), the variation of the volume of accessible states is given by the fourth power of the absolute value of the atomic probability amplitude with the initial condition $\alpha_e(0) = 1$.

We have analyzed in Chap 2 the atomic emission into a reservoir consisting of a damped cavity which is equivalent to a structured environment with a lorentzian d.o.s., as defined by (2.42). The corresponding atomic probability evolution $P_e(t)$ at resonance, for a given coupling constant g and photon loss rate k, is given in (2.48). Fig(4.6a) shows the time evolution of the determinant $\|\mathcal{A}(t)\| = P_e^2(t)$ in the coupling regime with $g < k/4$ for which it is a monotonic decreasing function of time. The corresponding Markovian decrease of the volume of accessible states is also shown. On the other hand, for $g > k/4$ in (2.48), one has a non-monotonic behaviour of $\|\mathcal{A}(t)\|$ and, as shown in Fig(4.6b), the corresponding non-Markovian dynamics is characterized by a non-monotonic evolution of the accesible volume. In this last case, since the derivative of $\|\mathcal{A}(t)\|$ takes periodically positive values, the measure $\mathcal{N}_V$ defined in (4.46) takes a nonvanishing value that is the higher the larger is g/k and, in the case of perfect lossless cavity ($k = 0$), it diverges.

The geometrical measure of non-Markovianity, similarly to the trace-distance based measure, can be linked to the change of the classical information encoded in the states of a system. If we indicate with $w(\mathbf{r})$ the probability density associated with an arbitrary distribution of the Bloch vectors within the space B_2 defined in (4.44), the corresponding differential entropy is

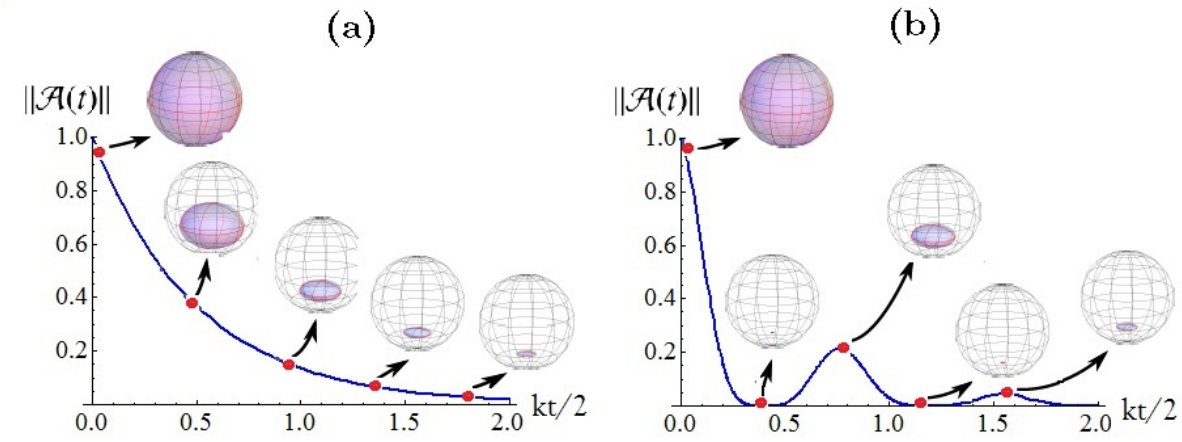

Figure 4.6: Time evolution of the determinant of the amplitude-damping map defined in (4.47) for Markovian (a) and non-Markovian dynamics (b). Quantitatively, the curves displayed in the figure correspond to the spontaneous emission of a TLS in a resonant leaky cavity with the Lorentzian d.o.s given in (2.42) and coupling/damping ratio given by $g/k = 0.2$ (a) and $g/k = 2$ (b). The set of accessible states, whose volume changes in time according to the behavior of the determinant, is also pictured.

$\mathcal{S}[w(\mathbf{r})] = -\int_{B_2} w(\mathbf{r}) \log_2 w(\mathbf{r}) dV$. If the states are evolved through the map (4.43), after a time t^* the probability density function is rescaled as $w'(\mathbf{r}(t^*)) = w(\mathbf{r}(t^*))/\|\mathcal{A}(t^*)\|$ and the entropy changes as $\mathcal{S}[w'(\mathbf{r}(t^*))] - \mathcal{S}[w(\mathbf{r}(0))] = \log_2 \|\mathcal{A}(t^*)\|$. In this way a contraction of the accessible volume implies a loss of information.

4.2.4 Non-Markovianity measures for the TLS-CCA quantum evolution in presence of static disorder

We have seen that the atomic emission into the uniform CCA is a non-Markovian process for any finite g/J. Due to the presence of the oscillatory bound-states contribution $\alpha_b(t)$ given in (3.13), the geometrical measure of non-Markovianity defined in (4.46) for such a system is divergent. This occurs for a generic system, whose evolution is described by the amplitude-damping map (4.47), which shows population trapping. In order to analyze the non-Markovianity of the quantum process which describe the coupling between a TLS and the disordered CCA, we define the following modified version of the geometrical measure $\mathcal{N}_V$:

$$\mathcal{N}_{Vr} = \frac{\int_{\partial_t \|\mathcal{A}(t)\|>0}^{t_{max}} \partial_t \|\mathcal{A}(t)\|}{\int_{\partial_t \|\mathcal{A}(t)\|<0}^{t_{max}} \partial_t \|\mathcal{A}(t)\|} \tag{4.48}$$

where, from (4.47), $\|\mathcal{A}(t)\| = P_e^2(t)$. Here the integrals of $\partial_t \|\mathcal{A}(t)\|$ are not calculated over the entire dynamics but up to a conveniently choosen time t_{max}. This definition is adopted because we compute the system's evolution, hence the non-Markovianity measure, by means of numerical simulations. The measure $\mathcal{N}_{Vr}$ quantifies the ratio between the total increase of the volume of accessible states and the corresponding decrease up to $t = t_{max}$, i.e. the ratio between the information which the TLS loses into the disordered-CCA's environment and the corresponding back-flow. For a finite-dynamics analysis of a system characterized by population trapping, the ratio between these two integrals provides a better way to quantify the non-Markovianity of the process with respect to the integral (4.46) calculated up to $t = t_{max}$. From the discussion of Sec.4.1.2 we know that the set of eigenmodes of the disordered CCA significantly involved in the atomic dynamics depends largely on the disorder strength. Here we study the non-Markovianity for the process of a TLS interacting with the disordered CCA by numerical computations of $\mathcal{N}_{Vr}$ for different standard deviations of the gaussian disorder. The simulations are performed for an array of $N = 1001$ cavities, the central one containing the atom which is coupled to, with $g/J = 0.1$. The measure $\mathcal{N}_{Vr}$ is averaged, for each standard deviation σ of the disorder, over 10000 realizations of the disordered array. Open boundary conditions are considered and the maximum time is chosen at $t_{max} = 240/J$ for each computational run, i.e. the time for which, in the uniform case, the photonic excitation has almost reached the borders of the array. The measure of non-Markovianity is compared with a representative quantity of the bare-array with a given disorder strength, also averaged over 10000 realizations with a given σ, that is the localization length (λ_0) of a given selected eigenstate. More specifically, for each disorder realization, we choose the eigenmode which provides the largest contribution to the atomic evolution. With reference to (4.17), out of the entire set of eigenmodes $\{|\psi_l\rangle\}$ of the bare disordered CCA, with corresponding eigenvalues ω_l, we select the eigenstate $|\psi^0\rangle$ for which the ratio $|\langle\psi_l|x_0\rangle/\omega_l|$ is maximum, i.e. out of the states which significantly overlap the central-cavity site $|x_0\rangle$, we choose the less detuned one. The corresponding eigenvalue is labeled as ω_0. As we will discuss below, the localization length of $|\psi^0\rangle$ can be considered proportional to the volume of an effective cavity coupled with the atom. For each disorder realization, $|\psi^0\rangle$ is an eigenstate of the bare CCA and the corresponding measure of non-Markovianity is clearly performed on the TLS-CCA coupled system with such disordered local energies. We consider standard deviations whitin the range $0 \leq \sigma/J \leq 2$ and, for each selected σ, the same set of 10000 realizations is used to compute both the average measure of non-Markovianity and the average localization length. As a definition for this last quantity, we adopt the inverse partecipation number (IP) defined in (4.14), thus the localization length of $|\psi^0\rangle$ reads:

$$\lambda_0 = IP^{-1}(\psi^0) = \frac{1}{\sum_{x=1}^{N} |\langle\psi^0|x\rangle|^4} \tag{4.49}$$

In Fig (4.7a) we plot the mean value of $\lambda_0^{-1/2}$ as a function of the standard deviation σ (for $J = 1$). The mean value is calculated, for each σ, over the 10000 realizations of the local-energies set $\{\omega_x\}$. The inset of the figure show the corresponding standard error of the mean

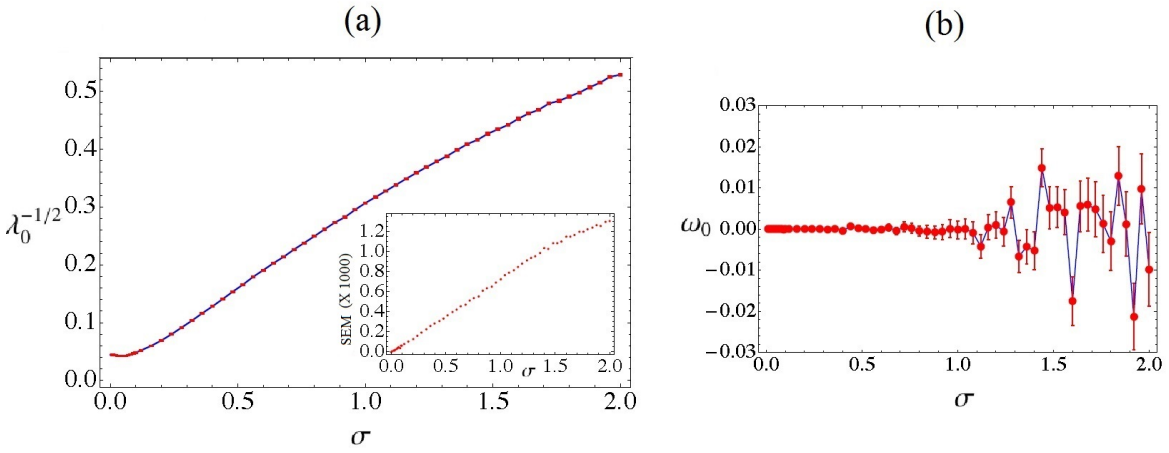

Figure 4.7: (a) Root of the inverse partecipation number ($IP_0^{1/2} = \lambda_0^{-1/2}$) of the eigenstate $|\psi^0\rangle$ with the maximum ratio $|\langle x_0|\psi^0\rangle|/\omega_0$ as a function of the disorder standard deviation σ (see text), for $J = 1$. The points represent the averages over 10000 realizations of the disordered bare-CCA with $N = 1001$, for each value of σ. In the inset are shown the corresponding standard errors of the mean (SEM) magnified by a factor 1000.
(b) Eigenvalue of $|\psi^0\rangle$ (ω_0) as a function of σ, averaged over 10000 realizations for the same disordered CCA. The bars indicate the corrisponding SEMs.

(SEM). Since we assume open boundary conditions, the eigenstate $|\psi^0\rangle$ in the uniform case (with associated $\omega = 0$ eigenvalue) has not the plane-wave $x-$representation, as in (2.52), but in this case it reads:

$$\psi^0(x) = \langle x|\psi^0\rangle = \sqrt{\frac{2}{N+1}}\sin(\pm\pi x/2) \quad for \quad \sigma = 0 \tag{4.50}$$

and the corresponding IP_0 is $\approx 2/N$, thus $\lambda_0^{-1/2} = IP_0^{1/2}$ approaches the value $\approx \sqrt{2/N}$ when $\sigma \to 0$. As the disorder is increased, λ_0 decreases until the upper limit of $\lambda_0^{-1/2} = 1$ is reached for very strong disorder. In this case, $|\psi^0\rangle$ is strongly localized around the central site and, as discussed in Sec. 4.1.2, the corresponding eigenvalue ω_0 coincides with the local energy ω_{x_0}. In Fig (4.7a) this limiting case is not reached, thus the value $\sigma = 2$ does not correspond to a disorder strength for which the CCA shows only single-site localized eigenstates (i.e. only the states with higher energies have single-site profiles). In Fig(4.7b) the eigenvalue ω_0, averaged over the different realizations, is plotted as a function of σ. It can be seen that the near-resonant condition for the choice of $|\psi_0\rangle$ is largely satisfied for $\sigma < 1$. For stronger disorder the error bars become larger and ω_0 begins to take random values around the zero.
The non-Markovianity measure of the TLS-CCA quantum evolution takes always finite values. However, in Fig (4.8a) the averaged value of $\mathcal{N}_{Vr}$, plotted as a function of σ, is not appreciably different from zero when $\sigma \to 0$. Clearly this depends on the negligible population trapping

in the strong-hopping regime (the bound contribution $\alpha_b(t)$ to the atomic amplitude, given in (3.13), oscillates with amplitude $\sim 10^{-5}$, so the residual oscillation of $\|\mathcal{A}(t)\| \to |\alpha_b(t))|^4$ is of the order $\sim 10^{-20}$ for $g/J = 0.1$ and $\sigma = 0$), as well as on the choice of t_{max}. The average measure increases with σ and approaches the unity when the disorder is strong enough. This means that when σ is large enough, on average, the TLS recovers from the environment the same amount of information which it has released. A further increase of the disorder does not change such dynamics. Indeed, when all the eigenstates show a localized profile, only a few of these contribute significantly to the atomic evolution, thus the probability amplitude $\alpha_e(t)$, for each realization, will include a small number of oscillating components (cf. Fig (4.5b) and (c)) and each of the two integrals in (4.48) will be ≈ 1 (if t_{max}, hence the linear extension of the CCA, is large enough). Clearly, in this case, both numerator and denominator of $\mathcal{N}_{Vr}$ are ≈ 1 for each single disorder realization. The averaged value of $\mathcal{N}_{Vr}$ is also plotted in Fig (4.8b) as a function of $\lambda_0^{-1/2}$. The threshold corresponds to the lower limit $\lambda_0^{-1/2} \approx \sqrt{2/N}$, i.e. $\sigma = 0$. The inset of the figure shows the small-disorder behaviour of the average $\mathcal{N}_{Vr}$ (dots) compared with the same non-Markovianity measure of an effective CQED model (solid line) that we here qualitatively discuss. We have described the damped CQED model in Sec. 1.1.2, by means of approximate solutions of the Linblad Master equation defined in (1.14) and (1.15). Here we consider the same model for an open cavity with infinite Q-factor, i.e. $k = 0$ and $\gamma \neq 0$. In this case the J-C level $|g, 1\rangle$ is not coupled to external modes, but the atom decays by direct coupling of the level $|e, 0\rangle$ to an external bath with rate γ. The atom-photon coupling constant or Vacuum-Rabi frequency is given in (1.4) and depends on $V^{-1/2}$, where V is the cavity volume. If we modify only one length of a 3D cavity, namely $\lambda = y/y_0$ (e.g. the distance between the mirrors in a Fabry-Perot setup along the y-axes), correspondingly the coupling constant varies according to $\Omega \propto \lambda^{-1/2}$. For a given realization of the disordered CCA with localization length λ_0, we select the coupling constant of the effective CQED model at $\Omega = g\lambda_0^{-1/2}$ and detuning $\delta = -\omega_0$. In other words, the eigenstate $|\psi^0\rangle$ chosen with the criterion discussed above plays the role of a cavity of frequency ω_0 which the atom is coupled to, with Rabi frequency Ω. Moreover, the bath of modes coupled to the level $|e, 0\rangle$ is chosen from an appropriate set of eigenstates of the disordered CCA by means of a numerical procedure. We compute, for a given realization, the density of states $\rho(\omega = 0)$ and, for each eigenmode $|\psi_l\rangle$, the overlap with the central site $\langle\psi_l|x_0\rangle$. The decay rate of the CQED model associated with this disorder realization is obtained by means of a Fermi's golden-rule argument and reads $\gamma = \frac{\pi}{N}\sum_{l=1}^{N} |\langle\psi_l|x_0\rangle|^2\rho(0)$. We use this values of Ω, γ and δ to solve the master equation of the open CQED model (in the basis $\{|g, 1\rangle, |e, 0\rangle\}$, with $k = 0$) given by (1.14), (1.15) and ((1.5) with $n = 1$). The corresponding atomic amplitude is used to compute the non-Markovianity measure, with the same definition. In this way, for a given σ, we associate with the i-th disorder realization the non-Markovianity measure $\mathcal{N}_{Vr}^i$, the correponding measure of the effective CQED model $\mathcal{N}_{Vr}^{(i)eff}$, the localization length λ_0^i and the effective coupling constant $\Omega^i = g/\sqrt{\lambda_0^i}$ (with detuning $-\omega_0^i$). In the inset of Fig (4.8b) are compared the two average measures (the averages, for a given σ, are calculated over $n_R = 10000$ realizations, i.e. $\mathcal{N} = \sum_{i=1}^{n_R} \mathcal{N}^i/n_R$), each of them as a function of $\lambda_0^{-1/2}$. This

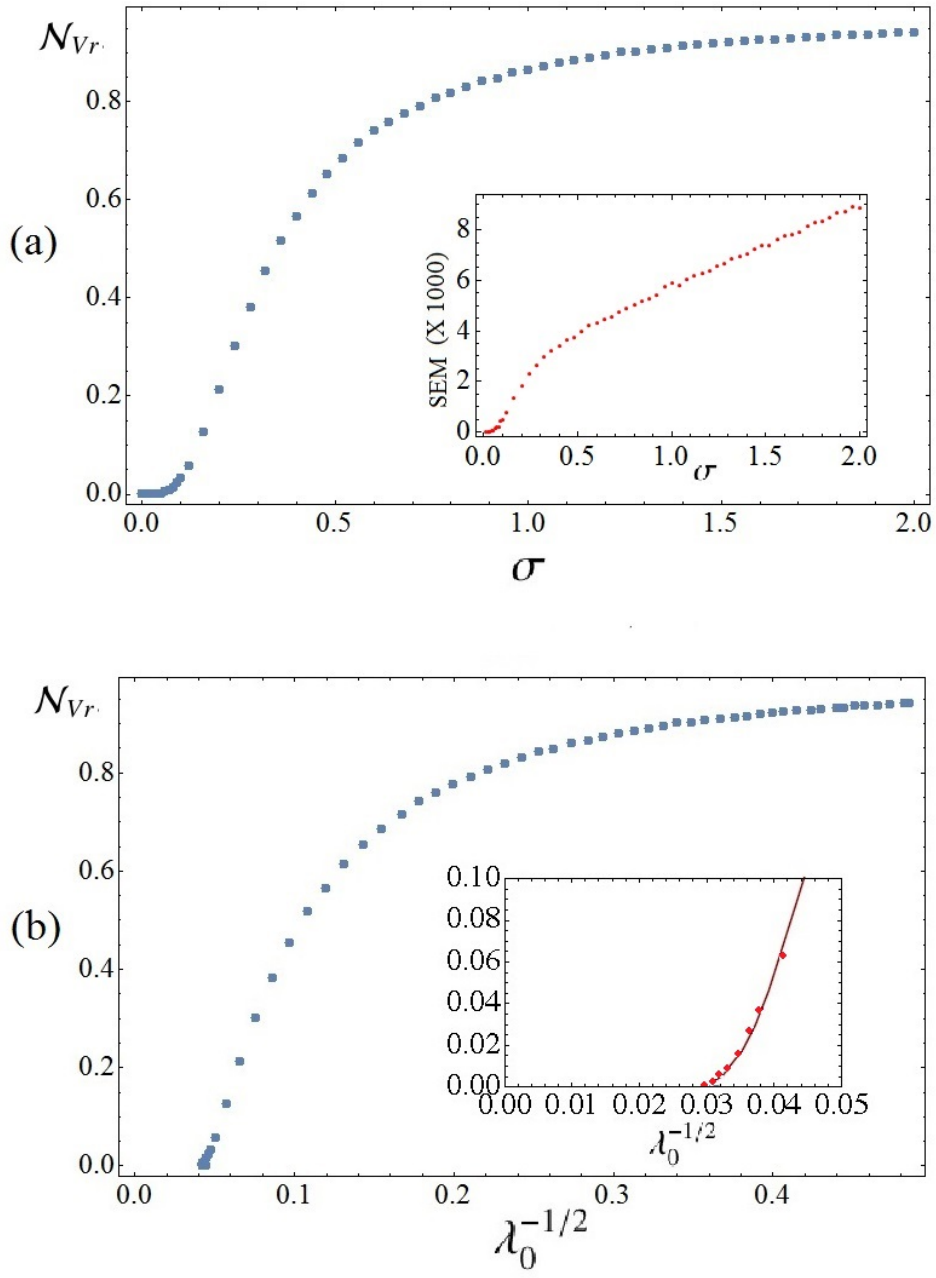

Figure 4.8: (a) Geometrical measure of non-Markovianity for the TLS-CCA quantum evolution as a function of the disorder standard deviation σ (for $J = 1$). The points represent the averages over 10000 realizations, for each value of σ, of the disordered CCA with $N = 1001$ and the TLS coupled to the central cavity with $g/J = 0.1$. In the inset are shown the corresponding standard errors of the mean (SEM) magnified by a factor 1000. (b) The same data of the non-Markovianity measure are plotted as a function of $\lambda_0^{-1/2} = IP_0^{1/2}$ (see text and Fig (4.7a)). The inset shows the non-Markovianity measure at small disorder of the TLS-CCA (dots) compared with the same measure for the effective open CQED model discussed in the text (solid line).

last quantity, also averaged over n_R realizations for a given disorder, represents both the size of the nearly resonant eigenstate and the coupling constant of the effective CQED. A good agreement between the TLS-CCA and the open CQED dynamics is found for small disorder. Indeed, the atomic evolution in the strong-hopping regime of the uniform CCA is dominated by the contributions of nearly resonant unbound states which show excitonic components characterized by the peaked distribution $F(k)$, given in (3.20), centered around $k = \pm\pi/2$ (corresponding to $\omega = 0$). In the case of small disorder this distribution is not significantly modified and, on average, $\omega_0 \approx 0$ [cf. Fig (4.8b)]. In these conditions, in which the eigenmodes with significant overlap $\langle\psi_l|x_0\rangle$ are still the near-resonant ones, the open CQED model with the numerical computation of the decay rate γ discussed above provides a good approximation of the atomic dynamics. Finally, we point out that both measures of non-Markovianity approach the unity for strong enough disorder (not shown in figure). Indeed, the effective model associated with a strongly disordered CCA corresponds to a CQED setup with large coupling constant and small decay rate, since the major part of the eigenmodes has not significant overlap with the central site of the CCA. Clearly, in the limiting case of very large σ the detuned CQED dynamics with $\gamma = 0$ and Rabi frequency $\Omega = g$ is retrived.

Conclusions

In this thesis some aspects of the interesting physics of a one-dimensional coupled cavity array (CCA), interacting with a two-level atom (TLS), have been theoretically investgated. The array consist of an arrangement of low-loss QED cavities with nearest-neighbor coupling allowing photon hopping (due to the overlap of the evanescent field modes) between neighboring cavities. In particular, we have examined the single-excitation transport dynamics in the emission process when the atom is coupled in the strong-coupling regime to the central cavity of a long CCA, either in the uniform case as in presence of static disorder. A tight-binding model, with Hamiltonian under rotating-wave approximation, has been adopted and the atom turns out to be effectively coupled to a finite band of bath modes with constant coupling strength. Similar models have been widely used in the framework of scattering problems, for both the CCA (with one or more TLS [17, 18, 19, 22, 23, 25, 31]) and equivalent condensed matter systems [28]. The Green's function approach, used to investigate the spectral properties, provided the mathematical tools needed to analyze the atomic dynamics and the photon-localization.
The main results concerning the interacion of a TLS with the uniform CCA have been discussed in Sec. 3.2. By investigating the time evolution of the atomic population as well as the photon probability distribution across the array, we have highlighted the occurrence of several regimes. For very weak values of the coupling-strength (with respect to the photon-hopping rate) and at resonance, standard exponential decay of the atom's population takes place. At the same time, the photon wave function spreads in either direction of the array in such a way that, for long enough times, it vanishes within any finite region around the central cavity. In this strong-hopping limiting case, the atom 'sees' an almost flat spectral-density bath and only the near resonant modes significantly contribute to the atomic dynamics (the effects due to the finiteness of the band are negligible). In contrast, when the coupling is large enough, the field fully localizes close to the atom's site since in this limit the dynamics reduces to the well-known Jaynes-Cummings model. Correspondingly, full population trapping takes place and the atom periodically exchanges the entire content of its initial energy with the localized field so as to exhibit standard vacuum Rabi oscillations. At intermediate coupling, in general, the dynamics features partial field localization and atomic fractional decay, the latter being due to population trapping that manifests as a residual oscillation of the atom's excitation at large times. Population trapping and photon localization are phenomena which arise due to the presence of a pair of atom-photon bound states whose properties (such as the localization lengths and excitonic

components) have been analyzed in detail. At resonance these polaritonic states are associated with two discrete eigenvalues external and symmetrical with respect to the band center and their exponential decreasing spatial-profiles are identical (up to a phase factor). Population trapping become relevant when the bound states show also large excitonic components. We found that, as the atom-cavity coupling constant grows from zero, field localization becomes significant before population trapping takes place. In particular, when the coupling is chosen within a given range, at long times, there is appreciable localization of the field around the atomic position, while the atom remains almost completely de-excited, i.e. population trapping is negligible. In these conditions the field undergoes a mere spatial redistribution whitin the central region of the array [15]. This regime is not strongly modified by the presence of moderate atom-cavity detuning. The main effect of a detuned interaction with respect to the resonant case is an increase of the atomic trapped energy. Indeed, for very large detuning, the dispersive regime is reached and the atom does not decay. We found that, if the coupling constant is not too large, the energy associated with the localized field is not a monotonic function of the detuning and shows a maximum near the band-edges. This localized-field energy exhibits a narrow peak around the band edges for small coupling, i.e. significant localization of the field arises only when the atomic transition energy is setted at the band edges. Correspondigly the population trapping shows a sharp transition between 0 and 1 when the detuning crosses this thresholds. Moreover we have shown that, for any value of the coupling constant, the ratio between the localized energy and the trapped one (at long times) always decreases as the detuning increases. As result, the effect of field localization without population trapping, maximum at resonance, is still present for not too strong detuning, but it occurs within a narrower range of the coupling constant.
The last chapter is devoted to the study of the TLS-CCA interaction in presence of static disorder. We have considered a completely disordered CCA, with random cavity-mode frequencies statistically independent on the position (but uniform in the hopping rate) in the strong-hopping atom-field regime. In this case each cavity behaves as a defect and back-scatters a fraction of the atomic excitation impinging on it. If the disorder is strong enough, the atomic Markovian decay is prevented as the atom cannot get rid of its excitation. In such an 1D system Anderson localization takes place and all eigenstates are localized and exhibit a probability profile, in the x-representation, the more localized the stronger the disorder. We have implemented the model by numerical diagonalization of the TLS-CCA Hamiltonian with gaussian disorder for several realizations of the latter, characterized by different values of the associated standard deviation (σ). Using the open quantum systems approach, we have investigated, from a more general perspective, the Non-Markovianity for the coupling between the TLS and the disordered-CCA. This latter performs a particular environment, characterized by a given set of eigenmodes whose energy and position-distribution depend on the disorder strength. The geometrical measure of non-Markovianity [56], that quantifies the complexive back-flow of information from the environment to the system, has been adopted and several simulations for different values of σ have been performed (for each disorder strength we have averaged the measures over 10000 realizations of the disordered CCA). In this way we have analyzed the behaviour of the average non-Markovianity as a function of the localization length of the eigenstate which exhibits the

largest overlap on the atomic site (this length is also an average over 10000 realizations for each σ). As results, if the disorder is not too strong, the non-Markovianity profile so obtained is comparable with the corresponding measure calculated for a TLS which interacts with a single open-cavity with a suitable volume (i.e. with a suitable coupling constant) and detuning. The decay rate for this effective model is obtained by means of a numerical procedure that takes into account a given set of localized eigenmodes of the disordered CCA. We found a good agreement since, although some disorder is introduced, the eigenmodes with significant overlap on the central site are still the near-resonant ones and the open CQED model provides a good approximation of the TLS-CCA dynamics. Moreover, the measures of non-Markovianity for both the CCA and the open cavity environments approach the unity and the agreement is also found for very strong disorder (in this case the effective cavity is nearly closed since the atom mainly interacts with only a localizied state of the CCA and a detuned Jaynes-Cummings dynamics is retrived). Further investigations are needed to extend this study to the regime of intermediate disorder strength.

Appendix A: Green's function expansion

Let $\hat{G}'_0(z)$ be the green function associated with $\hat{H}'_0 = \hat{H}_0 + \omega_a|e\rangle\langle e|$ (see Eq. (2.77)). The eigenstates of the latter, in the overall Hilbert space, are $\{|\varphi_k\rangle\}$ and $|e\rangle$ with eigenvalues $\omega_k = \omega_c + 2J\cos k$ and ω_a, respectively. Hence, using the corresponding spectral decomposition of $\hat{H}'_0$,

$$\hat{G}'_0(z) = \frac{|e\rangle\langle e|}{z-\omega_a} + \sum_k \frac{|\varphi_k\rangle\langle\varphi_k|}{z-\omega_k}\,. \tag{51}$$

$\hat{G}(z)$ can be linked with $\hat{G}'_0(z)$ through the series expansion in (2.12) that in this case reads:

$$\hat{G}(z) = \hat{G}'_0(z) + \hat{G}'_0(z)\hat{H}_{ac}\hat{G}'_0(z) + \hat{G}'_0(z)\hat{H}_{ac}\hat{G}'_0(z)\hat{H}_{ac}\hat{G}'_0(z) + ... \tag{52}$$

This can be regarded as a series expansion of $\hat{G}(z)$ in terms of powers of the coupling strength g, the form of which reads (we omit the dependence on z since this is unnecessary for the scopes of this section):

$$\hat{G} = \hat{G}^{(0)} + \hat{G}^{(1)}g + \hat{G}^{(2)}g^2 + ...\,, \tag{53}$$

where $\hat{G}^{(0)} \equiv \hat{G}'_0$, $\hat{G}^{(1)} = g^{-1}\hat{G}'_0\hat{H}_{ac}\hat{G}'_0$, ..., each $\hat{G}^{(k)}$ thus being independent of g. Using this along with Eq. (51) and the fact that in the one-excitation-sector $\hat{H}_{ac} = g|e\rangle\langle 0|$+h.c., up to the 4th power in g we find:

$$\begin{aligned}
\hat{G}^{(1)} &= \hat{G}'_0\,(|e\rangle\langle 0| + |0\rangle\langle e|)\,\hat{G}'_0\,,\\
\hat{G}^{(2)} &= \hat{G}'_0\,(G_{00}|e\rangle\langle e| + G_{0e}|0\rangle\langle 0|)\,\hat{G}'_0\,,\\
\hat{G}^{(3)} &= G_{00}G_{0e}\;\hat{G}'_0(|e\rangle\langle 0| + |0\rangle\langle e|)\,\hat{G}'_0\,,\\
\hat{G}^{(4)} &= G_{00}G_{0e}\,\hat{G}'_0(G_{00}|e\rangle\langle e| + G_{0e}|0\rangle\langle 0|)\,\hat{G}'_0
\end{aligned}$$

By induction, this is generalized for any integer $k \geq 1$ as

$$\begin{aligned}
\hat{G}^{(2k+1)} &= (G_{00}G_{0e})^k\,\hat{G}'_0(|e\rangle\langle 0| + |0\rangle\langle e|)\,\hat{G}'_0\,,\\
\hat{G}^{(2k)} &= (G_{00}G_{0e})^{k-1}\,\hat{G}'_0(G_{00}|e\rangle\langle e| + G_{0e}|0\rangle\langle 0|)\,\hat{G}'_0\,.
\end{aligned}$$

Note that even and odd power terms are always proportional to $\hat{G}'_0\,(G_{00}|e\rangle\langle e| + G_{0e}|0\rangle\langle 0|)\,\hat{G}'_0$ and $\hat{G}'_0\,(|e\rangle\langle 0| + |0\rangle\langle e|)\,\hat{G}'_0$, respectively. By introducing now the geometric series $f = g\sum_{n=0}^{\infty}(g^2G_{00}G_{0e})^n$, whose sum coincides with Eq. (2.81), together with functions $f_1(z) = gG_{00}(z)f(z)$ and $f_2(z) = gG_{0e}(z)f(z)$, we straightforwardly end up with Eq. (2.80). From Eq. (51), $G_{0e}(z) = (z-\omega_a)^{-1}$ and

$$G_{00}(z) = \sum_k \frac{|\langle\varphi_k|0\rangle|^2}{z-\omega_k} \;\overset{N\gg 1}{\longrightarrow}\; \frac{1}{2\pi}\int_{-\pi}^{\pi} dk\,\frac{1}{z-\omega_c-2J\cos k}\,, \tag{54}$$

where we computed the thermodynamic limit $N \gg 1$ [in this limit, owing to Eq. (2.54), $2\pi/N \to dk$].

Appendix B: Bound stationary states at resonance

Based on (2.80) and recalling that $f_1(z) = gG_{00}(z)f(z)$, $f_2(z) = gG_{0e}(z)f(z)$, the residues needed for the calculation of $|\psi_0^\pm\rangle\langle\psi_0^\pm|$ are given by

$$r = \mathrm{Res}(f, \omega_{0\pm}) = \pm \frac{g^5}{2\sqrt{g^4+4J^4}\sqrt{2J^2+\sqrt{g^4+4J^4}}}, \tag{55}$$

$$r_1 = \mathrm{Res}(f_1, \omega_{0\pm}) = \frac{g^4}{2\sqrt{g^4+4J^4}}, \tag{56}$$

$$r_2 = \mathrm{Res}(f_2, \omega_{0\pm}) = \frac{g^6}{2\sqrt{g^4+4J^4}(2J^2+\sqrt{g^4+4J^4})}. \tag{57}$$

Substituting these in $\mathrm{Res}(\hat{G}, \omega_{0\pm})$ yields

$$\begin{aligned} |\psi_0^\pm\rangle\langle\psi_0^\pm| &= -\frac{r}{2\pi\omega_{0+}}\int_{-\pi}^{\pi} dk\, \frac{|e\rangle\langle\phi_k| + \mathrm{h.c.}}{\omega_k \mp \omega_{0+}} + \frac{r_1}{\omega_{0+}^2}|e\rangle\langle e| \\ &\quad + \frac{r_2}{4\pi^2}\int_{-\pi}^{\pi} dk \int_{-\pi}^{\pi} dk' \frac{|\phi_k\rangle\langle\phi_{k'}|}{(\omega_k \mp \omega_{0+})(\omega_{k'} \mp \omega_{0+})}. \end{aligned} \tag{58}$$

Setting $x_0 = 0$, the matrix elements of projector (58) are calculated as

$$\langle e|\psi_0^\pm\rangle\langle\psi_0^\pm|e\rangle = \frac{r_1}{\omega_{0+}^2}, \tag{59}$$

$$\begin{aligned} \langle x|\psi_0^\pm\rangle\langle\psi_0^\pm|x'\rangle &= \frac{r_2}{4\pi^2}\int_{-\pi}^{\pi} dk \frac{e^{ikx}}{\omega_{0+} \mp \omega_k}\int_{-\pi}^{\pi} dk' \frac{e^{-ik'x'}}{\omega_{0+} \mp \omega_{k'}} \\ &= \frac{r_2}{\omega_{0+}^2 - 4J^2}(\pm\varrho)^{|x|+|x'|}, \end{aligned} \tag{60}$$

$$\langle e|\psi_0^\pm\rangle\langle\psi_0^\pm|x\rangle = \langle x|\psi_0^\pm\rangle\langle\psi_0^\pm|e\rangle = \pm\frac{r}{\omega_{0+}\sqrt{\omega_{0+}^2 - 4J^2}}(\pm\varrho)^{|x|}, \tag{61}$$

where ϱ is given in Eq. (2.90). In deriving Eqs. (60) and (61) we have used Eq. (2.57). Based on (2.90), (57) and (59), the following identity holds

$$\frac{r_2}{\omega_{0+}^2 - 4J^2} = \frac{(1-c_{e0}^2)(1-\varrho^2)}{1+\varrho^2}. \tag{62}$$

Using this and the identity $\sqrt{r_1 r_2} = r$ [cf. Eqs. (55)-(57)] one can check that the projector associated with state (2.88) has the same matrix elements as those in (59), (60) and (61). This proves (up to an irrelevant phase factor) that the state corresponding to projector (58) is indeed given by Eq. (2.88).

Appendix C: Solutions of quartic equation (2.85)

In what follows are reported the solutions of (2.85). Depending on the pair $\{g, \delta\}$, some of these are real.

$$
\begin{aligned}
z1 = {} & -\frac{\delta}{2} - \frac{1}{2}\sqrt{\left(4\,\mathcal{J}^2 + \frac{1}{3}\left(-4\,\mathcal{J}^2 + \delta^2\right) + \frac{2^{1/3}\left(-12\,g^4 + \left(-4\,\mathcal{J}^2 + \delta^2\right)^2\right)}{3\left(-108\,g^4\,\delta^2 + 72\,g^4\left(-4\,\mathcal{J}^2 + \delta^2\right) + 2\left(-4\,\mathcal{J}^2 + \delta^2\right)^3 + \sqrt{-4\left(-12\,g^4 + \left(-4\,\mathcal{J}^2 + \delta^2\right)^2\right)^3 + \left(-108\,g^4\,\delta^2 + 72\,g^4\left(-4\,\mathcal{J}^2 + \delta^2\right) + 2\left(-4\,\mathcal{J}^2 + \delta^2\right)^3\right)^2}\right)^{1/3}} + \right.} \\
& \left.\frac{\left(-108\,g^4\,\delta^2 + 72\,g^4\left(-4\,\mathcal{J}^2 + \delta^2\right) + 2\left(-4\,\mathcal{J}^2 + \delta^2\right)^3 + \sqrt{-4\left(-12\,g^4 + \left(-4\,\mathcal{J}^2 + \delta^2\right)^2\right)^3 + \left(-108\,g^4\,\delta^2 + 72\,g^4\left(-4\,\mathcal{J}^2 + \delta^2\right) + 2\left(-4\,\mathcal{J}^2 + \delta^2\right)^3\right)^2}\right)^{1/3}}{3\times 2^{1/3}}\right) - \\
& \frac{1}{2}\sqrt{\left(4\,\mathcal{J}^2 + \delta^2 + \frac{1}{3}\left(4\,\mathcal{J}^2 - \delta^2\right) - \frac{2^{1/3}\left(-12\,g^4 + \left(-4\,\mathcal{J}^2 + \delta^2\right)^2\right)}{3\left(-108\,g^4\,\delta^2 + 72\,g^4\left(-4\,\mathcal{J}^2 + \delta^2\right) + 2\left(-4\,\mathcal{J}^2 + \delta^2\right)^3 + \sqrt{-4\left(-12\,g^4 + \left(-4\,\mathcal{J}^2 + \delta^2\right)^2\right)^3 + \left(-108\,g^4\,\delta^2 + 72\,g^4\left(-4\,\mathcal{J}^2 + \delta^2\right) + 2\left(-4\,\mathcal{J}^2 + \delta^2\right)^3\right)^2}\right)^{1/3}} - \right.} \\
& \left.\frac{\left(-108\,g^4\,\delta^2 + 72\,g^4\left(-4\,\mathcal{J}^2 + \delta^2\right) + 2\left(-4\,\mathcal{J}^2 + \delta^2\right)^3 + \sqrt{-4\left(-12\,g^4 + \left(-4\,\mathcal{J}^2 + \delta^2\right)^2\right)^3 + \left(-108\,g^4\,\delta^2 + 72\,g^4\left(-4\,\mathcal{J}^2 + \delta^2\right) + 2\left(-4\,\mathcal{J}^2 + \delta^2\right)^3\right)^2}\right)^{1/3}}{3\times 2^{1/3}}\right) - \\
& \left(-8\,\delta^3 + 8\,\delta\left(-4\,\mathcal{J}^2 + \delta^2\right)\right)\Big/\left(4\sqrt{\left(4\,\mathcal{J}^2 + \frac{1}{3}\left(-4\,\mathcal{J}^2 + \delta^2\right) + \frac{2^{1/3}\left(-12\,g^4 + \left(-4\,\mathcal{J}^2 + \delta^2\right)^2\right)}{3\left(-108\,g^4\,\delta^2 + 72\,g^4\left(-4\,\mathcal{J}^2 + \delta^2\right) + 2\left(-4\,\mathcal{J}^2 + \delta^2\right)^3 + \sqrt{-4\left(-12\,g^4 + \left(-4\,\mathcal{J}^2 + \delta^2\right)^2\right)^3 + \left(-108\,g^4\,\delta^2 + 72\,g^4\left(-4\,\mathcal{J}^2 + \delta^2\right) + 2\left(-4\,\mathcal{J}^2 + \delta^2\right)^3\right)^2}\right)^{1/3}} + \right.}\right. \\
& \left.\left.\frac{\left(-108\,g^4\,\delta^2 + 72\,g^4\left(-4\,\mathcal{J}^2 + \delta^2\right) + 2\left(-4\,\mathcal{J}^2 + \delta^2\right)^3 + \sqrt{-4\left(-12\,g^4 + \left(-4\,\mathcal{J}^2 + \delta^2\right)^2\right)^3 + \left(-108\,g^4\,\delta^2 + 72\,g^4\left(-4\,\mathcal{J}^2 + \delta^2\right) + 2\left(-4\,\mathcal{J}^2 + \delta^2\right)^3\right)^2}\right)^{1/3}}{3\times 2^{1/3}}\right)\right);
\end{aligned}
$$

$$
\begin{aligned}
z2 = {} & -\frac{\delta}{2} - \frac{1}{2}\sqrt{\left(4\,\mathcal{J}^2 + \frac{1}{3}\left(-4\,\mathcal{J}^2 + \delta^2\right) + \left(2^{1/3}\left(-12\,g^4 + \left(-4\,\mathcal{J}^2 + \delta^2\right)^2\right)\right)\Big/\right.} \\
& \left.\left(3\left(-108\,g^4\,\delta^2 + 72\,g^4\left(-4\,\mathcal{J}^2 + \delta^2\right) + 2\left(-4\,\mathcal{J}^2 + \delta^2\right)^3 + \sqrt{-4\left(-12\,g^4 + \left(-4\,\mathcal{J}^2 + \delta^2\right)^2\right)^3 + \left(-108\,g^4\,\delta^2 + 72\,g^4\left(-4\,\mathcal{J}^2 + \delta^2\right) + 2\left(-4\,\mathcal{J}^2 + \delta^2\right)^3\right)^2}\right)^{1/3}\right) + \right. \\
& \left.\frac{1}{3\times 2^{1/3}}\left(-108\,g^4\,\delta^2 + 72\,g^4\left(-4\,\mathcal{J}^2 + \delta^2\right) + 2\left(-4\,\mathcal{J}^2 + \delta^2\right)^3 + \sqrt{-4\left(-12\,g^4 + \left(-4\,\mathcal{J}^2 + \delta^2\right)^2\right)^3 + \left(-108\,g^4\,\delta^2 + 72\,g^4\left(-4\,\mathcal{J}^2 + \delta^2\right) + 2\left(-4\,\mathcal{J}^2 + \delta^2\right)^3\right)^2}\right)^{1/3}\right) + \\
& \frac{1}{2}\sqrt{\left(4\,\mathcal{J}^2 + \delta^2 + \frac{1}{3}\left(4\,\mathcal{J}^2 - \delta^2\right) - \left(2^{1/3}\left(-12\,g^4 + \left(-4\,\mathcal{J}^2 + \delta^2\right)^2\right)\right)\Big/\right.} \\
& \left.\left(3\left(-108\,g^4\,\delta^2 + 72\,g^4\left(-4\,\mathcal{J}^2 + \delta^2\right) + 2\left(-4\,\mathcal{J}^2 + \delta^2\right)^3 + \sqrt{-4\left(-12\,g^4 + \left(-4\,\mathcal{J}^2 + \delta^2\right)^2\right)^3 + \left(-108\,g^4\,\delta^2 + 72\,g^4\left(-4\,\mathcal{J}^2 + \delta^2\right) + 2\left(-4\,\mathcal{J}^2 + \delta^2\right)^3\right)^2}\right)^{1/3}\right) - \right. \\
& \left.\frac{1}{3\times 2^{1/3}}\left(-108\,g^4\,\delta^2 + 72\,g^4\left(-4\,\mathcal{J}^2 + \delta^2\right) + 2\left(-4\,\mathcal{J}^2 + \delta^2\right)^3 + \sqrt{-4\left(-12\,g^4 + \left(-4\,\mathcal{J}^2 + \delta^2\right)^2\right)^3 + \left(-108\,g^4\,\delta^2 + 72\,g^4\left(-4\,\mathcal{J}^2 + \delta^2\right) + 2\left(-4\,\mathcal{J}^2 + \delta^2\right)^3\right)^2}\right)^{1/3}\right) - \right. \\
& \left.\left(-8\,\delta^3 + 8\,\delta\left(-4\,\mathcal{J}^2 + \delta^2\right)\right)\Big/\left(4\sqrt{\left(4\,\mathcal{J}^2 + \frac{1}{3}\left(-4\,\mathcal{J}^2 + \delta^2\right) + \left(2^{1/3}\left(-12\,g^4 + \left(-4\,\mathcal{J}^2 + \delta^2\right)^2\right)\right)\Big/\right.}\right. \\
& \left.\left.\left(3\left(-108\,g^4\,\delta^2 + 72\,g^4\left(-4\,\mathcal{J}^2 + \delta^2\right) + 2\left(-4\,\mathcal{J}^2 + \delta^2\right)^3 + \sqrt{\left(-4\left(-12\,g^4 + \left(-4\,\mathcal{J}^2 + \delta^2\right)^2\right)^3 + \left(-108\,g^4\,\delta^2 + 72\,g^4\left(-4\,\mathcal{J}^2 + \delta^2\right) + 2\left(-4\,\mathcal{J}^2 + \delta^2\right)^3\right)^2\right)}\right)^{1/3}\right) + \right.\right. \\
& \left.\left.\frac{1}{3\times 2^{1/3}}\left(-108\,g^4\,\delta^2 + 72\,g^4\left(-4\,\mathcal{J}^2 + \delta^2\right) + 2\left(-4\,\mathcal{J}^2 + \delta^2\right)^3 + \sqrt{\left(-4\left(-12\,g^4 + \left(-4\,\mathcal{J}^2 + \delta^2\right)^2\right)^3 + \left(-108\,g^4\,\delta^2 + 72\,g^4\left(-4\,\mathcal{J}^2 + \delta^2\right) + 2\left(-4\,\mathcal{J}^2 + \delta^2\right)^3\right)^2\right)}\right)^{1/3}\right)\right);
\end{aligned}
$$

$$z3= -\frac{\delta}{2}+\frac{1}{2}\sqrt{4 J^2+\frac{1}{3}\left(-4 J^2+\delta^2\right)+\frac{2^{1/3}\left(-12 g^4+\left(-4 J^2+\delta^2\right)^2\right)}{3\left(-108 g^4 \delta^2+72 g^4\left(-4 J^2+\delta^2\right)+2\left(-4 J^2+\delta^2\right)^3+\sqrt{-4\left(-12 g^4+\left(-4 J^2+\delta^2\right)^2\right)^3+\left(-108 g^4 \delta^2+72 g^4\left(-4 J^2+\delta^2\right)+2\left(-4 J^2+\delta^2\right)^3\right)^2}\right)^{1/3}}+\frac{1}{3\times 2^{1/3}}\left(-108 g^4 \delta^2+72 g^4\left(-4 J^2+\delta^2\right)+2\left(-4 J^2+\delta^2\right)^3+\sqrt{-4\left(-12 g^4+\left(-4 J^2+\delta^2\right)^2\right)^3+\left(-108 g^4 \delta^2+72 g^4\left(-4 J^2+\delta^2\right)+2\left(-4 J^2+\delta^2\right)^3\right)^2}\right)^{1/3}}-\frac{1}{2}\sqrt{4 J^2+\delta^2+\frac{1}{3}\left(4 J^2-\delta^2\right)-\frac{2^{1/3}\left(-12 g^4+\left(-4 J^2+\delta^2\right)^2\right)}{3\left(-108 g^4 \delta^2+72 g^4\left(-4 J^2+\delta^2\right)+2\left(-4 J^2+\delta^2\right)^3+\sqrt{-4\left(-12 g^4+\left(-4 J^2+\delta^2\right)^2\right)^3+\left(-108 g^4 \delta^2+72 g^4\left(-4 J^2+\delta^2\right)+2\left(-4 J^2+\delta^2\right)^3\right)^2}\right)^{1/3}}-\frac{1}{3\times 2^{1/3}}\left(-108 g^4 \delta^2+72 g^4\left(-4 J^2+\delta^2\right)+2\left(-4 J^2+\delta^2\right)^3+\sqrt{-4\left(-12 g^4+\left(-4 J^2+\delta^2\right)^2\right)^3+\left(-108 g^4 \delta^2+72 g^4\left(-4 J^2+\delta^2\right)+2\left(-4 J^2+\delta^2\right)^3\right)^2}\right)^{1/3}+\frac{-8 \delta^3+8 \delta\left(-4 J^2+\delta^2\right)}{4\sqrt{4 J^2+\frac{1}{3}\left(-4 J^2+\delta^2\right)+\frac{2^{1/3}\left(-12 g^4+\left(-4 J^2+\delta^2\right)^2\right)}{3\left(-108 g^4 \delta^2+72 g^4\left(-4 J^2+\delta^2\right)+2\left(-4 J^2+\delta^2\right)^3+\sqrt{-4\left(-12 g^4+\left(-4 J^2+\delta^2\right)^2\right)^3+\left(-108 g^4 \delta^2+72 g^4\left(-4 J^2+\delta^2\right)+2\left(-4 J^2+\delta^2\right)^3\right)^2}\right)^{1/3}}+\frac{1}{3\times 2^{1/3}}\left(-108 g^4 \delta^2+72 g^4\left(-4 J^2+\delta^2\right)+2\left(-4 J^2+\delta^2\right)^3+\sqrt{-4\left(-12 g^4+\left(-4 J^2+\delta^2\right)^2\right)^3+\left(-108 g^4 \delta^2+72 g^4\left(-4 J^2+\delta^2\right)+2\left(-4 J^2+\delta^2\right)^3\right)^2}\right)^{1/3}}}} \;;$$

$$z4= -\frac{\delta}{2}+\frac{1}{2}\sqrt{4 J^2+\frac{1}{3}\left(-4 J^2+\delta^2\right)+\frac{2^{1/3}\left(-12 g^4+\left(-4 J^2+\delta^2\right)^2\right)}{3\left(-108 g^4 \delta^2+72 g^4\left(-4 J^2+\delta^2\right)+2\left(-4 J^2+\delta^2\right)^3+\sqrt{-4\left(-12 g^4+\left(-4 J^2+\delta^2\right)^2\right)^3+\left(-108 g^4 \delta^2+72 g^4\left(-4 J^2+\delta^2\right)+2\left(-4 J^2+\delta^2\right)^3\right)^2}\right)^{1/3}}+\frac{1}{3\times 2^{1/3}}\left(-108 g^4 \delta^2+72 g^4\left(-4 J^2+\delta^2\right)+2\left(-4 J^2+\delta^2\right)^3+\sqrt{-4\left(-12 g^4+\left(-4 J^2+\delta^2\right)^2\right)^3+\left(-108 g^4 \delta^2+72 g^4\left(-4 J^2+\delta^2\right)+2\left(-4 J^2+\delta^2\right)^3\right)^2}\right)^{1/3}}+\frac{1}{2}\sqrt{4 J^2+\delta^2+\frac{1}{3}\left(4 J^2-\delta^2\right)-\frac{2^{1/3}\left(-12 g^4+\left(-4 J^2+\delta^2\right)^2\right)}{3\left(-108 g^4 \delta^2+72 g^4\left(-4 J^2+\delta^2\right)+2\left(-4 J^2+\delta^2\right)^3+\sqrt{-4\left(-12 g^4+\left(-4 J^2+\delta^2\right)^2\right)^3+\left(-108 g^4 \delta^2+72 g^4\left(-4 J^2+\delta^2\right)+2\left(-4 J^2+\delta^2\right)^3\right)^2}\right)^{1/3}}-\frac{1}{3\times 2^{1/3}}\left(-108 g^4 \delta^2+72 g^4\left(-4 J^2+\delta^2\right)+2\left(-4 J^2+\delta^2\right)^3+\sqrt{-4\left(-12 g^4+\left(-4 J^2+\delta^2\right)^2\right)^3+\left(-108 g^4 \delta^2+72 g^4\left(-4 J^2+\delta^2\right)+2\left(-4 J^2+\delta^2\right)^3\right)^2}\right)^{1/3}+\frac{-8 \delta^3+8 \delta\left(-4 J^2+\delta^2\right)}{4\sqrt{4 J^2+\frac{1}{3}\left(-4 J^2+\delta^2\right)+\frac{2^{1/3}\left(-12 g^4+\left(-4 J^2+\delta^2\right)^2\right)}{3\left(-108 g^4 \delta^2+72 g^4\left(-4 J^2+\delta^2\right)+2\left(-4 J^2+\delta^2\right)^3+\sqrt{-4\left(-12 g^4+\left(-4 J^2+\delta^2\right)^2\right)^3+\left(-108 g^4 \delta^2+72 g^4\left(-4 J^2+\delta^2\right)+2\left(-4 J^2+\delta^2\right)^3\right)^2}\right)^{1/3}}+\frac{1}{3\times 2^{1/3}}\left(-108 g^4 \delta^2+72 g^4\left(-4 J^2+\delta^2\right)+2\left(-4 J^2+\delta^2\right)^3+\sqrt{-4\left(-12 g^4+\left(-4 J^2+\delta^2\right)^2\right)^3+\left(-108 g^4 \delta^2+72 g^4\left(-4 J^2+\delta^2\right)+2\left(-4 J^2+\delta^2\right)^3\right)^2}\right)^{1/3}}}}$$

Bibliography

[1] M. J. Hartmann, F. G. S. L. Brandão, and M. Plenio - Laser & Photon. Rev. **2**, 527 (2008); Nature Phys. **2**, 849 (2006); M. J. Hartmann and M. Plenio - Phys. Rev. Lett. **99**, 103601 (2007).

[2] M. J. Hartmann, F. G. S. L. Brandão, and M. Plenio - Phys. Rev. Lett. **99**, 160501 (2007); A. Kay, D. G. Angelakis - Europhys. Lett. **84**, no 2 (2008); P. Li, Q. Gong, and G. Guo - Eur. Phys. J. D, **55**, pp 205-9 (2009); J. Cho, D. G. Angelakis, and S. Bose - Phys. Rev. A **78**, 062338 (2008).

[3] D. G. Angelakis, M. F. Santos and S. Bose - Phys. Rev. A **76**, 031805(R) (2007).

[4] A. D. Greentree, C. Tahan, J. H. Cole, L. C. L. Hollenberg - Nature Phys. **2**, 856-861 (2006); M. I. Makin, J. H. Cole, C. Tahan, L. C. L. Hollenberg, and A. D. Greentree - Phys. Rev. A 77, 053819 (2008); D. Rossini and R. Fazio - Phys. Rev. Lett. **99**, 186401 (2007); M. Aichhorn, M. Hohenadler, C. Tahan, and P. B. Littlewood - Phys. Rev. Lett. **100**, 216401 (2008); E. K. Irish, C. D. Ogden, and M. S. Kim - Phys. Rev. A **77**, 033801 (2008).

[5] D. G. Angelakis, M. F. Santos, V. Yannopapas, and A. Ekert - Phys. Lett. A **362**, 377 (2007); D. G. Angelakis and A. Kay - New J. Phys. **10**, 023012 (2008); S. Bose, D. G. Angelakis, and D. Burgarth - J. Mod. Opt. **54**, 2307 (2007); D. G. Angelakis, S. Mancini, and S. Bose - Europhys. Lett. **85**, no 2 (2009); J. Cho, D. G. Angelakis, and S. Bose - Phys. Rev. A **78**, 022323 (2008).

[6] L. Zhou, J. Lu, and C. P. Sun - Phys. Rev. A **76**, 012313 (2007); F. M. Hu, L. Zhou, T. Shi, and C. P. Sun - Phys. Rev. A 76, 013819 (2007); L. Zhou, Y. B. Gao, Z. Song, and C. P. Sun - Phys. Rev. A **77**, 013831 (2008).

[7] M. I. Makin, J. H. Cole, C. D. Hill, A. D. Greentree, and L. C. L. Hollenberg - Phys. Rev. A **80**, 043842 (2009).

[8] F. Ciccarello - Phys. Rev. A **83**, 043802 (2011).

[9] A. Tomadin and R. Fazio - J. Opt. Soc. Am. B **27**, A130 (2010).

[10] F. Illuminati - Nat. Phys. **2**, 803 (2006).

[11] S. M. Giampaolo and F. Illuminati - Phys. Rev. A **80**, 050301 (2009).

[12] C. D. Ogden, E. K. Irish, and M. S. Kim - Phys. Rev. A **78**, 063805 (2008).

[13] J. Cho, D. G. Angelakis and S. Bose - Phys. Rev. A **78**, 022323 (2008).

[14] A. Yariv, Y. Xu, R. K. Lee and A. Scherer - Opt. Lett. **24**, no 11 (1999).

[15] F. Lombardo, F. Ciccarello and G. M. Palma - Phys. Rev. A **89**, 053826 (2014)

[16] G. M. A. Almeida and A. M. C. Souza - Phys. Rev. A **87**, 033804 (2013).

[17] L. Zhou, F. Nori *et al.* - Phys. Rev. Lett. **101**, 100501 (2008).

[18] L. Zhou, F. Nori *et al.* - Phys. Rev. A **78**, 063827 (2008).

[19] P. Longo, P. Schmitteckert, and K. Busch - Phys. Rev. Lett. **104**, 023602 (2010).

[20] G. D. Mahan - *Many-Particle Physics* (New York, Plenum Press, 1990).

[21] M. Gadella and G. P. Pronko - Fort. Phys., **59** 795 (2011).

[22] T. Shin and C. P. Sun - Phys. Rev. B **79**, 205111 (2009).

[23] J. Lu, L. Zhou, H. C. Fu, and L.-M. Kuang - Phys. Rev. A **81**, 062111 (2010).

[24] P. Longo, P. Schmitteckert, and K. Busch - Phys. Rev. A **83**, 063828 (2011).

[25] M. Biondi, S. Schmidt, G. Blatter and H. E. Türeci - Phys. Rev. A **89**, 025801 (2014).

[26] S. Longhi - Eur. Phys. J. B **57**, 45 (2007)

[27] B. Gaveau and L. S. Schulman - J. Phys. A **28**, 7359 (1995).

[28] S. Tanaka, S. Garmon, and T. Petrosky - Phys. Rev B **73**, 115340 (2006).

[29] A. G. Kofman , G. Kurizki and B. Sherman - J. Mod. Opt. **41**, 353 (1994).

[30] P. Lambropoulos, G. M. Nikolopoulos, T. R. Nielsen, and S. Bay - Rep. Prog. Phys. **63**, 455 (2000).

[31] M.-T. Cheng, X.-S. Ma, M.-T. Ding, Y.Q. Luo and G.X. Zhao - Phys. Rev A **85**, 053840 (2010).

[32] S. John and J. Wang - Phys. Rev. Lett. **64** 2418 (1990).

[33] S. John and T. Quang - Phys. Rev. A, **50**, 1764 (1994).

[34] *Handbook of Mathematical Functions*, edited by M. Abramowitz and I. A. Stegun (Dover, New York, 1972).

[35] I. L. Garanovich, S. Longhi, A. A. Sukhorukov, and Yu. S. Kivshar - Phys. Rep. **518**, 1 (2012).

[36] S. Longhi - Phys. Rev. E **74**, 026602 (2006); S. Longhi, Phys. Rev. B **80**, 165125 (2009).

[37] H. Trompeter, U. Peschel, T. Pertsch, F. Lederer, U. Streppel, D. Michaelis, and A. Bräuer - Opt. Express **11**, 3404 (2003); S. Longhi - Phys. Rev. A **74**, 063826 (2006).

[38] T. M Cover, J. A. Thomas - *Elements of information theory* (Wiley, 2006).

[39] W. F. Stinespring, Proc. Amer. Math. Soc. **6**, 211 (1955).

[40] V. Gorini, A. Kossakowski, E.C.G. Sudarshan, J. Math. Phys. **17**, 821 (1976).

[41] G. Linblad - Comm. Math. Phys. **48**, 119 (1976).

[42] H.-P. Breuer, F. Petruccione - *The Theory of Open Quantum Systems* (Oxford Press, 2007).

[43] H.-P. Breuer - J. Phys. B: At. Mol. Opt. Phys. 45, 154001 (2012).

[44] M. M.Wolf, J. Eisert, T. S. Cubitt, and J. I. Cirac - Phys. Rev. Lett. **101**, 150402 (2008).

[45] D. Chruscinski and S. Maniscalco - Phys. Rev. Lett. **112**, 120404 (2014).

[46] A. Rivas, S. F. Huelga, B. Plenio - Rep. Prog. Phys. 77, 094001 (2014).

[47] H.-P. Breuer, E. M. Laine and J. Piilo - Phys. Rev. Lett. **103**, 210401 (2009).

[48] E.-M. Laine, J. Piilo and H.-P. Breuer - Phys. Rev. A **81**, 062115 (2010).

[49] B.-H Liu, L. Li, Y.-F. Huang, C.-F. Li, G.-C. Guo, E.-M. Laine, H.-P. Breuer and Jyrki Piilo - Nature Phys. **7**, 931 (2011).

[50] S. Wissmann, A. Karlsson, E.-M. Laine, J. Pilo, H.-J. Breuer - Phys. Rev. **A** 86, 062108 (2012).

[51] A. Rivas, S. F. Huelga and M. B. Plenio - Phys. Rev. Lett. **105**, 050403 (2010); H.-S. Zeng, N. Tang, Y.-P. Zheng and G.-Y.Wang - Phys. Rev. A **84**, 032118 (2011); S. Lorenzo, F. Plastina and M. Paternostro - Phys. Rev. A **84**, 032124 (2011); A. Rosario, E. Massoni and F. De Zela - J. Phys. B: At. Mol. Opt. Phys. **45**, 095501 (2012); R. Vasile, F. Galve and R. Zambrini - Phys. Rev. A **89**, 022109 (2014).

[52] X.-M. Lu, X. Wang and C. P. Sun - Phys. Rev. A **82**, 042103 (2010); P. Haikka, J. Goold, S. McEndoo, F. Plastina and S. Maniscalco - Phys. Rev. A **85**, 060101 (2012); X. Hao, N.-H. Tong and S. Zhu - J. Phys. A: Math. Theor. **46**, 355302 (2013); F. F. Fanchini, G. Karpat, M. C. de Oliveira *et al* - Phys. Rev. Lett. **112**, 210402 (2014).

[53] S. Luo, S. Fu, and H. Song - Phys. Rev. A **86**, 044101 (2012); F. F. Fanchini, G. Karpat, L. K. Castelano, and D. Z. Rossatto - Phys. Rev. A **88**, 012105 (2013); M. Jiang and S. Luo - Phys. Rev. A **88**, 034101 (2013); C. Addis, B. Bylicka, D. Chruscinski, and S. Maniscalco - Phys. Rev. A 90, 052103 (2014).

[54] J. Piilo, K. Harkonen, S. Maniscalco, and K.-A. Suominen - Phys. Rev. A **79**, 062112 (2009); M. J. W. Hall, J. D. Cresser, L. Li, and E. Andersson - Phys. Rev. A **89**, 042120 (2014).

[55] M.M Ali, A. P.-Y. Lo, M. W.-Y. Tu, W.-M. Zhang - Arxiv:01505.05748 (2015).

[56] S. Lorenzo, F. Plastina, and M. Paternostro - Phys. Rev. A **88**, 020102(R) (2013).

[57] T. Jordan, A. Shaji, and E. Sudarshan, Phys. Rev. A **70**, 052110 (2004).

[58] G. Kimura, J. Phys. Soc. Jpn **72**, 185188 (2003).

[59] E. Jaynes and F. Cummings, Proceedings of the IEEE, **51**, nÂ°1, pp. 89-109 (1963).

[60] P.W. Anderson - Phys. Rev. **109**, 1492 (1958).

[61] V. I. Oseledets, Trans. Moscow Math. Soc. **19**, 197 (1968)

[62] P. Lloyd - J. Phys. C , **2**, no 10 (1969).

[63] D. J. Thouless - J. Phys. C: Solid state Phys. **5**, i. 1, pp 77-81 (1972).

[64] D. J. Thouless - Phys. Rev. Lett. **39**, 1167 (1977).

[65] E. Abrahams, P. W. Anderson, D. C. Licciardello, and T. V. Ramakrishnan - Phys. Rev. Lett. *42*, 673 (1979).

[66] J. M. Ziman - *Models of disorder*, (Cambridge Press, 1979).

[67] F. Wegner - Z. Phys. B **36**, i. 3, pp 209-214 (1980).

[68] B. Kramer and A. MacKinnon - Rep. Prog. Phys. **56**, pp 1469-1564 (1993).

[69] M. P. A. Fisher, P. B. Weichman, G. Grinstein, and D. S. Fisher - Phys. Rev. B **40**, 546 (1989).

[70] A. R. McGurn, K. T. Christensen, F. M. Mueller, and A. A. Maradudin - Phys. Rev. B **47**, 13120 (1993).

[71] G. Bergmann - Phys. Rep. **107** (1984).

[72] D. S. Wiersma, P. Bartolini, Ad Lagendijk and R. Righini - Nature **390**, (1997).

[73] S. Karbasi, C. R. Mirr, P. G. Yarandi, R. J. Frazier, K. W. Koch, and Arash Mafi - Optics Lett. **37** (2012).

[74] S. John - Phys. Today (May 1991)

[75] Y. Lahini, A. Avidan, F. Pozzi, M. Sorel, R. Morandotti, D. N. Christodoulides, and Yaron Silberberg - Phys. Rev. Lett. **100**,013906 (2008).

[76] Schwartz T. *et al* - Nature **446**, pp. 52-55 (2007).

[77] Hefei Hu *et al* - Nature Phys. **4**, pp. 945 - 948 (2008) .

[78] G. Roati, C. D'Errico, L. Fallani, M. Fattori, C. Forti, M. Zaccanti, G. Modugno, M. Modugno and M. Inguscio - Nature **453**, pp. 895-898 (2008).

[79] L. Sapienza, H. Thyrrestrup, S. Stobbe, P. D. Garcia, S. Smolka and P. Lodahl - Science **327**, 5971 (2010)

[80] G. M. Petersen - *Anderson Localization in Low-Dimensional Systems with Long-Range Correlated Disorder* (Ph.D. Thesis, Ohio Univ. - 2014)

[81] S. Haroche, J. M. Raimond - *Exploring the Quantum: Atoms, Cavities, and Photons* (Oxford Press, 2006).

[82] S. M. Dutra *Cavity Quantum Electrodynamics - The Strange Theory of Light in a Box* (Wiley, 2005).

[83] P. Meystre and M. Sargent - *Elements of Quantum Optics* (Springer).

[84] J.C. Garrison, R.Y. Chiao - *Quantum Optics* (Oxford Press, 2008).

[85] H. Paul - *Introduction to Quantum Optics* (Cambridge Press, 2004).

[86] D. F. Walls and G. J. Milburn - *Quantum Optics* (Springer, 2007).

[87] P. Schleich - *Quantum Optics in Phase Space* (Wiley, 2001).

[88] M. O. Scully and M. Suhail Zubairy *Q*uantum Optics (Cambridge Press, 1997).

[89] C. Cohen-Tannoudji, J. Dupont-Roc, G. Grynberg - *Atom-Photon Interactions*, (Wiley, 1998).

[90] E. N. Economou - *Green's functions in quantum physics* (Springer-Verlag, Berlin, 1979).

[91] S. Haroche - Rev. of Modern Phys. **85**, 1083 (2013).

[92] E. M. Purcell, H. C. Torrey, and R. V. Pound - Phys. Rev. **69**, 37 (1946).

[93] P. Goy, J. M. Raimond, M. Gross, and S. Haroche - Phys. Rev. Lett. **50**, 1903 (1983).

[94] R. G. Hulet, E. S. Hilfer, and D. Kleppner - Phys. Rev. Lett. **55**, 2137 (1985).

[95] G. Gabrielse and H. Dehmelt - Phys. Rev. Lett. **55**, 67 (1985).

[96] D. Meschede, H. Walther, and G. Muller - Phys. Rev. Lett. **54**, 551 (1985) .

[97] G. Rempe, H. Walther, and N. Klein - Phys. Rev. Lett. **58**, 353 (1987) .

[98] S. Ritter, G. Rempe *et al* - Nature **484** pp. 195-200 (2012).

[99] A. Kuhn and G. Rempe in *Experimental Quantum Computation and Information* (IOS Press 2003), pp. 37-66.

[100] W. Jhe, A. Anderson, E. A. Hinds, D. Meschede, L. Moi, and S. Haroche - Phys. Rev. Lett. **58**, pp. 666-669 (1987).

[101] R. J. Thompson, G. Rempe, and H. J. Kimble - Phys. Rev. Lett. **68**, 1132 (1992).

[102] Q. Turchette, C. J. Hood, W. Lange, H. Mabuchi, and H. J. Kimble - Phys. Rev. Lett. **75**, 4710 (1995).

[103] C. J. Hood, T. W. Lynn, A. C. Doherty, A. S. Parkins, and H. J. Kimble - Science, **287**, 5457 (2000).

[104] J. McKeever, A. Boca, a. D. Boozer, J. R. Buck, and H. J. Kimble, Nature - **425**, pp. 268-271 (2003).

[105] J. McKeever, J.R. Buck, AD Boozer, A. Kuzmich, H.-C. Nagerl, DM Stamper-Kurn, e J. Kimble - Phys. Rev. Lett. **90**, 133602 (2003).

[106] K. M. Birnbaum, A. Boca, R. Miller, A. D. Boozer, T. E. Northup, and H. J. Kimble - Nature, **436**, pp. 87-90, (2005).

[107] C. J. Hood, H. J. Kimble and J. Ye - Phys. Rev. A **64**, 033804 (2001).

[108] T. Aoki, B. Dayan, E. Wilcut, W. P. Bowen, A. S. Parkins, H. J. Kimble, T. J. Kippenberg, and K. J. Vahala - Nature **443**, 825 (2006).

[109] M. Karski, L. F. orster, J. M. Choi, A. Steffen, W. Alt, D. Meschede, and A. Widera - Science, **325**, pp. 174-7 (2009).

[110] M. Trumpke, E. A. Hinds, M. Kraft *et al* - App. Phys. Lett. **87**, no 21 (2005).

[111] J. Goldwin, M. Trupke, J. Kenner, A. Ratnapala, and E. a. Hinds - Nature Comm. **2**, no 418 (2011).

[112] M. Trupke, J. Goldwin, B. Darquie', G. Dutier, S. Eriksson, J. Ashmore, and E. A. Hinds - Phys. Rev. Lett. **99**, 063601 (2007).

[113] A. Mazzei, V. Sandoghdar *et al* - Phys. Rev. Lett. **99**, 173603 (2007).

[114] D. K. Armani, T. J. Kippenberg, S. M. Spillane, and K. J. Vahala - Nature **421** pp. 925-8 (2003).

[115] R. K. Chang and A. J. Campillo - *Optical Processes in Microcavities* (World Scientific, 1996).

[116] L. Collot, V. Lefevre-Seguin, M. Brune, J. M. Raimond and S. Haroche - EuroPhys. Lett. *23* no 5 (1993).

[117] S. M. Spillane, T. J. Kippenberg, O. J. Painter, and K. J. Vahala - Phys. Rev. Lett. **91**, 043902 (2003).

[118] T. F. Krauss, R. M. De La Rue and S. Brand - Nature **383**, pp. 699-702 (1996).

[119] E. Yablonovitch, T.J. Gmitter *et al* - Phys. Rev. Lett. **67**, 2295 (1991).

[120] Y. Akahane, T. Asano, Bong-Shik Song and S. Noda - Nature **425**, 944-947 (2003).

[121] M. Bayindir, B. Temelkuran, and E. Ozbay - Phys. Rev. B **61**, R11855 (2000); Phys. Rev. Lett. **84**, 2140 (2000).

[122] H. Altug and J. Vuckoic - Appl. Phys. Lett. **84**, 161 (2004). (2004).

[123] P. Michler - *Single Semiconductor Quantum Dots*, (Springer, 2009).

[124] A. Badolato, K. Hennessy, M. Atature, J. Dreiser, E. Hu, P. M. Petroff, and A. Imamoglu - Science **308**, 1158 (2005).

[125] K. Hennessy, A. Badolato, M. Winger, D. Gerace, M. Atature, S. Gulde, S. Falt, E. L. Hu, and A. Imamoglu - Nature **445**, 896 (2007).

[126] M. Nomura, N. Kumagai, S. Iwamoto, Y. Ota and Y. Arakawa - Nature Phys. **6**, 279 (2010).

[127] D. Englund, A. Majumdar, A. Faraon, M. Toishi, N. Stoltz, P. Petroff, and J. Vuckovic - Phys. Rev. Lett. **104**, 073904 (2010).

[128] Ze-Liang Xiang, S. Ashhab, J. Q. Yu and F. Nori - Rev. of Modern Phys. **85**, 623 (2013).

[129] Y. Nakamura, Yu A. Pashkin and S. J. Tsai - Nature **398**, 786 (1999).

[130] J.Q. Yu and F. Nori - Phys. Today **58**, no 11 (2005).

[131] S. M. Girvin - *Circuit QED: Superconducting Qubits Coupled to Microwave Photons*, (Oxford press).

[132] A. Blais, R.-S. Huang, A. Wallraff, S. M. Girvin, and R. J. Schoelkopf - Phys. Rev. A **69**, 062320 (2004).

[133] J. Q. You and F. Nori - Nature, **474**, 589 (2011).

[134] I. Buluta, S. Ashhab and F. Nori - Rep. Prog. Phys **74**, 104401 (2011).

[135] A. Wallraff, D. I. Schuster, A. Blais, L. Frunzio, R.-S. Huang, J. Majer, S. Kumar, S. M. Girvin and R. J. Schoelkopf - Nature **431**, 162 (2004).

[136] T. Niemczyk, F. Deppe, R. Gross *et al* - Nature Phys. **6**, 772 (2010).

[137] B. Peropadre, P. Forn-Diaz, E. Solano, and J. J. Garcia-Ripoll - Phys. Rev. Lett. **105**, 023601 (2010).

[138] W. Lepert *Integrated optics for coupled-cavity quantum electrodynamics* (Ph.D. Thesis, Imperial College, London - 2013).

[139] A. A. Houck. H. E. Türeci and J. Koch - Nature Phys. **8**, pp 292-9 (2012); S. Schmidt and J. Koch - Ann. der Phys. **525** i. 2 (2013); D. L. Underwood, W. E. Shanks, J. Koch, and A. A. Houck - Phys. Rev. A **86**, 023837 (2012).

[140] M. Notomi, E. Kuramochi and T. Tanabe - Nature Phot. **2**, pp 741-7 (2008); N Matsuda, E. Kuramochi, H. Takesue and M. Notomi - Opt. Lett. 39, 2290-2293 (2014)

Ringraziamenti (Acknowledgments)

Vorrei ringraziare innanzitutto il mio Tutor, Prof. G. M. Palma, per avermi dato la possibilitá di intraprendere un percorso cosí stimolante, introducendomi pazientemente nel mondo della ricerca in Fisica Teorica e seguendomi costantemente durante questi tre anni di Dottorato. E' inoltre doveroso da parte mia ringraziare i colleghi del gruppo di ricerca Francesco Ciccarello e Salvatore Lorenzo che, grazie alla loro capacitá ed esperienza e mostrandosi sempre disponibili, mi hanno dato ottimi consigli e prontamente aiutato a trovare una soluzione a molti dei problemi che ho incontrato.
Di certo la buona compagnia non mi é affatto mancata nell'ufficio del primo piano in cui ho avuto modo di lavorare. Con i colleghi con cui ho condiviso la stanza mi sono sin da subito sentito a mio agio e di certo non potró dimenticare le stimolanti conversazioni su argomenti scientifici ed anche i simpatici momenti di scherzo e chiacchiera durante le pause. Per questo motivo ringrazio Saro, Salvatore, Salvo, Samuele, Margherita ed Antonio.
Un ulteriore ringraziamento va alla Prof.ssa Anna Napoli per avere pazientemente letto la bozza della tesi, suggerendomi alcune indispensabili correzioni finali.
Desidero infine ringraziare di cuore i miei genitori per il sostegno e per avermi sempre incoraggiato e dato motivazione.